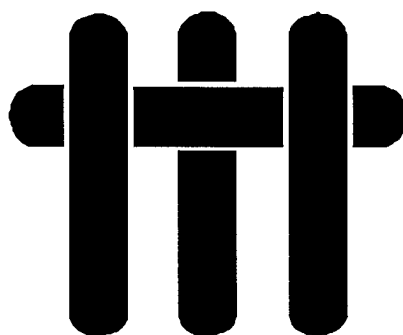


ANNUAL REPORT
to
OFFICE OF NAVAL RESEARCH

Contract NO0014-97-I-0190
October 1997 to October 1998

M A T E R I A L S

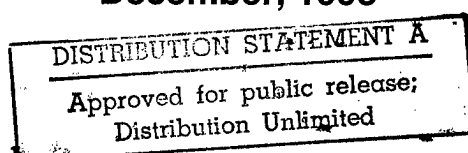


DTIC QUALITY INSPECTED 2

**OXIDATION-INDUCED FAILURE OF THERMAL
BARRIER COATINGS**

David R. Clarke
Materials Department, College of Engineering
University of California, Santa Barbara

December, 1998



1 9 9 9 0 2 1 9 0 8 0

REPORT DOCUMENTATION PAGE			Form Approved OMB No. 0705-0188	
1. AGENCY USE ONLY (Leave blank)		2. REPORT DATE 12/31/98	3. REPORT TYPE AND DATES COVERED Annual report - 10/1/97 through 10-31/98	
4. TITLE AND SUBTITLE Oxidation Induced Failure of Thermal Barrier Coatings			5. FUNDING NUMBERS N00014-97-1-0190	
6. AUTHOR(S) David R. Clarke				
7. PERFORMING ORGANIZATION NAME(S) AND ADDRESS(ES) Materials Department College of Engineering University of California Santa Barbara, CA 93106-5050			8. PERFORMING ORGANIZATION REPORT NUMBER 8-442490-25837	
9. SPONSORING/MONITORING AGENCY NAME(S) AND ADDRESS(ES) Office of Naval Research Program Officer Steven G. Fishman ONR 332 Ballston Centre Tower One 800 North Quincy Street Arlington, Va 22217-5660			10. SPONSORING/MONITORING AGENCY REPORT NUMBER	
11. SUPPLEMENTARY NOTES				
12A. DISTRIBUTION/AVAILABILITY STATEMENT			12B. DISTRIBUTION CODE	
13. ABSTRACT (Maximum 200 words) <p>On prolonged high-temperature exposure in air, thermal barrier coatings (TBCs) on bond-coated superalloys fail by spalling. We have focused on identifying the underlying mechanisms of failure and sought to establish whether it is a direct consequence of the failure of the underlying thermally grown oxide. We have discovered a new TBC failure mode, one in which failure is associated with moisture-enhanced sub-critical crack-growth along the bond-coat/thermally grown oxide interface. By making concurrent piezospectroscopy measurements, the interfacial fracture energy was determined to be $\sim 10 \text{ J/m}^2$ – a considerably smaller value than that of sapphire/metal interfaces prepared in the laboratory but consistent with measurements of the effects of segregation on metal/ceramic interfaces. New insights into the mechanism underlying failure of the thermally grown oxide have come from direct optical microscopy. These indicate that failure is associated with surface roughness of the bond-coat and specifically that the thermally-grown oxide separates from the bond-coat on cooling at the concave (“crests”) surface features. These locally separated regions grow with oxidation time and are seen to link-up. These events are believed to be the precursor events that grow to provide the critical-sized flaws from which buckling and spalling of thermal barrier coatings occur.</p>				
14. SUBJECT TERMS Thermal Barrier Coating, Oxidation-induced failure of thermal barrier coatings, Thermally grown oxide,			15. NUMBER OF PAGES	
			16. PRICE CODE	
17. SECURITY CLASSIFICATION OF REPORT Unclassified	18. SECURITY CLASSIFICATION OF THIS PAGE Unclassified	19. SECURITY CLASSIFICATION OF ABSTRACT Unclassified	20. LIMITATION OF ABSTRACT	

EXECUTIVE SUMMARY

On prolonged high-temperature exposure in air, both protective thermal barrier coatings (TBCs) on bond-coated superalloys and the thermally grown oxide (TGO) formed on the same bond-coated alloys fail by spalling. During the current year, we have focused on identifying the underlying mechanisms responsible for these failures and sought to establish whether the failure of electron-beam deposited TBCs is a direct consequence of the failure of the thermally grown oxide.

In the course of this work, we have discovered that one mode of TBC failure is associated with moisture enhanced sub-critical crack-growth along the bond-coat/thermally grown oxide interface. This is a hitherto unrecognized failure mode and was characterized using time-lapsed microscopy observations. By making concurrent piezospectroscopy measurements of the residual stress, the interfacial fracture energy was determined to be $\sim 10 \text{ J/m}^2$ – a considerably smaller value than that of sapphire/metal interfaces prepared in the laboratory but consistent with measurements of the effects of carbon segregation on metal/ceramic interfaces. (This was work performed earlier under the preceding grant period). This discrepancy is believed to be a result of segregation of impurities to the interface during prolonged oxidation exposure. The mechanism responsible for the nucleation of the observed failure has not yet been identified.

New insights into the mechanism underlying failure of the thermally grown oxide have, surprisingly, come from direct optical microscopy observations. These indicate that failure is associated with surface roughness of the bond-coat and specifically that the thermally-grown oxide separates from the bond-coat on cooling at the concave (“crests”) surface features. These locally separated regions grow with oxidation time. Despite being under biaxial compression, it is believed that the oxide separates from the underlying metal because the surface curvature geometrically transforms the compressive stress to a local tensile stress across the oxide/metal interface. These isolated separations are seen to link-up and are believed to be the precursor events that grow to provide the critical-sized flaws from which buckling and spalling of thermal barrier coatings occur. If this separation process is indeed correct it provides the “missing link” in applying the fracture mechanics of compressed films to spalling of TBCs. The mechanics requires that a flaw tens to hundreds of microns in size to pre-exist at the oxide/metal interface. These are not present in as-deposited coatings but the separations we see are observed to evolve to this size. A model for this separation has recently been submitted for publication. The gradual evolution of damage by localized separation and growth is also consistent with our piezospectroscopy measurements of the stress distribution in TBCs where we find increasing spatial variation in residual stress with increasing oxidation time until failure occurs.

**REPORTS OF WORK SUPPORTED
UNDER CONTRACT N00014-97-I-0190**

- Q. Wen, D. M. Lipkin and D. R. Clarke, **Luminescence Characterization of Chromium Containing Theta Alumina**, Journal of the American Ceramic Society, 81 [12] 3345-3348 (1998).
- V. Sergo and D. R. Clarke, **Observation of Sub-critical Spall Propagation of a Thermal Barrier Coating**, Journal of the American Ceramic Society, 81 [12] 3237-3242 (1998).
- X-Y. Gong and D. R. Clarke, **On The Measurement of Strain in Coatings Formed on a Wrinkled Elastic Substrate**, Oxidation of Metals, 50 [3/4] 355-376 (1998).
- V. K. Tolpygo and D. R. Clarke, **Wrinkling of α -Alumina Films Grown By Thermal Oxidation: I. Quantitative Studies on Single Crystals of Fe-Cr-Al Alloy**, Acta Materialia, 46 [14] 5153-5166 (1998).
- V. K. Tolpygo and D. R. Clarke, **Wrinkling of α -Alumina Films Grown By Thermal Oxidation: II. Oxide Separation and Failure**, Acta Materialia, 46 [14] 5167-5174 (1998).
- D. R. Clarke and W. Pompe, **Critical Radius For Interface Separation Of A Compressively Stressed Film From a Rough Surface**, Acta Materialia, In Press.
- V. K. Tolpygo and D. R. Clarke, **Initiation of Oxide Scale Decohesion and Spalling: Microscopy Observations and Piezospectroscopic Strain Measurements**, Journal of the Electrochemical Society, In press.

Luminescence Characterization of Chromium-Containing θ -AluminaQingzhe Wen,[†] Donald M. Lipkin,[‡] and David R. Clarke*

Materials Department, College of Engineering, University of California, Santa Barbara, California 93106-5050

Characteristic photostimulated luminescence (fluorescence) in the visible range is reported from θ transition alumina prepared by using a variety of methods. The luminescence is associated with trace concentrations of chromium and can be intensified by intentional chromium doping. The luminescence from θ -alumina is similar to, albeit considerably weaker than, the R-line luminescence from α -alumina. The θ -alumina spectrum is characterized by a doublet at ~ 14575 and 14645 cm^{-1} at 77 K and is blue-shifted from the R-lines of α -alumina by $\sim 150\text{ cm}^{-1}$. The doublet is attributed to Cr^{3+} ions in octahedral coordination and can be used for phase identification in microstructural characterization.

I. Introduction

ALTHOUGH the R-line luminescence from chromium-doped α -alumina is probably the most familiar, being the basis for the ruby laser, strong luminescence is also known to occur in other oxides that contain substitutional Cr^{3+} ions in octahedral coordination.¹ For instance, R-line luminescence has been reported from Cr^{3+} ions in MgO (periclase),¹ LiNbO_3 ,² SrTiO_3 ,³ MgSiO_4 (forsterite),⁴ $\text{Y}_3\text{Al}_5\text{O}_{12}$ (YAG),⁵ and MgAl_2O_4 (spinel).⁶⁻⁸ In addition to observations from the normal spinel, there have been several studies that concern the details of the luminescence spectrum from other spinels to determine the nature of cation ordering on the tetrahedral and octahedral sites.⁸⁻¹⁰ However, there have been no reports of fluorescence from the θ or γ transition aluminas, despite their structural similarities to the other spinels.

The origin of the luminescence in the above-mentioned oxides is the photostimulation and subsequent radiative decay of excited d^3 electrons in substitutional Cr^{3+} ions located on octahedral sites.^{11,12} Because it has been reported that Al^{3+} ions can occupy octahedral and tetrahedral sites, in θ - and γ -alumina, it might be expected that trace chromium would also occupy these sites and, when suitably excited, result in characteristic luminescence.

In this report, we describe the luminescence from aluminas prepared via several different methods. These materials include θ - and γ -alumina powders annealed in the presence of chromium-containing vapor, the oxide produced by the thermal oxidation of nickel aluminide (NiAl), and an alumina film formed by the solid-phase epitaxial regrowth of a chromium-doped (Cr_2O_3 -doped) amorphous alumina on a sapphire substrate.

II. Experimental Details

The visible-range luminescence properties of the investigated aluminas were characterized at room temperature and at

77 K (by immersion in liquid nitrogen). Low-temperature measurements were used to minimize thermal broadening, which allowed greater spectral resolution. The photoluminescence was excited using an argon-ion laser at a wavelength (λ) of 514.5 nm as the excitation source. The resulting luminescence was collected and analyzed using a standard dispersive (1 m) spectrometer with a liquid-nitrogen-cooled charge-coupled device (CCD).

Nominally pure θ -alumina powder and a commercially available γ -alumina powder were studied. The θ -alumina was prepared by calcining Disperal sol P2 powder at a rate of $10^\circ\text{C}/\text{min}$ to 1000°C and was identified as fully θ -alumina via X-ray diffraction (XRD).¹³ Two methods were used to introduce chromium doping into the powders. In the first, the powders were pressed and then sintered for 5 h at a variety of temperatures (up to 1100°C) in a capped alumina crucible; a pellet of Cr_2O_3 powder was adjacent to (but not in physical contact with) the alumina pellet, so that the alumina was exposed to chromium-containing vapor. After sintering, the crucible and the pellets both had a pinkish color. In the second doping method, Cr_2O_3 powder was mixed with the individual alumina powders and pressed into pellets that were sintered for various times at 1000° and 1050°C . After sintering, the samples were characterized via XRD and luminescence spectroscopy.

Aluminum oxide was also prepared by the oxidation in air of (111) single crystals of NiAl at 900° and 1100°C . Although such oxidation does not lead to single-phase θ -alumina, previous work¹⁴ has shown that a coexisting mixture of α - and θ -alumina is formed; the proportion is dependent on the oxidation temperature.

In still another set of experiments, alumina thin films were formed by regrowth of chromium-doped amorphous alumina deposited on *c*-plane sapphire. These alumina thin films have been described previously by Wen *et al.*¹⁵

III. Observations

The as-received θ -alumina powder exhibited a very weak broad luminescence spectrum, extending from $\sim 14000\text{ cm}^{-1}$ to 14650 cm^{-1} , as well as two distinct peaks at 14575 and 14645 cm^{-1} (denoted by downward arrows in Fig. 1) at room temperature and in liquid nitrogen (Fig. 1). The two lines marked " α " in Fig. 1 (at ~ 14404 and 14432 cm^{-1} in the 77 K spectrum) are attributed to a minor concentration of α - Al_2O_3 , presumably due to partial transformation. Attempts to further increase the chromium above the impurity level by doping the as-received powder were only partially successful, because the powder readily transformed to α - Al_2O_3 , as evidenced by the strong R-line luminescence. Nevertheless, despite the partial transformation, the spectrum from the θ -alumina powder after sintering for 5 h at 1050°C in the presence of the chromium-containing vapor exhibited the same characteristic lines in the as-received powder, at 14575 and 14645 cm^{-1} . In addition, the broad-band luminescence decreased while the characteristic lines grew stronger in the sintered powder.

The as-received γ -alumina powder exhibited no distinctive luminescence at either room temperature or in liquid nitrogen, with only a weak, broad luminescence background. After sintering in the presence of Cr_2O_3 , the luminescence shown in Fig. 2 was obtained. The same doublet as that recorded from the

W. White—contributing editor

Manuscript No. 190484. Received December 19, 1997; approved June 17, 1998. Supported by the U.S. Office of Naval Research, under Grant No. NO0014-97-1-0190.

*Member, American Ceramic Society.

†Now with Hewlett-Packard, Palo Alto, CA.

‡Now with General Electric Corporate Research and Development, Niskayuna, NY 12309.

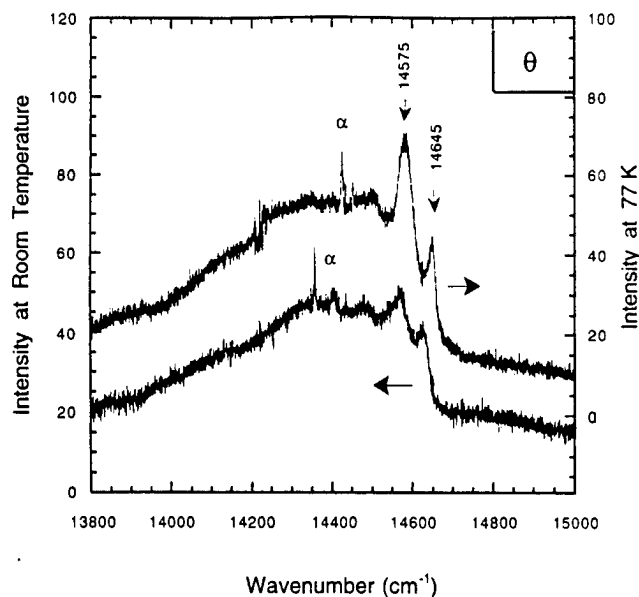


Fig. 1. Luminescence spectra from the as-received θ -alumina powder. In addition to the broad luminescence extending from ~ 14000 cm^{-1} to 14645 cm^{-1} , there are two lines (denoted by the downward arrows) at 14575 and 14645 cm^{-1} , as well as evidence of a broader line. The line marked " α " is attributed to a minor concentration of α -alumina in the powder.

θ -alumina is present at 14645 – 14575 cm^{-1} , as well as two somewhat broader peaks at 14260 and 14360 cm^{-1} . A small trace of α -alumina is also present, as indicated. Very similar but stronger luminescence was obtained from the cofired γ -alumina and Cr_2O_3 powder (see Fig. 3). The most-notable feature of the latter is the increase in the relative intensity of the line at ~ 14360 cm^{-1} . Also, as with the spectra of Figs. 1 and 2, the relative intensities of the two lines in the 14575 – 14645 cm^{-1} doublet reversed when the powder was cooled in liquid nitrogen. XRD measurements confirmed that the powder obtained after both annealing treatments was predominantly θ -alumina.

The spectra recorded from the oxide scale formed on the (111) NiAl surfaces at 900° and 1100°C were similar in many respects to those described previously in this work, with a doublet in the region of 14500 – 14650 cm^{-1} (Fig. 4). However, although the shape and energy of the line at 14620 cm^{-1} was

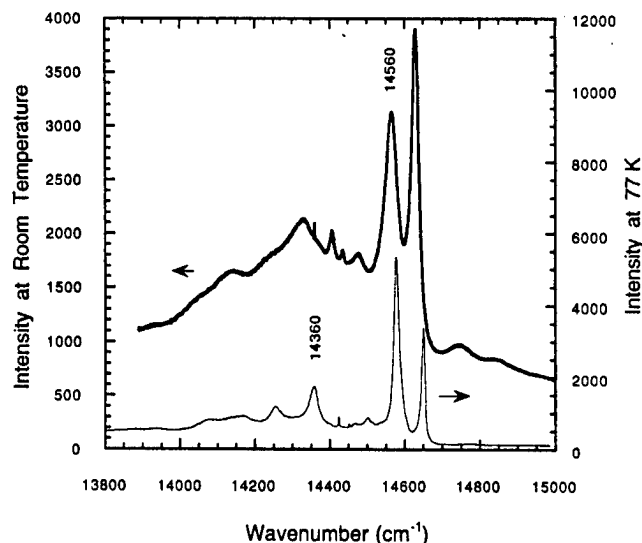


Fig. 2. Luminescence spectra from γ -alumina powder after heating in the presence of vapor from Cr_2O_3 powder for 5 h at 1050°C .

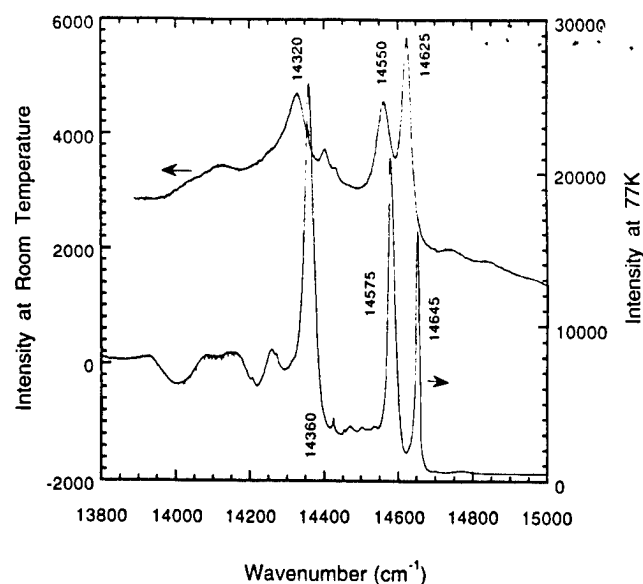


Fig. 3. Luminescence spectra from cofired γ -alumina and Cr_2O_3 powder (5 h at 1050°C); the spectra are similar to that observed in Fig. 2, but with a much-intensified line at 14360 cm^{-1} .

almost unchanged from place to place on the samples, there were quite marked differences in the lower-frequency line. In some locations, the line was centered at ~ 14530 cm^{-1} , whereas in others, it appeared as two distinct lines, one at 14520 cm^{-1} and the other at 14570 cm^{-1} . In all the spectra, there was also broad band luminescence in the range of 14150 – 14350 cm^{-1} .

Weak luminescence at liquid-nitrogen temperature was also recorded from the 800-nm -thick chromium-doped alumina film regrown on sapphire and annealed for 4 h at 750°C (Fig. 5). The most-distinctive feature of the resulting spectrum is the doublet at the same frequency as that observed in the spectra from the θ -alumina powder. The other doublet, labeled α in Fig. 5, is attributed to the very weak R-line luminescence from the ultrahigh-purity sapphire substrate.

IV. Discussion

The observations reported here indicate that θ -alumina exhibits a distinctive luminescence doublet at ~ 14626 and 14564

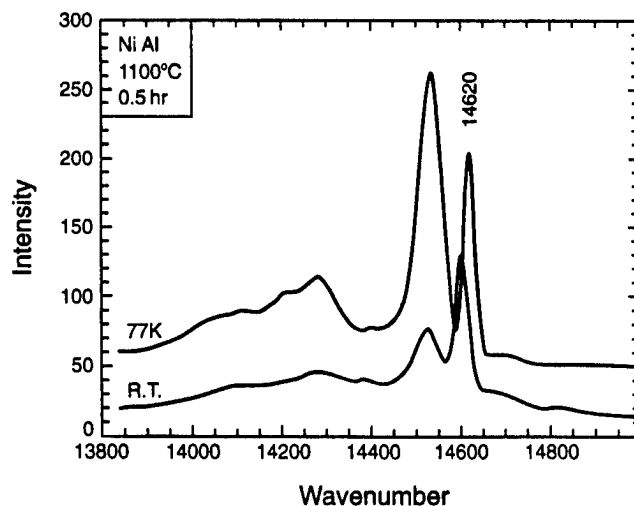


Fig. 4. Luminescence spectra from a small region on the surface of (111) NiAl after oxidation at 1100°C , obtained using a $1\text{ }\mu\text{m}$ optical probe. Other regions exhibit very strong R-line luminescence from α -alumina.

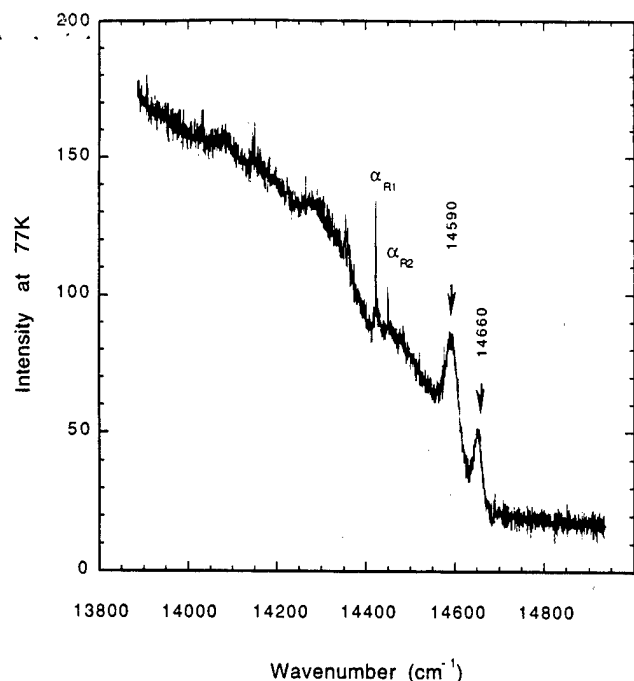


Fig. 5. Liquid-nitrogen luminescence spectrum from the alumina film formed on sapphire via the regrowth of an 800-nm-thick chromium-doped amorphous film at 750°C for 4 h.

cm⁻¹ when doped with chromium. Although still narrow, the lines are not as sharp as those of the R-line luminescence from Cr³⁺ ions in α-alumina. The doublet is similar to that previously reported by Bohandy,¹⁶ where alumina-chromia mixtures were annealed over a range of temperatures for electron-spin-resonance studies. Although uncertain as to their origin, Bohandy conjectured that the peaks were analogous to the R-lines in ruby. However, the spectrum in his paper did not extend far enough to ascertain whether the weaker lines at ~14300 cm⁻¹ were also present.

Although, at this point, we are unable to assign the individual lines to specific electronic transitions, a preliminary identification can be made based on the equation of state for sapphire and the known pressure dependence of the R-line luminescence from ruby, assuming that the observed doublet is also R-line luminescence. An estimate of the θ-alumina R-line energies can be made if we make the additional assumption that the local CrO₆ octahedral arrangement in θ-alumina can be obtained by uniformly expanding the CrO₆ octahedron in α-alumina, and that the material maintains the bulk modulus of sapphire. According to the neutron diffraction data of Zhou and Snyder,¹⁷ the average Al-O distance for octahedral Al in θ-alumina is 0.1948 nm. In contrast, the average Al-O distance in sapphire is only 0.191245 nm. Assuming the Cr-O distances are the same as the Al-O distances in both θ- and α-alumina, there is a volumetric increase of 5.7% in altering the CrO₆ arrangement in α-alumina to that of θ-alumina. The negative pressure required to cause this volume change can be computed from an equation of state of sapphire, for instance, the Birch-Murnaghan equation of state:^{18,19}

$$P(f) = 3K_0f(1+2f)^{5/2}(1+a_1f) \quad (1)$$

where

$$f = \frac{1}{2} \left[\left(\frac{V_\alpha}{V_\theta} \right)^{2/3} - 1 \right]$$

and

$$a_1 = \frac{3}{2}(K'_0 - 4)$$

K_0 is the bulk modulus of sapphire at ambient pressure (254 GPa) and K'_0 is a constant that has a value of 4.3.¹⁹ Using this relationship, a negative pressure of 12.5 GPa is necessary to produce the required volume change. According to the well-established data for the pressure dependence of the R-line fluorescence,²⁰⁻²² the corresponding frequency shift would be 95 cm⁻¹. Although the calculated shift is ~100 cm⁻¹ from the observed displacement in the θ-alumina luminescence peaks, the discrepancy is attributed to the inadequate accounting of the changes in bond character that accompany the θ→α phase transformation. In consideration of this evidence, we conclude that the observed lines at 14575 and 14650 cm⁻¹ are R-lines due to Cr in an octahedral arrangement. Interestingly, the 75 cm⁻¹ separation of the two lines is larger than that of the R1-R2 separation in ruby, which suggests that the contribution from the trigonal distortion and spin-orbit coupling is larger. This phenomenon may be due to the Cr being further from the center of the CrO₆ than it is in ruby. (The variation in luminescence frequency across the NiAl sample is attributed to stress-induced shifts caused by the thermal expansion mismatch with the underlying NiAl alloy.) The somewhat broader lines, centered at 14332 cm⁻¹, are tentatively ascribed to being N-lines due to Cr-Cr interactions and are at a lower energy than the R-lines. Based on the limited number of experiments, their intensity seems to increase as the chromium concentration increases.

The fact that the luminescence from α- and θ-alumina occurs at different frequencies provides an opportunity to use characteristic luminescence for phase identification and phase mapping in microstructural characterization studies. Figure 6 shows a room-temperature luminescence image of the spatial distribution of the α- and θ-phases in the alumina formed via the oxidation of NiAl. The image of the α-phase (right-hand side) was formed by collecting the luminescence from the R-lines over the range of 14325-14450 cm⁻¹ and the image of the θ-phase (left-hand side) was formed using the luminescence over the range of 14475-14650 cm⁻¹. Together with similar images formed at successively longer oxidation times, such images show that the α-alumina phase nucleates and grows by consuming the θ-phase.²³ This transformation process, via nucleation and growth, is consistent with the X-ray findings of

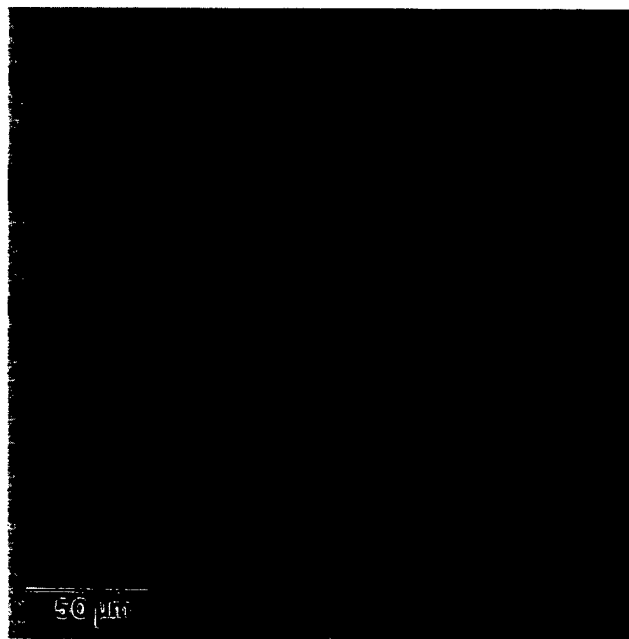


Fig. 6. Complementary images of the oxidation scale formed on a (111) NiAl surface formed using the luminescence from θ-alumina (left-hand side) and α-alumina (right-hand side); the intensity is proportional to the luminescence intensity.

Brumm and Grabke,¹⁴ who showed that the α - and θ -phases can, under certain conditions, coexist within the oxide scale that is formed on NiAl. Furthermore, the observed frequency variation of the θ -phase luminescence across the NiAl samples suggests that, with suitable calibration, such shifts may be useful for piezospectroscopic analysis of residual stresses in the θ -phase.

V. Conclusions

θ -alumina that contains trace chromium concentrations has been shown to exhibit characteristic R-line luminescence. This phenomenon is attributed to the presence of Cr^{3+} ions in octahedral coordination. The frequency shift of the θ -alumina luminescence, with respect to the ruby R-lines, is believed to be a consequence of the larger volume of the CrO_6 octahedra in the θ -alumina than in α -alumina, as well as a change in the bond character that is associated with the transformation.

Acknowledgments: The authors are grateful to Mr. Scott Nordahl (Pennsylvania State University, University Park, PA) for providing us with a sample of θ -alumina for comparison purposes and to Dr. Segei Feofilov (A. F. Ioffe Physics-Technical Institute, St. Petersburg, Russia) for correspondence related to the luminescence from γ -alumina.

References

- ¹H. G. Drickamer, "The Effect of High Pressure on the Electronic Structure of Solids"; pp. 1-63 in *Solid State Physics*, Vol. 17. Edited by F. Seitz and D. Turnbull. Academic Press, New York.
- ²B. Macalik, L. E. Bausa, J. Garcia Sole, and F. Jaque, "Influence of the Stoichiometry in the Site Distribution of Cr^{3+} in LiNbO_3 ," *Appl. Phys. Lett.*, **62** [16] 1887-88 (1993).
- ³T. S. Chang and G. F. Imbusch, "Effect of Domain Structure on the Fluorescence of Cr^{3+} -doped SrTiO_3 ," *J. Appl. Phys.*, **42** [12] 4704-707 (1971).
- ⁴W. Jia, H. Liu, S. Jaffe, W. M. Yen, and B. Denker, "Spectroscopy of Cr^{3+} and Cr^{4+} Ions in Forsterite," *Phys. Rev. B: Condens. Matter*, **43** [7] 5234-42 (1991).
- ⁵P. R. Wamsley and K. L. Bray, "The Effect of Pressure on the Luminescence of Cr^{3+} :YAG," *J. Lumin.*, **59**, 11-17 (1994).
- ⁶D. L. Wood, G. F. Imbusch, R. M. Macfarlane, P. Kisliuk, and D. M. Larkin, "Optical Spectrum of Cr^{3+} Ions in Spinel," *J. Chem. Phys.*, **48** [11] 5255-63 (1968).
- ⁷W. Streck, P. Deren, and B. Jezowska-Trzebiatowska, "Optical Properties of Cr^{3+} in MgAl_2O_4 Spinel," *Physica B (Amsterdam)*, **152**, 379-84 (1988).
- ⁸C. Garapon, H. Manaa, and R. Moncorge, "Absorption and Fluorescence Properties of Cr^{3+} Doped Nonstoichiometric Green Spinel," *J. Chem. Phys.*, **95** [8] 5501-12 (1991).
- ⁹W. Streck, P. Deren, and B. Jezowska-Trzebiatowska, "Broad Band Emission of Cr^{3+} in MgAl_2O_4 Spinel," *J. Phys. C*, **C7** [12] C7-475-C7-477 (1987).
- ¹⁰J. M. G. Tijero and A. Ibarra, "Use of Luminescence of Mn^{2+} and Cr^{3+} in Probing the Disordering Process in MgAl_2O_4 Spinel," *J. Phys. Chem. Solids*, **54** [2] 203-207 (1993).
- ¹¹D. S. McClure, "Electronic Spectra of Molecules and Ions in Crystals. Part II. Spectra of Ions in Crystals"; pp. 399-525 in *Solid State Physics*, Vol. 9. Edited by F. Seitz and D. Turnbull. Academic Press, New York, 1959.
- ¹²B. Henderson and G. F. Imbusch, *Optical Spectroscopy of Inorganic Solids*. Oxford Science Publications, Oxford University Press, New York, 1989.
- ¹³Scott Nordal, Pennsylvania State University, University Park, PA; private communication.
- ¹⁴M. W. Brumm and H. J. Grabke, "The Oxidation Behavior of NiAl—I. Phase Transformations in the Alumina Scale during Oxidation of NiAl and NiAl-Cr Alloys," *Corros. Sci.*, **33** [11] 1677-90 (1992).
- ¹⁵Q. Wen, N. Yu, D. R. Clarke, and M. Nastassi, "Epitaxial Regrowth of Ruby on Sapphire for an Integrated Thin Film Stress Sensor," *Appl. Phys. Lett.*, **66** [3] 293-95 (1995).
- ¹⁶J. Bohandy, "Electron Spin Resonance and Optical Fluorescence of the Chromia-Alumina System," *J. Solid State Chem.*, **3**, 467-72 (1971).
- ¹⁷R.-S. Zhou and R. L. Snyder, "Structures and Transformation Mechanisms of the η , γ and θ Transition Aluminas," *Acta Crystallogr., Sect. B: Struct. Sci.*, **B47**, 617-30 (1991).
- ¹⁸O. L. Anderson, *Equations of State of Solids for Geophysics and Ceramic Science*. Oxford University Press, New York, 1995.
- ¹⁹J. H. Eggert, K. A. Goettel, and I. F. Silvera, "Ruby at High Pressure. I. Optical Line Shifts to 156 GPa," *Phys. Rev. B: Condens. Matter*, **B40** [8] 5724-32 (1989).
- ²⁰G. J. Piermarini, S. Block, J. D. Barnett, and R. A. Foreman, "Calibration of the Pressure Dependence of the R_1 Ruby Fluorescence Line to 195 kbar," *J. Appl. Phys.*, **46**, 2774-80 (1975).
- ²¹R. G. Munro, "A Scaling Theory of Solids under Hydrostatic Pressure," *J. Chem. Phys.*, **67** [7] 3146-50 (1977).
- ²²J. He and D. R. Clarke, "Determination of the Piezospectroscopic Coefficients for Chromium-Doped Sapphire," *J. Am. Ceram. Soc.*, **78** [5] 1347-53 (1995).
- ²³D. M. Lipkin, D. R. Clarke, H. Schaffer, and F. Adar, "Lateral Growth Kinetics of α Alumina Accompanying the Formation of a Protective Scale on (111) NiAl during Oxidation at 1100°C," *Appl. Phys. Lett.*, **70** [19] 2550-52 (1997). □

Observation of Subcritical Spall Propagation of a Thermal Barrier Coating

Valter Sergo^{*†} and David R. Clarke^{*}

Materials Department, College of Engineering, University of California, Santa Barbara, California 93106-5050

Observations are reported of the room-temperature propagation of a spalling failure mode of a thermal barrier coating (TBC) from its bond coat after oxidation. The coating is a Y_2O_3 -stabilized ZrO_2 coating formed by electron-beam deposition on a Ni-Co-Cr-Al-Y bond coat. The spall shape evolution and stress redistribution as the spall propagates are reported. The failure propagates primarily as an interface crack between the bond coat and the thermally grown aluminum oxide (TGO) formed on the underside of the TBC during oxidation. The observations are consistent with subcritical propagation of an interface crack between the TGO and bond coat assisted by the presence of moisture. An estimate of 9 J/m^2 is made of the fracture resistance in air of the interface.

I. Introduction

AS WITH the development of other metal/ceramic systems, the structural reliability of thermal barrier coatings (TBCs) is of utmost concern, and, therefore, extensive research has focused on the mechanisms of failure. Under normal circumstances, if thermal coatings fail, they generally do so by spalling on cooling after thermal cycling.¹ This is attributed to the development of thermal expansion mismatch stresses on cooling. Occasionally another type of failure occurs, one in which the TBC spontaneously spalls entirely from the alloy at room temperature within some indefinite period of time, which can vary from hours to months, after cooling. The implication of these failures is that they are associated with some form of subcritical crack propagation, but they are so infrequent as to preclude systematic study.

Quite serendipitously we observed one of these room-temperature spalling failures that was occurring at a sufficiently slow rate to make some measurements. Recognizing the unusual opportunity this particular time-dependent failure presented, we examined its shape evolution and the stress redistribution in detail. Measurements were made of the three-dimensional shape of the spall and of the residual stress distribution in the thermally grown aluminum oxide (TGO) formed on the underside of the TBC. Residual stress measurements were made using photostimulated Cr^{3+} luminescence-based piezospectroscopy. The methodology has been described in detail elsewhere,²⁻⁵ as has its application for the nondestructive, noncontact measurement of residual stress in the TGO formed beneath thermal barrier coatings.⁶

The TBC examined was one deposited by electron-beam

evaporation of ZrO_2 onto a plasma-sprayed Ni-Co-Cr-Al-Y bond coat on a PWA 1484 superalloy. After the first cycle of oxidation for 2 h at 1121°C , the sample was inadvertently dropped and would, under normal circumstances, not have been oxidized further. No damage was apparent, and the sample was subsequently oxidized for another 10 h at 1121°C . Some indeterminate number of days after cooling, the TBC buckled and spalled from the edge (Fig. 1(a)). This time was subsequently designated as $t = 0 \text{ d}$. Over the next several weeks, the failure advanced in several distinct branches across the coating until the spalling pattern shown in Fig. 1(b) developed. (The term buckling is used here to describe the uplift of the TBC, a precursor to subsequent cracking and final separation. Cracking and final separation are referred to as spalling.)

In the following sections, optical microscopy observations of the buckle and spall propagation are presented, together with measurements of its shape evolution and the residual stress redistribution.

II. Observations

The progression of failure over a period of 20 d is shown in the sequence of photomicrographs in Fig. 1. During the course of these observations, the relative humidity in the room was $\sim 55\%$. The change in the size and shape of the spall can be seen by comparing the optical micrographs in Fig. 1. In the measurements described below, particular attention was paid to the extension of the buckle shown at higher magnification in Fig. 2. With time, the buckle propagated to the left from the point Q and then deflected by $\sim 90^\circ$. The accompanying crack along the buckle ridge also bifurcated, with one branch extending along the buckle ridge in Fig. 2(b) to the point designated as O. With further exposure, the buckle continued to propagate, as did the ridge line crack. Interestingly, the width of the buckle perpendicular to its propagation direction appeared to be approximately constant. In Figs. 2(a) and (b), the buckle extending from point Q was uncracked, but at some time between the recording of Figs. 2(b) and (c), the buckle boundary cracked at C.

To test whether the buckle extended in the absence of moisture, the sample was held for 3 d under dry nitrogen at zero humidity. No propagation was noted during this period, but, as soon as the sample was again exposed to air, the buckle continued to propagate.

(1) Buckling Morphology

To quantify the shape of the extending buckle, the height of the TBC surface was measured as a function of distance in the vicinity of the buckle. Because the heights were relatively large, they were measured by counting the rotations of the optical microscope stage required to bring the surface into focus as a function of position around the buckle. Measurements were also made with a diamond stylus profilometer; they gave essentially the same profile. Although measurement error was relatively large ($\pm 20 \mu\text{m}$), it was substantially smaller than the height of the buckle. The height variation at $t = 10 \text{ d}$ of the buckle propagating toward the lower left in Fig. 2 is shown in the perspective three-dimensional graph of Fig. 3. The profile

D. B. Marshall—contributing editor

Manuscript No. 190557. Received November 20, 1997; approved March 27, 1998. Supported by Office of Naval Research under Grant No. N00014-97-1-0190. Additional support provided to Dr. Sergo from the "Research Abroad" project from the University of Trieste.

^{*}Member, American Ceramic Society.

[†]Now with Materials Engineering Department, University of Trieste, Trieste, Italy.

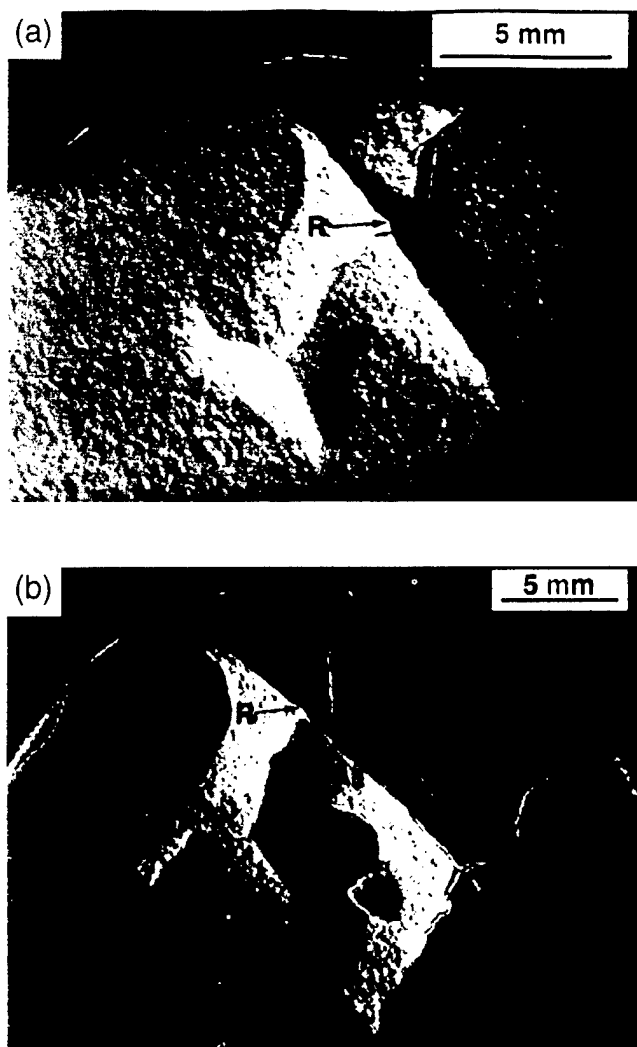


Fig. 1. Appearance of buckling and spalling when (a) it was first noticed and (b) 20 d later. R is a point of reference with which the extent of spalling can be assessed.

in the direction of the crack, OA, and perpendicular to the crack, OB, are shown in Fig. 4(a). Also shown in Fig. 4(b) is the profile along the line QC of the first buckle. A striking feature of these profiles is that the buckled portions are essentially straight rather than concave or convex, indicating that the

buckled material is not subject to any significant net bending moment. An estimate of residual strain in the coating prior to buckling can also be obtained geometrically from the buckle height and width. For instance, using the profile measured perpendicular to the buckle propagation direction, i.e., along the direction OB, the compressive residual strain relieved by buckling is $\sim 2.7\%$. Similarly, from the profile along the line QC, residual strain is also calculated to be $\sim 2.7\%$.

(2) Piezospectroscopic Measurements

In addition to the morphological measurements, a series of piezospectroscopic measurements of residual stress in the TGO were made in order to ascertain the strain energy release associated with failure propagation. Measurements were made using an optical microprobe in which an argon-ion laser was focused onto the region of interest identified in the optical microscope. Using a $10\times$ objective lens, a spot size of $\sim 50\ \mu\text{m}$ could be obtained on the sample surface. Luminescence from Cr^{3+} ions in the TGO excited by the laser beam was collected by the same objective lens and passed through the attached spectrometer to a charged couple device (CCD) detector for frequency analysis.

Piezospectroscopy measurements were made as a function of distance from point O in Fig. 2 in two orthogonal directions, OA and OB. The method is shown schematically in Fig. 5. Previous work has indicated that it is possible to probe an attached TGO through an electron-beam-deposited TBC⁶ but not through an additional air gap. Thus, luminescence could be obtained from the TGO shown schematically at A but not at B. In addition, measurements were also made from the ridge crack at point Q in the direction QC. The measurements were made by traversing the sample with respect to the stationary optical probe using a computer-controlled X-Y stage fitted to the optical microprobe. The shift, $\Delta\nu$, in frequency of the R2 luminescence line from its stress-free frequency was used to evaluate the biaxial stress as follows: For a randomly oriented polycrystalline Al_2O_3 , the general piezospectroscopic relationship² can be written as

$$\begin{aligned}\overline{\Delta\nu} &= \frac{1}{3}(\Pi_{11} + \Pi_{22} + \Pi_{33})(\sigma_{11} + \sigma_{22} + \sigma_{33}) \\ &= \frac{1}{3}\Pi_{ii}(\sigma_{11} + \sigma_{22} + \sigma_{33})\end{aligned}\quad (1)$$

where Π are the piezospectroscopic coefficients. For a biaxial stress state, i.e., for $\sigma = \sigma_{11} = \sigma_{22}$, $\sigma_{33} = 0$, the piezospectroscopic relation of Eq. (1) can be written as

$$\overline{\Delta\nu} = \frac{2}{3}\Pi_{ii}\sigma\quad (2)$$

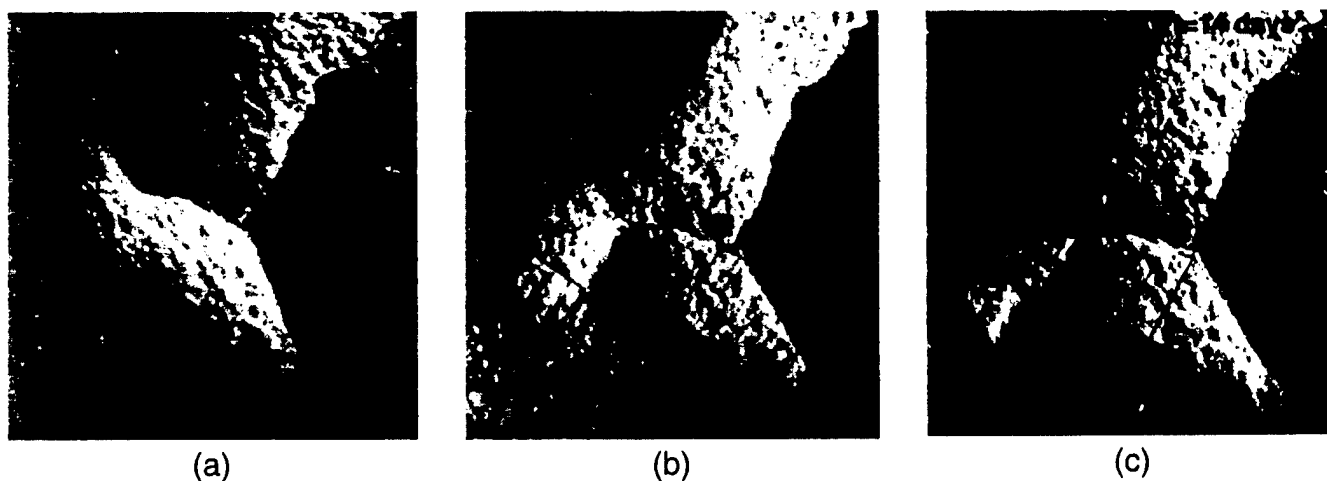


Fig. 2. Higher magnification images of one branch of the buckling when it was first noticed (left) and then at the days indicated.

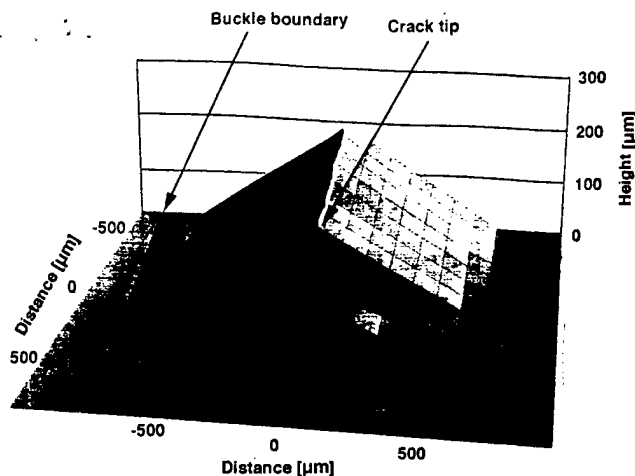


Fig. 3. Three-dimensional plot of the height of the TBC surface in and around the buckle propagating along the direction OA in Fig. 2. Crack tip is point O in Fig. 2.

where Π_{ii} is the trace of the piezospectroscopic coefficient tensor that has a value of $7.50 \text{ cm}^{-1} \cdot \text{GPa}^{-1}$.⁷

The variation in residual biaxial stress along the length of the buckle in the direction OA of the crack is shown in Fig. 6 at $t = 0, 2$, and 7 d . The location of the crack tip along the ridge of the buckle at the three times is also noted. All three sets of residual stress data show similar behavior, namely that, in the buckled portion, the stress is low ($\sim 400 \text{ MPa}$), whereas, well

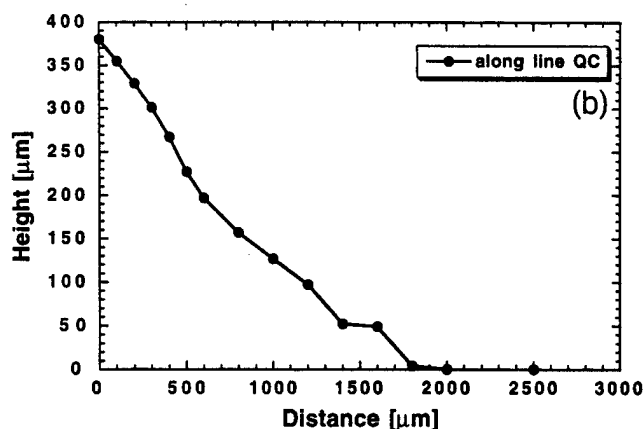
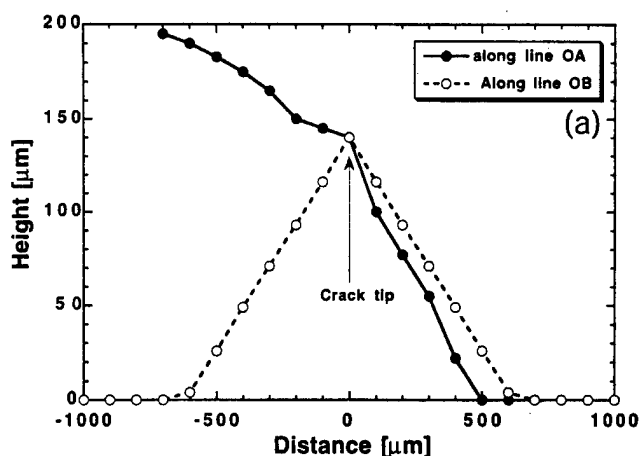


Fig. 4. Height profile along (a) lines OA and OB and (b) line OC in Fig. 2.

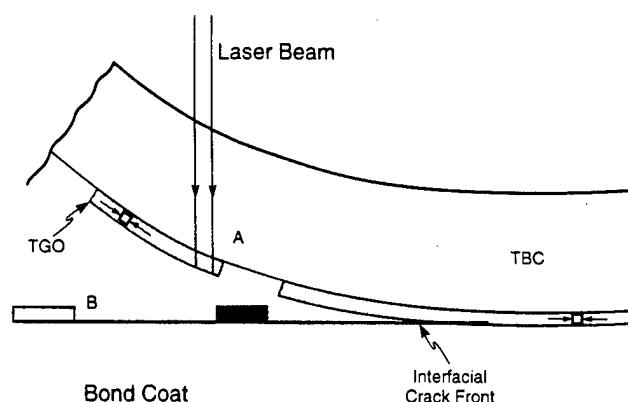


Fig. 5. Schematic diagram of the optical probing of the residual stress distribution in the thermally grown Al_2O_3 beneath the TBC and along the buckled regions. Spectra can be obtained through the TBC from the Al_2O_3 attached to the TBC, such as at point A. Experiments indicate that the spectra could not be obtained from the Al_2O_3 attached to the bond coat, such as at B, because of the air gap between the Al_2O_3 and the TBC.

ahead of the buckle, the residual stress is very high ($\sim 4 \text{ GPa}$). In these two identifiable regions, luminescence consists of two distinct lines, corresponding to the $R1, R2$ doublet, and the frequency shift of the $R2$ line is plotted as the solid symbols in the figure. In between the two regions, the luminescence can be deconvoluted into four distinct lines, a $R1, R2$ doublet with a small shift and a second doublet with a larger shift. The larger shifts are plotted as the open symbols in the figure. Our interpretation of this luminescence is that it is recorded from the vicinity of the interfacial crack front with the luminescence being recorded simultaneously from both the cracked (buckled) and uncracked portions, i.e., highly stressed and less highly stressed regions. This region is designated as the decohesion front in Fig. 6. (In this region, the stress is unlikely to be pure biaxial, and, therefore, the nominal biaxial stress is plotted in the figure.) Examination of the data indicates that the decohesion front advances over the period of measurement from a position $750 \mu\text{m}$ in front of the initial crack tip (point O) to $1100 \mu\text{m}$ 2 d later and then to $1400 \mu\text{m}$ 5 d later. Subsequently, no further advance of the decohesion crack occurred in this area of the spalling pattern, although buckling and spalling progressed elsewhere. (Because the TBC is opaque, the decohesion front and the buckle boundary cannot be observed directly.)

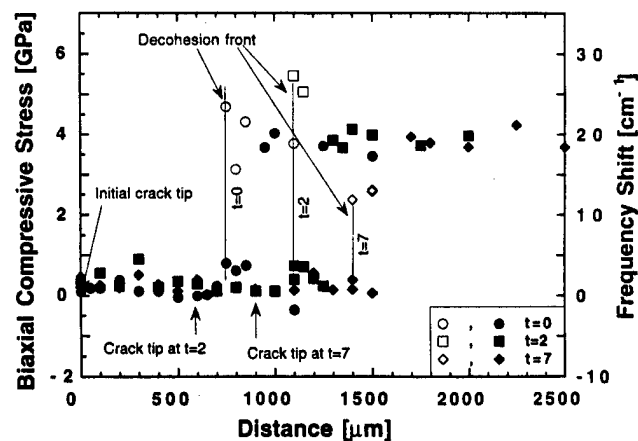


Fig. 6. Variation in residual stress in the thermally grown Al_2O_3 as a function of position along the buckle in the direction OA. Distance is measured from the initial position of the tip of the ridge crack. O. Abrupt rise in residual stress corresponds with the position of the decohesion front, i.e., the buckle boundary.

The variation in residual stress in a direction perpendicular to the buckle (and ridge crack) direction is shown in Fig. 7. A residual stress distribution similar to that found along the buckle direction (Fig. 6) is seen. The most important difference is that the decohesion front advances in this case from a position 700 μm from point O to a position 1600 μm from it in the first 2 d, and then does not advance further. A similar variation in residual stress is observed along the line QC, but no advance of the buckle along this direction is noted.

The residual stress (~ 4 GPa) in the TGO in the regions of the TBC well ahead of the buckle boundary is the same as the intact region elsewhere on the sample, suggesting that the region ahead of the buckle is undamaged. The numerical value of the residual stress in the Al_2O_3 is similar to that measured on other TBCs;⁶ it is a combination of the thermal expansion mismatch stress, primarily with the underlying superalloy, and growth stress in the oxide. The compressive residual stress, σ_{or} , in the Al_2O_3 attached to the buckled portions of the TBC is almost constant from one position to another, at ~ 400 MPa. The elastic modulus of electron-beam-deposited TBCs, in particular their biaxial modulus parallel to the bond-coat/TBC interface, is not known, but its columnar microstructure with a high density of intercolumnar voids and gaps suggests it is very low, much smaller than the modulus of dense ZrO_2 (~ 200 GPa). (A very high biaxial compliance is, in fact, a design requirement of TBCs.) This supposition is supported, indirectly, by microhardness measurements made perpendicular to the TBC surface.⁸ Hardness derived in this way is ~ 0.75 GPa, as compared to the hardness of dense ZrO_2 of ~ 10 GPa. The indentations also exhibit considerable crushing, suggesting that the true hardness is even lower.

In fact, the elastic modulus of the TBC, E_{TBC} , can be estimated from the value of the residual stress in the Al_2O_3 TGO phase, σ_{or} , after separation from the bond coat but remaining attached to the TBC. This is the value shown in Fig. 6 for the regions that have buckled. Using the standard thermal stress equation for a composite laminate,

$$\sigma_{\text{or}} = \frac{E_0}{1 - \nu_0} \frac{(\alpha_0 - \alpha_{\text{TBC}})}{1 + R} \Delta T \quad (3)$$

where R is the ratio

$$R = \frac{E_0}{E_{\text{TBC}}} \left(\frac{1 - \nu_{\text{TBC}}}{1 - \nu_0} \right) \frac{h_0}{h_{\text{TBC}}} \quad (4)$$

and where E_0 is the modulus of the Al_2O_3 (~ 380 GPa), ν_0 the Poisson ratio, and h_0 and h_{TBC} the thicknesses of the Al_2O_3 (~ 0.5 μm) and the TBC (~ 140 μm), respectively. ΔT is the difference between the temperature at which the TBC is de-

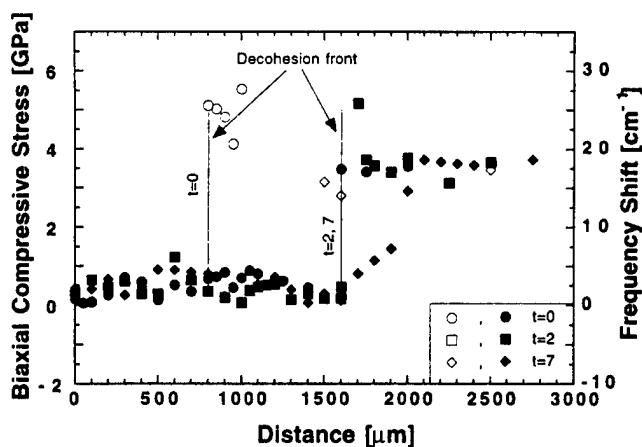


Fig. 7. Variation in residual stress in the thermally grown Al_2O_3 as a function of position along the direction OB, perpendicular to the buckling direction.

posited ($\sim 1000^\circ\text{C}$) and room temperature. Using these values, and assuming that the Poisson ratio of the Al_2O_3 and the TBC are the same (~ 0.25), the biaxial elastic modulus of the TBC is estimated to be ~ 1 GPa.

(3) Fracture Surface Observations

After a portion of the spalled TBC had completely separated from the sample, the fracture surface revealed by the separation was examined by both luminescence and scanning electron microscopy. By probing the luminescence on the fracture surface on the alloy side, we determined that it was partially covered with $\alpha\text{-Al}_2\text{O}_3$ with other regions free of any Al_2O_3 . The fracture surface is shown more clearly in the scanning electron micrographs of Fig. 8, which reveal portions of bare bond coat with the rest of the surface covered with fractured Al_2O_3 . (These assignments were confirmed by energy-dispersive X-ray analysis.) There were two other notable features of the exposed surface. One was the appearance of grain impressions in the bare bond coat, interpreted to correspond to the grains in the matching Al_2O_3 phase. The other surprising feature was that the Al_2O_3 surface exhibited no fracture markings but rather had the appearance of a free oxide surface. Examination of the underside of the TBC spalled from the

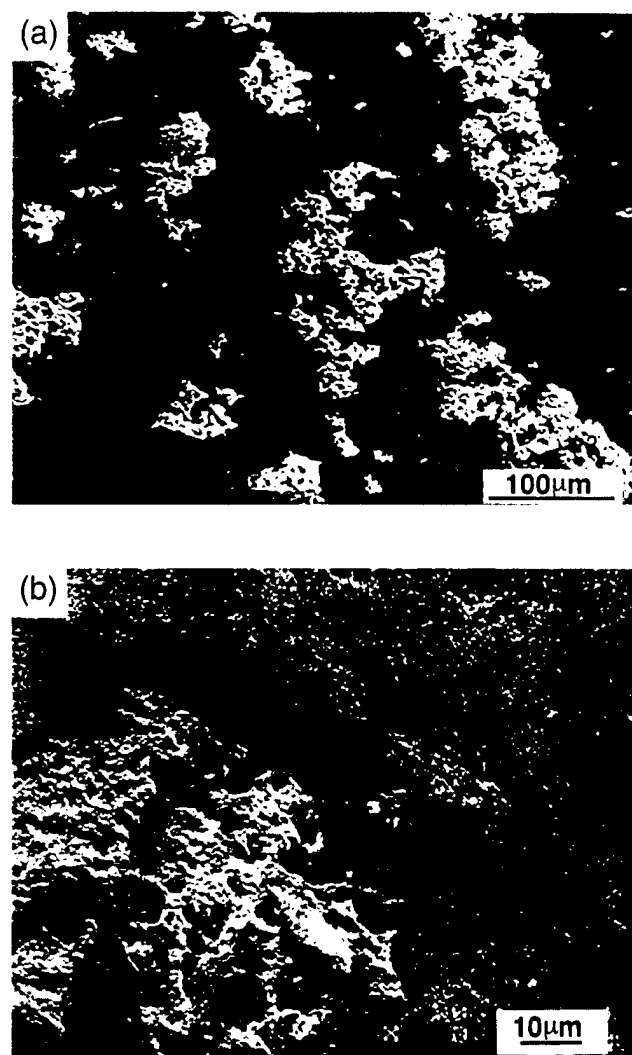


Fig. 8. Surface on the alloy side exposed by the spalling away of the TBC: (a) low-magnification image revealing that the surface is principally covered by the thermally grown oxide but also has regions in which the bond coat is exposed (the bright regions) and (b) higher-magnification image showing grain impressions in the bond coat and the surface of the thermally grown Al_2O_3 . (Scanning electron micrographs.)

sample revealed it was principally ZrO_2 with patches of Al_2O_3 , as shown in the low-magnification image in Fig. 9(a) taken from close to the edge of one of the spalled flakes of TBC so as to also image the ZrO_2 columns of the TBC. Although quantitative comparisons were not made, the areal density of the Al_2O_3 patches corresponded to that of the bare bond coat seen on the exposed surface on the alloy. Closer examination revealed that the majority of the Al_2O_3 surface had the morphology of a free surface with the angular features of individual grains clearly delineated as shown in Fig. 9(b). In the image, as elsewhere on the underside of the TBC, the morphology of the ZrO_2 surface suggested that it also had been a free surface and exhibited no indications of being a fracture surface. Taken together with observations of the Al_2O_3 surface on the exposed alloy, these observations suggested that, before failure by TBC buckling, there was actually very little contact between the TBC and the underlying bond coat. Then, when failure occurred, it was by sequential fracture, at the bond-coat/TGO interface, of the fully bonded regions. The process is shown schematically in Fig. 10. The reason for the areas in which there was no bonding between the ZrO_2 TBC and the TGO on the bond coat is not known. However, one can surmise that it was due to the densification of the metastable Al_2O_3 , initially formed in the heating stages prior to coating, as it transformed to $\alpha\text{-Al}_2\text{O}_3$ after TBC deposition.

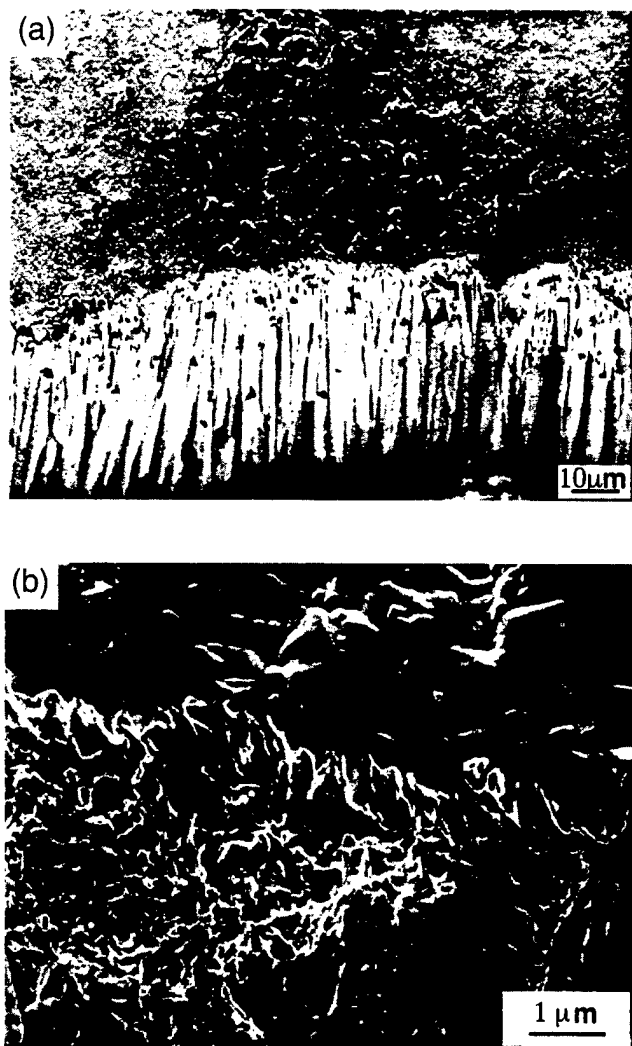


Fig. 9. (a) Underside of the TBC after spalling away. Surface is principally ZrO_2 with patches of attached thermally grown Al_2O_3 . (b) Higher-magnification image reveals the ZrO_2 surface is porous with no indication of fracture and the alumina surface has the granular appearance of an oxide/metal interface formed by oxidation of a metal.

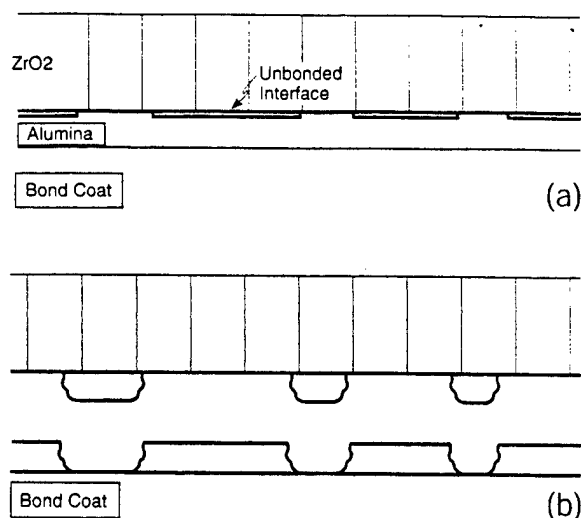


Fig. 10. Schematic representation of the TBC/ Al_2O_3 /bond-coat system before and after fracture (not to scale). Postspalling microscopy observations (Figs. 8 and 9) suggest that, before failure, the TBC was attached only to the Al_2O_3 over a small fraction of the entire coated area. Failure then occurred by the successive fracture of the intact regions at the bond-coat/ Al_2O_3 interface.

III. Discussion and Implications

Optical microscopy observations and the associated topographic measurements indicate that the TBC failure propagates first by the extension of a buckled region followed by cracking at the ridge of the buckle and then of the coating at the buckle boundaries. Once ridge and boundary cracking of the TBC have occurred, the coating is then free to detach. Failure propagation is thus macroscopically similar to that observed in the failure of highly stressed thin films under compression, such as coatings⁹ and diamond films on silicon substrates.¹⁰ Examination of the surfaces exposed by spalling reveals that buckling propagates by the successive failure of those regions of TGO attached to both the bond coat and the TBC. This is supported by the matching morphology of the patches of Al_2O_3 on the TBC and the bare bond coat on the alloy side and, in turn, suggests that the failure occurs at the Al_2O_3 /bond-coat interface and does so by moisture-enhanced subcritical crack growth, because the Al_2O_3 grain features are preserved. The propagation of the buckle by a subcritical crack growth mechanism is manifest not only in the appearance of the buckle with time but also in the redistribution of the residual stress in the TGO with time (Figs. 6 and 7).

Piezoelectroscopic measurements of the residual stress and scanning electron microscopy observations provide the quantitative data needed to estimate the fracture energy of the TGO/bond-coat interface under propagation conditions. Optical microscopy observations indicate that the spall propagates under approximately steady state and that the width of the buckled region remains approximately constant. Under such conditions, we idealize the propagation as shown in the plan view in Fig. 11 and apply the mechanics of buckling worked out in considerable detail for different types of buckling.¹¹⁻¹⁴ Of the analyses, that by Thouless¹⁴ is most appropriate, because it includes the propagation of a crack along the buckle ridge as well as the buckling itself. Using this analysis and recognizing that, when the buckle extends by a distance Δx under steady-state conditions, the elastic strain energy in the TGO is partially relieved and the interfacial fracture energy can be obtained from the difference in elastic strain energy between an area $2b(\Delta x)$ ahead of the propagating buckle and the same area after buckling,

$$G_E = \frac{h(1-\nu^2)}{2E} \left[\sigma_0 - \frac{\sigma_1}{4} \right]^2 f \quad (5)$$

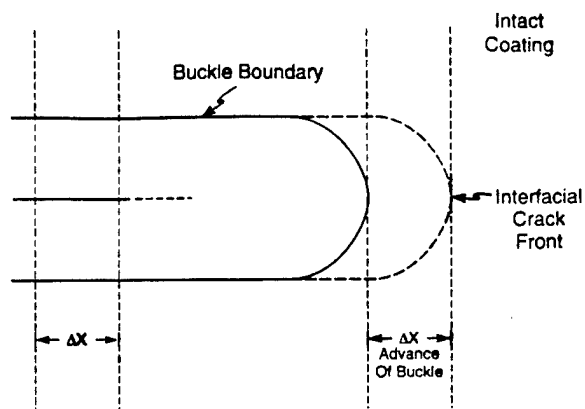


Fig. 11. Schematic representation of a buckle propagation used to estimate the crack driving force and, hence, the interfacial fracture resistance.

where

$$\sigma_1 = \frac{\pi^2 E}{12(1-\nu^2)} \left(\frac{h}{b}\right)^2 \quad (6)$$

and where σ_0 is the residual stress in the film prior to buckling, σ_1 the critical buckling stress, E the elastic modulus, h the film thickness, and b the half-width of the buckle. The additional term f is the fraction of the total buckle area that fractures and is included to account for the observation that only a portion, f , of the TBC/TGO/bond-coat interface is apparently intact before failure. From microscopy observations, this factor is determined to be 0.22 using a commercial image analyzer. From the piezospectroscopic measurements and calculations of the critical buckling, $\sigma_0 \gg \sigma_1$, Eq (5) can be approximated as

$$G_E = \frac{\sigma_0^2 h(1-\nu^2)}{2E} f \quad (7)$$

This expression can be evaluated by assuming that the elastic strain energy in the ZrO_2 TBC is negligible. This is reasonable despite its significant thickness because of its exceptionally low elastic modulus. There are, unfortunately, no values in the open literature for the biaxial elastic modulus of electron-beam-deposited TBCs. (In fact, this remains an unanswered challenge, because the in-plane biaxial modulus determines the compliance of the TBC when subjected to the very large thermal mismatch strains.) However, as described in Section II(2), the value of the residual stress in the Al_2O_3 remaining attached to the TBC is consistent with a biaxial modulus of the TBC of ~ 1 GPa, which is considerably smaller than the modulus of dense Y_2O_3 -stabilized ZrO_2 . This low value for the biaxial modulus of the TBC is also consistent with the buckle profiles (Fig. 4), which show that the buckled material is straight and, hence, not under appreciable bending moment. The piezospectroscopic measurements indicate that the residual biaxial stress in the TGO in the intact region is ~ 4 GPa, whereas after the buckle front passes, the residual biaxial stress falls to ~ 0.4 GPa. Assuming that the elastic modulus of the TGO is ~ 380 GPa and its thickness is $0.5 \mu\text{m}$, and using the expression above, the interfacial fracture energy is estimated to be $\sim 9 \text{ J}\cdot\text{m}^{-2}$. This compares quite fortuitously with the fracture energy of the nickel/sapphire interface of $10 \text{ J}\cdot\text{m}^{-2}$.¹⁵ Although there are several other reports in the literature of the fracture resistance of metal/ceramic interfaces,^{16–17} including observations of subcritical crack growth in the presence of moisture,¹⁷ the authors

are unaware of any other work on the fracture resistance of the nickel/ Al_2O_3 interface, the interface pertinent to the oxide/bond-coat interface.

For some reason, presumably associated with its deposition as discussed above, the TBC in this particular instance is not well-attached to the bond coat and, as a result, may not be typical of high-performance TBCs. This may be why it is possible to observe the slow propagation of the TBC in this case. However, the relatively low fracture energy of the Al_2O_3 /bond-coat interface and its susceptibility to moisture-enhanced crack growth suggest that it is of utmost importance to shield this interface from moisture. In retrospect, it is possible that the failure observed was initiated when the sample was dropped, thereby damaging the TBC at the edge and exposing the Al_2O_3 /bond-coat interface. This suggests, in turn, that systematic studies of subcritical growth in TBC systems at different humidities be undertaken, together with the use of deliberately introduced controlled defects to initiate failure under prescribed conditions.

IV. Conclusions

Room-temperature time-dependent failure of an electron-beam-deposited ZrO_2 TBC occurs over a period of several weeks. By combining optical and scanning electron microscopy observations with piezospectroscopic measurements, it is concluded that the observed macroscopic failure by buckling and subsequent spalling of the TBC is mediated by subcritical crack growth along the TGO/bond-coat interface, presumably enhanced by the presence of moisture. Fracture energy of the interface is estimated to be $\sim 9 \text{ J}\cdot\text{m}^{-2}$.

Acknowledgments: The authors are grateful to Dr. Tolpygo for invaluable discussions, to Dr. C. Schmid, (University of Trieste) for the image analysis, and to Professor M. Thouless (University of Michigan) for his suggestions after reviewing the original manuscript.

References

- ¹Coatings for High Temperature Structural Materials. National Academy Press, Washington, DC, 1996.
- ²Q. Ma and D. R. Clarke, "Stress Measurement in Single Crystal and Polycrystalline Ceramics Using Their Optical Fluorescence," *J. Am. Ceram. Soc.*, **76** (6) 1433–40 (1993).
- ³Q. Ma and D. R. Clarke, "Piezo-Spectroscopic Determination of Residual Stresses in Polycrystalline Alumina," *J. Am. Ceram. Soc.*, **77** (2) 298–302 (1994).
- ⁴D. M. Lipkin and D. R. Clarke, "Sample-Probe Interactions: Sampling Microscopic Property Gradients," *J. Appl. Phys.*, **77** (5) 1855–63 (1995).
- ⁵D. M. Lipkin and D. R. Clarke, "Measurement of the Stress in Oxide Scales Formed by Oxidation of Aluminum-Containing Alloys," *Oxid. Met.*, **45** (3/4) 267–80 (1996).
- ⁶R. Christensen, D. M. Lipkin, D. R. Clarke, and K. Murphy, "Non-Destructive Evaluation of Oxidation Stresses through Thermal Barrier Coatings Using Cr^{3+} Piezospectroscopy," *Appl. Phys. Lett.*, **69** (24) 3754–56 (1996).
- ⁷J. He and D. R. Clarke, "Determination of the Piezo-Spectroscopic Coefficients for Chromium-Doped Sapphire," *J. Am. Ceram. Soc.*, **78** (5) 1347–53 (1995).
- ⁸P. Heydt, M.S. Thesis, University of California, Santa Barbara, CA, to be published.
- ⁹G. Gille, "Strength of Thin Films and Coatings"; pp. 420–72 in *Current Topics in Materials Science*, Vol. 12. Edited by E. Kaldis. North Holland, Amsterdam, The Netherlands, 1985.
- ¹⁰D. Nir, "Stress Relief Forms of Diamond-like Carbon Thin Films on Silicon," *Thin Solid Films*, **112**, 41–49 (1984).
- ¹¹A. G. Evans and J. W. Hutchinson, "On the Mechanics of Delamination and Spalling in Compressed Films," *Int. J. Solids Struct.*, **20**, 455–66 (1984).
- ¹²J. W. Hutchinson and Z. Suo, "Mixed Mode Cracking in Layered Materials," *Adv. Appl. Mech.*, **29**, 63–91 (1992).
- ¹³M. D. Thouless, J. W. Hutchinson, and E. G. Liniger, "Plane Strain, Buckling-Driven Delamination of Thin Films," *Acta Metall. Mater.*, **40**, 2639–49 (1992).
- ¹⁴M. D. Thouless, "Combined Buckling and Cracking of Films," *J. Am. Ceram. Soc.*, **76** (11) 2936–38 (1993).
- ¹⁵J. Stolken and A. G. Evans, to be published.
- ¹⁶"Proceedings of the International Symposium on Metal/Ceramic Interfaces" (special issue), *Acta Metall. Mater.*, **40**, S1–S368 (1992).
- ¹⁷T. Oh, R. M. Cannon, and R. M. Ritchie, "Sub-critical Crack Growth along Ceramic-Metal Interfaces," *J. Am. Ceram. Soc.*, **70** (12) C-352–C-355 (1987).

On the Measurement of Strain in Coatings Formed on a Wrinkled Elastic Substrate

Xiao-Yan Gong* and D. R. Clarke*

Received December 9, 1997

Highly stressed coatings, such as those formed by oxidation can, on occasion, wrinkle. Such wrinkling has been suggested as a mode of deformation by which the overall strain energy in a compressively stressed coating can be reduced. One of the consequences of wrinkling is that the strain in the coating does not remain independent of position, but rather varies over the wavelength of the wrinkling. The strain variation caused by sinusoidal wrinkling is calculated using finite-element methods and the effects on both photostimulated Cr^{3+} luminescence piezospectroscopy measurements and X-ray measurements calculated. Wrinkling is shown to decrease the elastic-strain-energy density in the coating. A direct measure of the decrease is the shift in the R2 Cr^{3+} luminescence line and the X-ray diffraction peaks. Wrinkling of a compressive coating also causes stresses to be created perpendicular to the coating-substrate interface, tensile at the crests in the wrinkles, and compressive stress at the troughs.

KEY WORDS: residual stresses; finite-element modeling; wrinkling; strain measurements.

INTRODUCTION

It is a common observation in the oxidation literature that oxide scales formed on the flat surfaces of certain metals do not remain flat during oxidation but instead wrinkle. Such wrinkling is seen on both single crystals of

*Materials Department, College of Engineering, University of California, Santa Barbara, California 93106-5050.

FeCrAl¹ and on a variety of polycrystalline alloys.²⁻⁴ An example of wrinkling is shown in Fig. 1. The origin of this wrinkling instability has been attributed to the presence of large compressive stresses in the oxide scale at the oxidation temperature and a linear stability analysis has been presented by Suo⁵ showing that wrinkling is a form of morphological instability driven by relaxation of the elastic-strain energy in the scale. In Suo's model, the kinetics of relaxation are determined by diffusion along the oxide-metal interface, but other relaxation mechanisms may pertain in specific materials. The observation of wrinkling of the scale raises two questions. The first is what is the elastic strain in the scale and how does it vary with the wrinkling geometry, for instance, the wavelength and amplitude of the wrinkles. The second question is how the strain measured by a number of techniques relates to the elastic-strain energy stored in the wrinkled scale. The elastic-strain energy is important since it is the energy available for propagating cracks or scale delamination.

To illustrate the difficulty posed by wrinkling, consider the strains created in an oxide formed on cooling to room temperature as a result of thermal-expansion mismatch between the oxide and the underlying metal. On a flat surface, the measurement of strain is unambiguous since the strain is not expected to vary spatially over the oxide. Furthermore, it can be assumed that the strain through the thickness of the oxide also does not vary from place to place over the surface. However, when the oxide is not flat then the strains do vary from place to place and there will be variations in strain through the thickness of the oxide. Thus, when a measurement is made of the strain in the oxide using a technique with a spatial resolution that is inferior to the characteristic length scales of the wrinkling, what does this average strain correspond to? Furthermore, how does this average strain relate to the overall elastic-strain energy in the scale, the strain energy that is available to drive scale cracking or decohesion?

In this work we seek to address these questions analytically. For illustrative purposes, we consider how strain measurements made by X-ray diffraction (XRD) and photostimulated Cr³⁺ luminescence-based piezospectroscopy will be affected by wrinkling. (These two techniques are presently the principal ones being used to measure strains in oxide scales.) It is emphasized that wrinkling occurs during oxidation in response to the existence of compressive growth stresses, whose magnitude are presently unknown, and not on cooling. This is a complex process and so we consider here the more general, but much simpler, case of a conformal coating under compression on cooling as a result of thermal-expansion mismatch on a wrinkled substrate. However, the findings can be used to evaluate the driving forces for oxidation-induced wrinkling by comparing the strain distribution and elastic-strain-energy density at successive stages in the evolution of the wrinkling geometry.

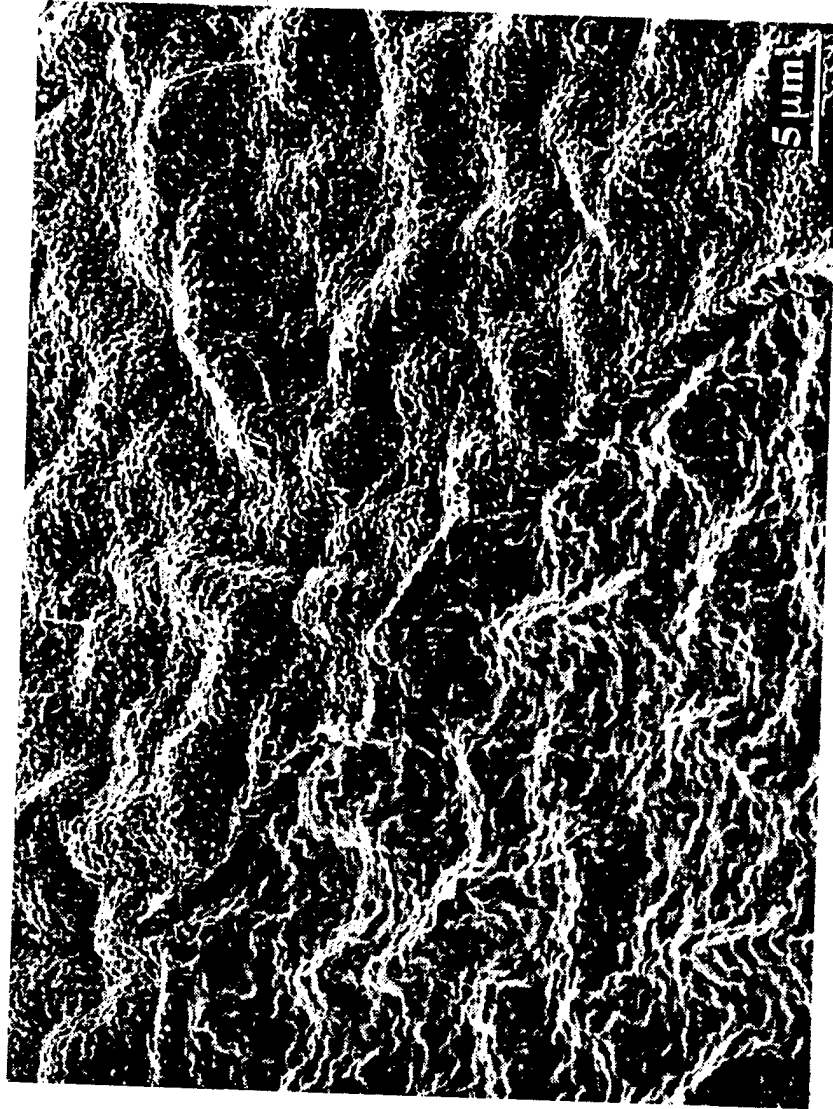


Fig. 1. An example of oxide-scale wrinkling on an FeCrAl alloy produced during oxidation at 1000°C for 70 hr. The oxide has spalled on the bottom left side to reveal the same wrinkled morphology on the underlying metal. Scanning electron micrograph.

Table I. Physical Properties of Oxide Film and Metal Alloy

Materials	Young's modulus (GPa)	Poisson's ratio	Thermal-expansion coefficient
Oxide film	400	0.25	8.0×10^{-6}
Metal alloy	200	0.3	13.7×10^{-6}

STRAIN CALCULATIONS

In calculating the strain distribution within a wrinkled coating or film, the coating is assumed to be attached to a very thick, thermal-expansion-mismatched solid having a sinusoidally varying surface. For simplicity, both the coating and the substrate are assumed to be elastic. The coating is represented by an isotropic elastic material having the physical properties listed in Table I. The properties of the metal are also listed. In developing the residual stress in the coating, the strains in the metal and coating are computed using known thermal-expansion coefficients (appropriate to FeCrAl and aluminum oxide) and a temperature difference of 975°C. The strain distribution is calculated using a commercial finite-element program (ABAQUS). For purposes of computation, symmetry permits a unit cell of one-half of the sinusoid to be analyzed (shown by the dashed region BCDE in Fig. 2). The length scales in the computation are the thickness, H , of the coating, the wavelength, $2L$, and amplitude, A , of the sinusoid and the thickness of the metal. As a check, the biaxial stress and elastic strain energy

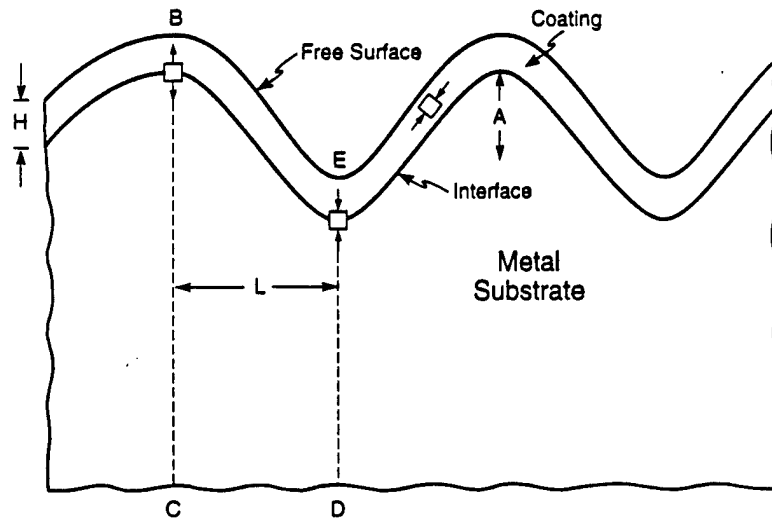


Fig. 2. Geometry used in the finite-element computations. The computational unit cell BCDE is shown within the dashed lines.

Table II. Comparison of Analytical and Finite-Element Results on Flat Film

	Stress (GPa)	Elastic-strain-energy density (MJ/m ³)
Analytical solution	2.964	16.47
Finite-element result	2.937	16.17

in a flat coating were computed and compared with the known, analytical results (Table II). Two geometries were considered: one of generalized plane strain in which the sinusoid varies in the x -direction only and the other the axisymmetric geometry in which a sinusoidal variation with radial distance is assumed. The strains were calculated from the average of nine integration points within each element. The strain-energy densities were calculated directly in each element and then integrated over the whole mesh to derive the total elastic-strain energy.

Detailed computations of the strain distribution throughout the coatings were carried out, including the hydrostatic strains and the strains normal to the mean coating surface. As will be described, the former were used in evaluating the piezospectroscopic shifts and the latter for evaluating the XRD shifts. Where appropriate the stresses in the coating were calculated from the computed strains through the generalized Hooke's law.

The general result is that as the amplitude of the wrinkling increases and the wavelength decreases, the distribution of strain in both the scale and the underlying metal become increasingly inhomogeneous. An example of this is shown in both Figs. 3 and 4 for two different ratios of the wrinkling amplitude and wavelength, one corresponding to a rather small wrinkling and the other with a more pronounced wrinkling. As indicated by the contours of hydrostatic strain in Fig. 3, the spatial variation in strain increases and the numerical values also exhibit a broader variation as the wrinkling is increased. A similar behavior is shown by the normal strains as shown in Fig. 4. In the absence of any wrinkling, there are no stresses perpendicular to the coating-substrate interface, but they are created once wrinkling occurs with tensile stresses at the crests of the wrinkles and compressive stresses at the valleys. These stresses perpendicular to the interface are presented and discussed in detail later. The general trend they exhibit is that their magnitude increases with increasing wrinkling and while the point of maximum tensile stress remains at the coating-metal interface at the crests the point of maximum compressive stress moves from the coating-metal interface toward the coating-air interface.

In Fig. 5, the effect of wrinkling amplitude and wavelength on the elastic-strain-energy density is plotted. As expected, when the wrinkling wavelength

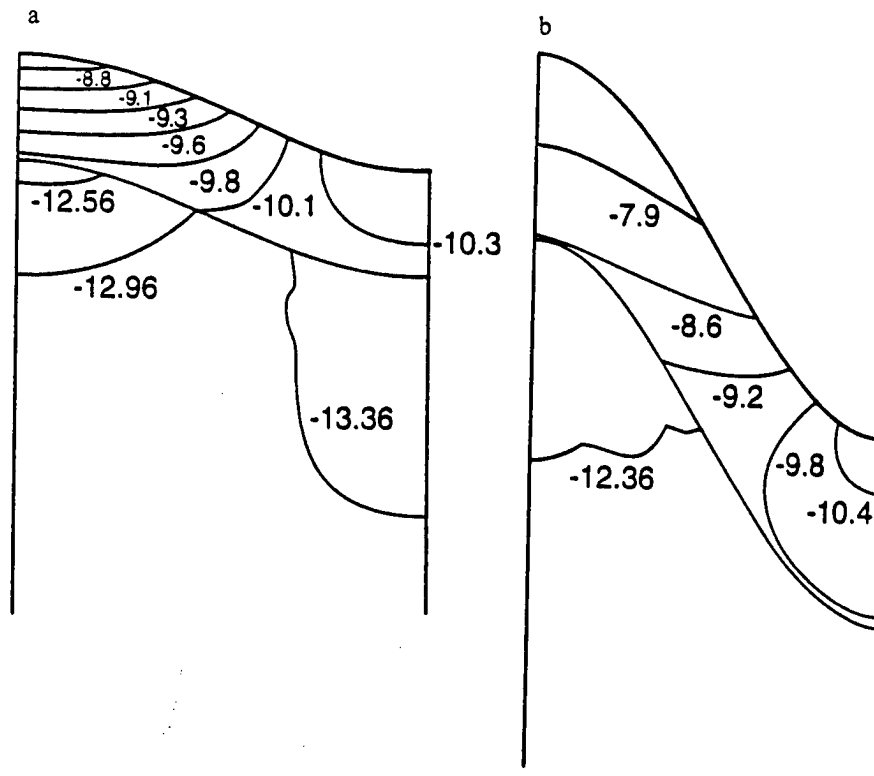


Fig. 3. Contours of the hydrostatic strain distribution in the scale and underlying metal for (a) $A/H = 0.5$, $L/H = 4.0$, and (b) $A/H = 1.0$, $L/H = 2.0$. Contours are in units of 10^{-3} .

is large compared to both the scale thickness and the wrinkling amplitude, the strain energy approaches that of a flat coating. This is a direct consequence of the elastic distortions being small under these conditions. As the wavelength, coating thickness, and amplitude become comparable, the strain energy decreases rapidly. Although the actual values are dependent on the coating thickness, for most combinations of length scales, the curves are just shifted with respect to one another. The exception being when the coating thickness is similar to that of the amplitude, in which case the curves begin to cross.

PIEZOSPECTROSCOPIC ANALYSIS

A detailed description of the piezospectroscopic analysis technique applied to the measurement of stress and strain in polycrystalline aluminum

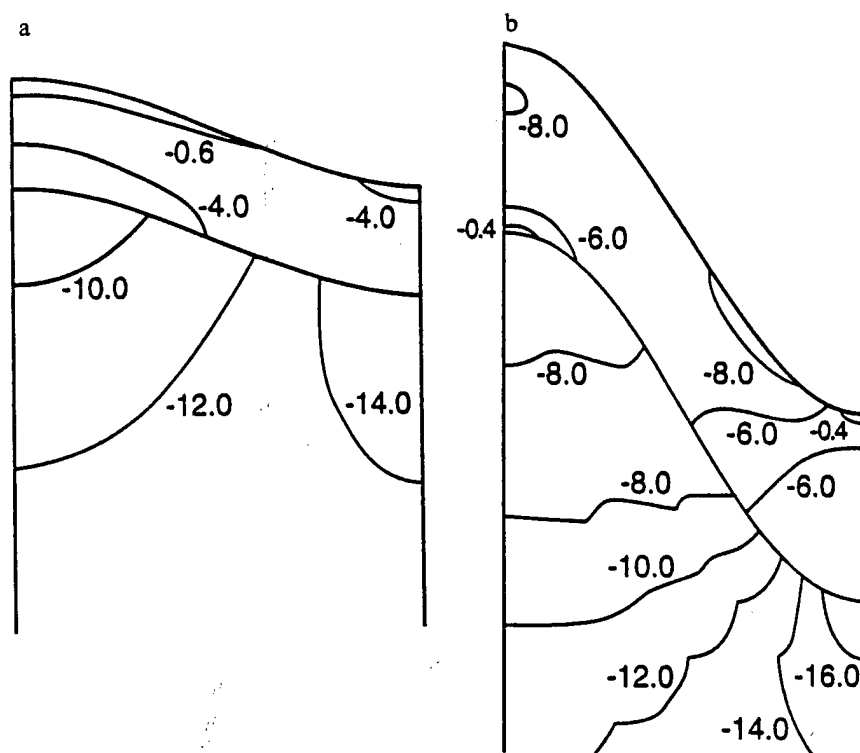


Fig. 4. Contours of the normal strain distribution in the scale and underlying metal for (a) $A/H = 0.5$, $L/H = 4.0$, and (b) $A/H = 1.0$, $L/H = 2.0$. Contours are in units of 10^{-3} .

oxide has been presented elsewhere.^{6,7} In brief, the characteristic photo-stimulated *R*-line luminescence, from trace amounts of Cr^{3+} in solid solution, is shifted from their unstrained frequencies when aluminum oxide is strained. The shift in frequency of the R1 and R2 lines, which in unstrained aluminum oxide are at 14402 and 14432 cm^{-1} , respectively, at room temperature, is related to the strain, to first order, by the relation:

$$\Delta\nu = \Pi_{ij}(\epsilon)\epsilon_{ij} \quad (1)$$

where $\Pi_{ij}(\epsilon)$ are the piezospectroscopic strain coefficients. In polycrystalline alumina, provided the luminescence is collected from a region containing a sufficient number of grains, considerable simplification of Eq. (1) occurs and the piezospectroscopic shifts are simply given in terms of the strain averaged over the probed volume by:

$$\overline{\Delta\nu} = \frac{1}{3}\Pi_{ij}(\epsilon)\langle\epsilon_{ii}\rangle \quad (2)$$

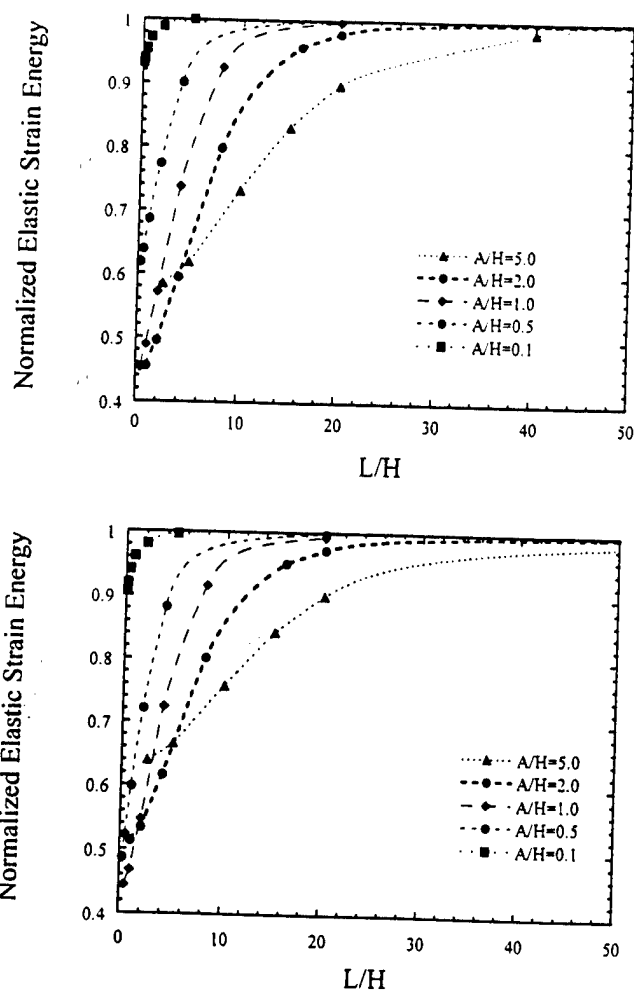


Fig. 5. Normalized elastic-strain-energy density as a function of the wrinkling wavelength, L/H , under axisymmetric (top) and generalized plane-strain conditions (bottom).

in other words, the shift is directly proportional to the trace of the average strain tensor, $\epsilon_{ii} = \epsilon_{rr}$, namely the hydrostatic component of the strain. The value of the trace of the piezospectroscopic tensor, $\Pi_{ii}(\epsilon)$, has been determined to be 5906 cm^{-1} unit strain.⁸

If the strain varies over the volume of oxide probed, then the luminescence signal $I(\nu)$ is the convolution of the luminescence given by Eq. (2) and the variation in strain within the volume from which the luminescence

is collected:

$$I(\nu) \propto \int \varphi\{\nu - \nu_0[\epsilon(\vec{r})]\} d\vec{r} \quad (3)$$

where $\varphi(\nu)$ is the luminescence peak from a strain-free alumina and $\nu_0[\epsilon(\vec{r})]$ is the constitutive relation between the frequency and the spatial variation in the strain field, $\epsilon(\vec{r})$.

Using these equations it is possible to calculate the luminescence peak shape and frequency shift from the strain distribution calculated using the finite-element method above. The methodology adopted is as follows: At each element the average hydrostatic strain, $\langle\epsilon_{rr}\rangle$, is calculated as well as the volume. From these values, the total luminescence intensity as a function of frequency is then obtained by adding the contributions from the individual elements:

$$I(\nu) = \frac{\sum_i V_i \varphi_i\{\nu, \nu_0[\langle\epsilon_{rr}\rangle_i]\}}{\sum_i V_i} \quad (4)$$

In calculating the effect of wrinkling on the piezospectroscopic shifts, we have used the experimentally measured luminescence from a stressed-alumina scale on FeCrAl(Y) (which forms a flat scale) to represent the frequency shift from a flat coating and the measured luminescence from a stress-free sapphire to represent the strain-free spectrum. In both cases, the R2 luminescence peak can be fit with a pseudo-Voigt function. The width of the peak from the unstrained sapphire is 11.16 cm^{-1} , whereas that from the stressed, flat scale was 21.0 cm^{-1} .

The calculated frequency shift as a function of wrinkling amplitude and wavelength is shown in Fig. 6 and indicates a strong sensitivity of the frequency shift to the geometry of the wrinkling. In fact, the shapes of the curves bear a strong similarity to the strain-energy curves of Fig. 5. This is borne out by Fig. 7 in which the piezospectroscopic shift is plotted against the normalized elastic-strain energy. All the computed curves collapse onto a single curve that can be expressed analytically as a quadratic function of the form:

$$U_E = a + b\overline{\Delta v} + c(\overline{\Delta v})^2 \quad (5)$$

where a , b , and c are coefficients. For the axisymmetric case $a = 1.5$, $b = -0.25$, and $c = 0.015$. For the generalized plane-strain case, $a = 0.72$, $b = -0.10$, and $c = 0.009$.

Wrinkling also affects both the broadening of the luminescence peak and the Lorentzian fraction. The effects are not large and so in the interests of space are not presented here.

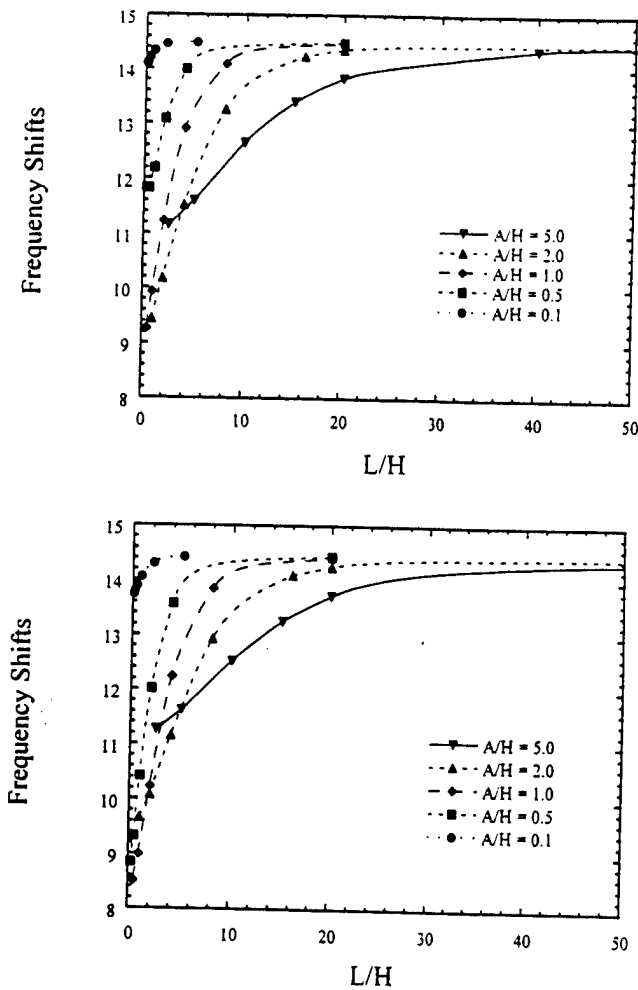


Fig. 6. Computed shift in luminescence frequency under axisymmetric (top) and generalized plane-strain (bottom) conditions. The frequency shift is relative to that from a strain-free scale.

STRAIN MEASUREMENT BY X-RAY DIFFRACTION

The calculation of the XRD spectra from a wrinkled coating is similar in many respects to that for the calculation of the luminescence spectra. The main difference being that since XRD is sensitive to the lattice spacing, rather than the trace of the strain tensor, the shift is proportional to the principal strain perpendicular to the scattering vector. Assuming that the

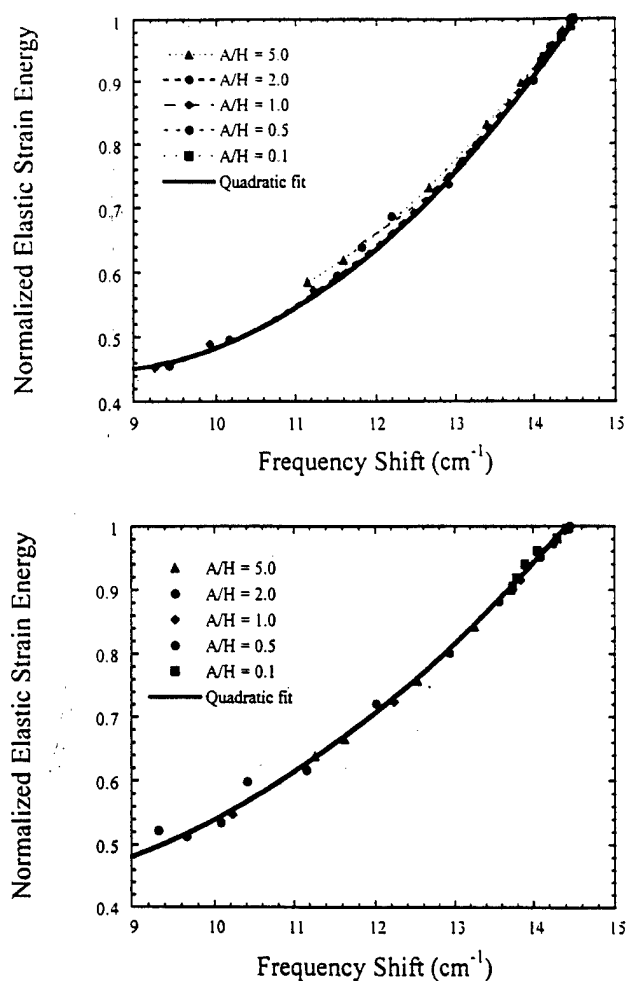


Fig. 7. Relationship between the normalized elastic-strain energy in the scale and the frequency shift of the luminescence line. As in the previous figure, the frequency shift is relative to a strain-free scale. The solid line is a quadratic fit to the computed data.

strain will be measured by the shift in diffraction peaks recorded from the sample in the $\Theta - 2\Theta$ Bragg reflection geometry, the pertinent strain is the normal strain perpendicular to the average surface plane, as shown schematically in Fig. 8. In this diffraction geometry, the position of the XRD peak center θ_0 is related to strain normal to the average wrinkled scale plane

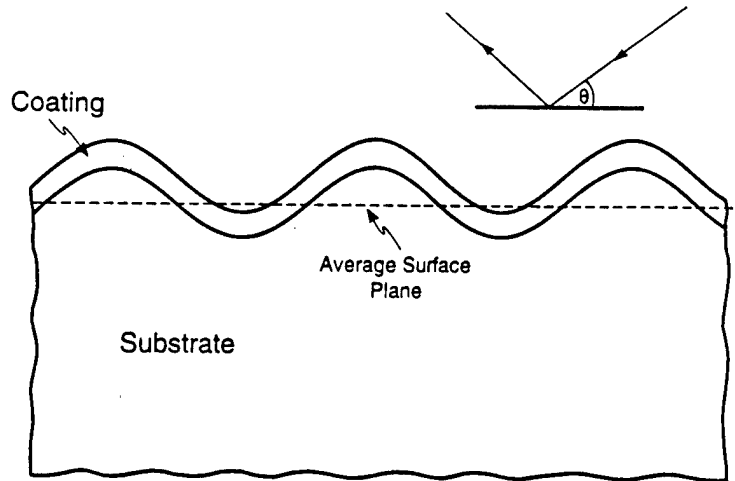


Fig. 8. Schematic diagram of the X-ray diffraction geometry and the wrinkling geometry. In a Θ - 2Θ diffraction geometry, it is the strain in the scale normal to the diffracting plane that causes a shift in the diffraction peak.

by the Bragg condition,

$$2d(1 + \epsilon) \sin \theta_0 = \lambda \quad (6)$$

where d is the unstrained lattice spacing and ϵ is the normal strain.

In calculating the diffraction intensity as a function of diffraction angle, we assume that the coating is polycrystalline and, as with the luminescence calculations, the diffracted intensity comes from a large number of individual grains within the coating. We also assume that the grain size is small or comparable with the thickness of the coating so that the full strain distribution within the wrinkled film is sampled. The latter is not a severe restriction provided the grain size is not smaller than the coherence length for XRD. If it is, then there will be additional broadening of the X-ray peaks due to local curvatures and a much more sophisticated analysis is required than is presented here. Last, it is also assumed that the coating exhibits no preferential crystallographic texture so that the orientation of any particular lattice plane is randomly distributed throughout the film and, hence, samples the maximum principal strain distribution.

The diffraction line profile is formally the convolution of the diffracted amplitude from the individual grains within the coating. Assuming that the measured intensity as a function of scattering angle, Θ , is the integration of the diffracted intensity from each element weighted by its volume, the

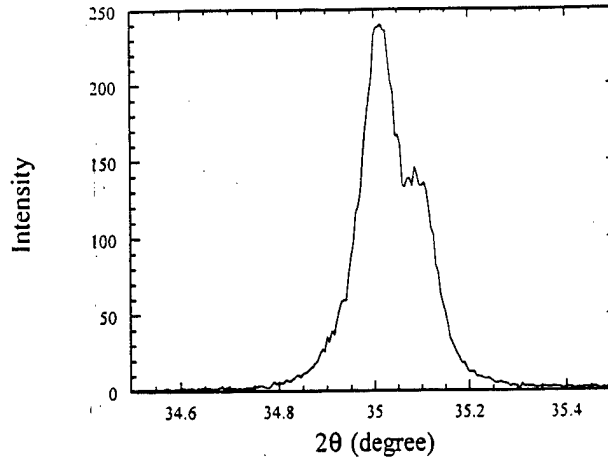


Fig. 9. Typical (104) X-ray peak from a flat, highly-stressed alumina scale formed on a FeCrAl(Y) alloy.

convolution can be replaced by the summation:

$$I(\theta) = \frac{\sum_i V_i \phi_i\{\theta, \theta_0[\langle \epsilon \rangle_i]\}}{\sum_i V_i} \quad (7)$$

where the summation is performed over each element, i , in the mesh and V_i is the volume of the i th element. The function $\phi(\theta)$ describes the intensity of the stress-free peak as a function of diffraction angle.

For the purposes of illustration we again consider the coating to be an oxide scale and specifically consider the shift in the (104) X-ray peak from a flat scale on a FeCrAlY alloy. With copper $K\alpha$ X-rays, the peak was centered at $2\theta = 35.032^\circ$, corresponding to a normal strain in the flat scale of $\epsilon = -4.1293 \times 10^{-3}$ (Fig. 9). The computed shifts of the X-ray peak for a variety of scale thicknesses as a function of wrinkling wavelength are shown in Fig. 10, and includes both the generalized plane strain and axisymmetric cases. As with the luminescence shifts, there is a relationship between the normalized elastic-strain-energy density in the wrinkled scale and the shift in the XRD peaks. However, as shown in Fig. 11, the relationship is also dependent on the amplitude:thickness ratio of the scale. Nevertheless, the shift is proportional to the reduction on the elastic-strain-energy density.

IMPLICATIONS AND DISCUSSION

The finite-element computations clearly indicate that wrinkling decreases the elastic-strain energy in a conformal coating and that the

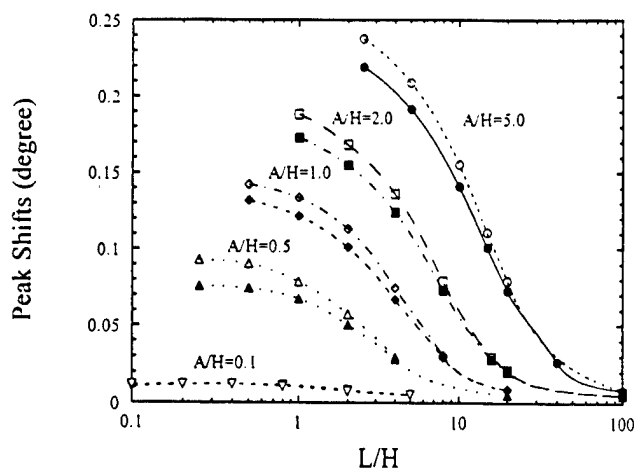


Fig. 10. Shifts in X-ray diffraction peak as a function of wrinkling geometry. Axisymmetric (filled symbols) and generalized plane strain (open symbols).

decrease in strain energy is dependent on both the wavelength and amplitude of the wrinkle. This reaffirms the basis for the linear-stability analysis presented by Suo,⁵ as well as the suggestions in the literature that wrinkling is motivated by decreasing the overall strain energy in the scale. Calculations of both the luminescence frequency and the X-ray lattice parameter show that both are affected by wrinkling. Perhaps most surprising is that there is a direct correlation between the piezospectroscopic shift and the normalized strain energy in the wrinkled scale that pertains irrespective of the actual amplitude and wavelength of the wrinkling. This indicates that the piezospectroscopic shift is a direct measurement of the strain-energy density of the scale and that a detailed knowledge of the wrinkling geometry is not necessary to determine the strain-energy density. A similar relationship pertains for the X-ray measurements but is not independent on the amplitude:thickness ratio.

There are a number of results from the finite-element computations that have particular relevance to understanding the response of materials to oxidation. First, and foremost, is that the decrease in elastic-strain-energy density is accompanied by both increases and decreases in local stress. This is particularly pronounced at the crests and valleys of the wrinkling, where large stresses perpendicular to the oxide-metal interface exist. Thus, as the amplitude of the wrinkling increases, the tensile stress across the metal-oxide interface at the crests of the wrinkle increases. This is of significance since in the absence of wrinkling, there exist no stresses across the metal-

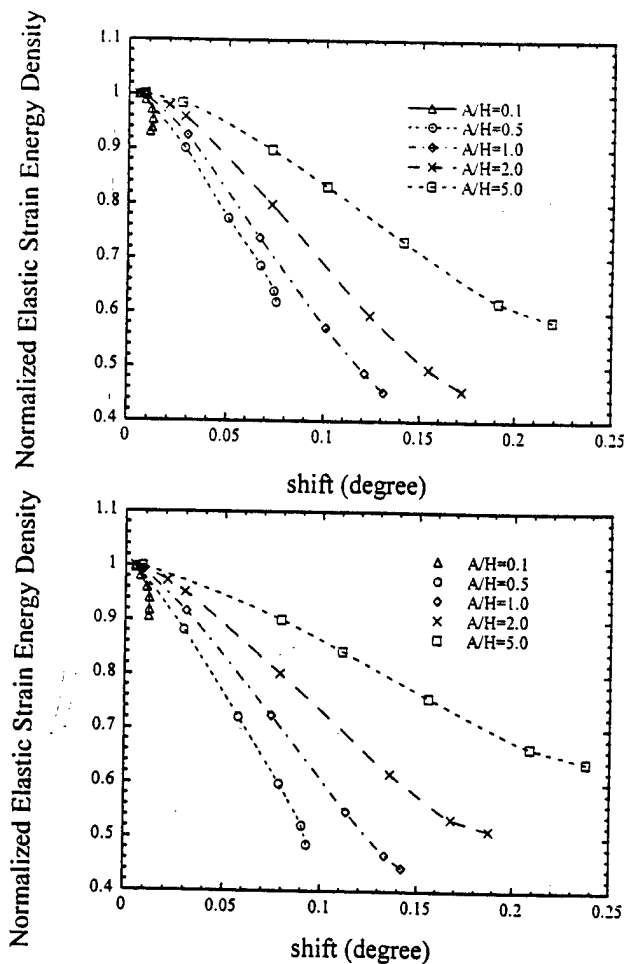


Fig. 11. Relationship between the shift in X-ray peak position and the normalized elastic-strain energy in a wrinkled scale for different amplitudes:thickness ratios of the scale. Axisymmetric (top) and generalized plane strain (bottom).

ceramic interface and, hence, no forces to separate the interface. It is, therefore, of interest to relate the results of the finite-element calculations to those calculated analytically using an idealized geometry, as is discussed in the Appendix. When the scale is thin with respect to the radius of local curvature, one might expect that the oxide can be considered as a thin, stressed membrane by direct analogy with the surface tension in a liquid droplet of radius R . The values of the normal stress across the interface at the crests

and valleys would then be similar to those calculated by force balance using a simple Laplace equation:

$$\sigma_N = \frac{\sigma_b h}{R} \quad (8)$$

where σ_b is the biaxial stress in the scale and R is the effective radius of curvature at the crests of the sinusoidal wrinkle. (For a wrinkle in three dimensions, the numerator would have an additional factor of two.) To evaluate this comparison, the maximum and minimum normal stresses computed at the interface are plotted in Fig. 12 as a function of the local radius. This simple analogy works reasonably well for the generalized plane-strain condition until the normalized radius of curvature is small. The discrepancy at the small radii is a direct result of the neglect of the substantial distortions in the scale away from the crest and valleys and the fact that the scale is no longer thin relative to the other dimensions. In the axisymmetric case, the analogy works well for the tensile stress, but not for the compressive stress when the radius is large. This is believed to be due to the fact that when the radius is large, the local strain state more closely represents a plane-strain condition. Indeed, when the plane-strain solution is used, it fits the compressive data well, as indicated by the dotted line. Another feature of the stress distributions computed is that as the wrinkling increases, the maximum tensile stress always lies at the crest of the sinusoid at the metal-scale interface, whereas the maximum value of the compressive stress moves from the metal-scale interface to the scale-air interface.

A direct consequence of the spatial variation in strain produced by wrinkling is that the strain measured using a particular technique depends on its spatial resolution. Thus, at one extreme, such as with XRD as it is usually implemented where the spatial resolution is far inferior to the wrinkling wavelength, the strain measured is the normal strain averaged over all possible wavelengths of the wrinkling. Interpretation of the strain then requires a knowledge of the wrinkling geometry. Obviously, if no observations are made as to whether a scale is wrinkled or not, then a strain measurement by XRD has rather dubious value. At the other extreme, a technique with a spatial resolution considerably better than the wrinkling wavelength is required to probe the details of the strain distribution and, in particular, to measure the highly-localized strains in the vicinity of the crests and troughs of the wrinkles. This can be achieved with luminescence piezospectroscopy under appropriate conditions. More generally, the strain distribution must be obtained by deconvoluting the measured signal using the probe function for the measurement technique employed.

Another general result with far-reaching consequences is that wrinkling causes gradients in strain well into the underlying metal, typically to

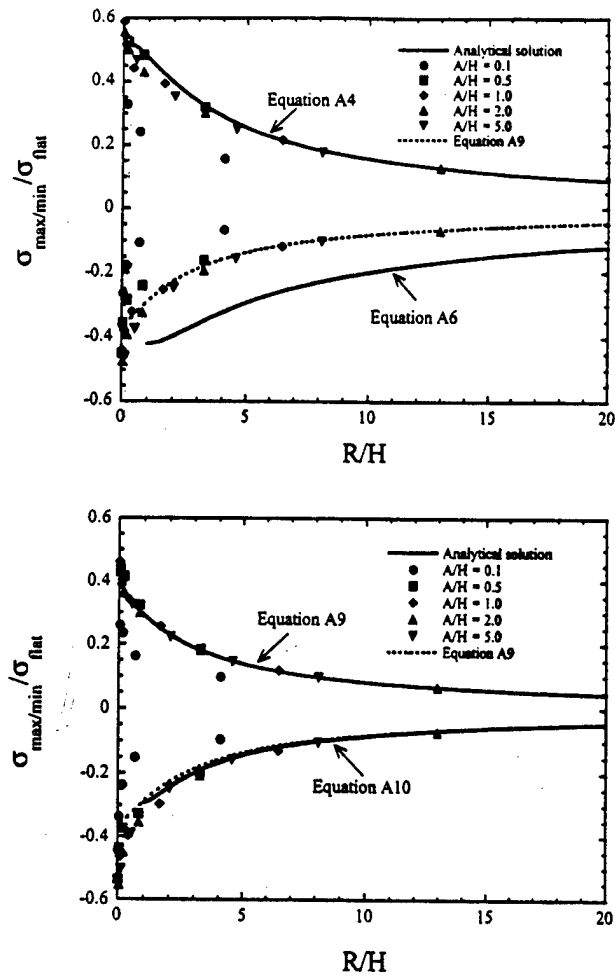


Fig. 12. Normalized maximum/minimum normal stress at the coating-substrate interface as a function of the local curvature of the interface. Axisymmetric (top) and generalized plane strain (bottom).

distances of the order of the wavelength of the wrinkle. The actual distances depend in detail on the constitutive behavior of the metal and the wrinkling geometry and, therefore, must be computed. The consequences are twofold. First, the existence of wrinkling in the scale necessarily means that simple force balances in which the average stress in the scale is balanced by a uniformly varying stress in the metal no longer apply. While this assumption is a very useful one in analyzing the stresses in samples with flat scales, it

does not apply when wrinkling occurs even if the metal remains elastic. Second, if the local stresses in the metal exceed its yield stress, then it can be expected that the metal will deform plastically or, alternatively, if the temperature is sufficiently high, deform by creep. Either way, the strain energy in the scale will be relaxed but with concomitant irreversibility on thermal cycling and, hence, mechanical fatigue. The effect of plasticity when the local stress exceeds the yield stress has been discussed in some detail by Evans *et al.*⁹ based on finite-element computations of a slightly different geometry, namely, one in which two solid blocks are joined by a sinusoidal interface. Similar conclusions have also been reached based on finite-element simulations of the stress distributions around corners.¹⁰

Last, although the calculations presented here are couched in terms of strains created as a result of thermal-expansion mismatch, they are equally applicable to growth strains or, indeed, any combination of other strains associated with wrinkling. Wrinkling is a means of relaxing-strain energy but there are, of course, other mechanisms by which strain energy can be relaxed. Its occurrence during oxidation appears to depend on a variety of parameters including how rough the initial surface is and the presence of impurities. In addition, certain elements appear to prevent it from occurring, for instance, yttrium in the base alloy, whereas others, such as calcium, can cause it to occur on alloys in which it does not usually occur.¹¹ These parameters clearly affect the nucleation and kinetics of wrinkling rather than the reduction in elastic-strain energy caused by wrinkling that is discussed in this work.

ACKNOWLEDGMENTS

We are indebted to Drs. V. Tolpygo and Jun He for discussions during the course of this work and allowing us to use their results. We are also grateful to Dr. V. Srikant for performing the X-ray analysis that have been used in these computations. The work was supported by the Office of Naval Research under grant NOOO14-97-1-0190.

APPENDIX. ANALYTICAL SOLUTIONS FOR THE STRESS AT THE INTERFACE OF A COATING ATTACHED TO A CYLINDRICAL/SPHERICAL SYMMETRIC SUBSTRATE

In idealizing the wrinkle geometry the regions in the vicinity of the crests and the troughs can be represented by a thin coating attached to either a sphere or a cylinder of radius, R (Fig. A1). With such an idealization, the coating is a cylindrical ring or spherical shell and the interface

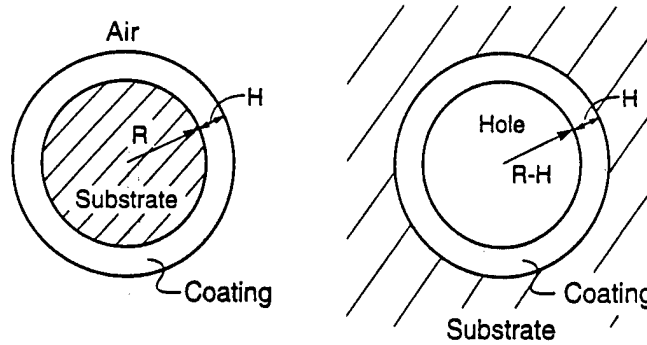


Fig. A1.

stresses can be determined analytically from the general stress solutions and the generalized Hooke's law by imposing the appropriate boundary conditions. The vicinity of the crest of the wrinkled coating corresponds to the substrate being on the inside and covered by the coating, whereas the vicinity of the trough corresponds to the substrate covering the coating. The general procedures to obtain the stress solutions are outlined below.

For an isotropic homogeneous elastic material, the generalized Hooke's law can be written as:

$$\epsilon_i = \frac{1}{E} [\sigma_i - \nu(\sigma_j + \sigma_k)] + \alpha \Delta T \quad (\text{A1})$$

where index i, j , and k denotes the three perpendicular directions, ϵ is the strain, σ is the stress, α is the thermal-expansion coefficient, and ΔT is the temperature change.

Spherically Symmetric Case

The general stress solution may be written, using a spherical coordinate system of (r, θ, ϕ) , as¹²

$$\sigma_r = \frac{c_1}{r^3} + c_2 \quad (\text{A2a})$$

$$\sigma_\theta = \sigma_\phi = -\frac{c_1}{2r^3} + c_2, \quad (\text{A2b})$$

where c_1 and c_2 are constants to be determined from the application of the boundary conditions. Notice that the stress takes the same form in both the coating and the substrate but with differing coefficients, so that four constants need be determined. For clarification, the physical properties in the

coating and the substrate are distinguished by superscript^O and ^A. H is the coating thickness and R is the radius of the coating-substrate interface. If the substrate is surrounded by the coating, the boundary conditions are:

$$\text{stresses are finite when } r = 0 \quad (\text{A3a})$$

$$\sigma_r^O = 0, \quad \text{when } r = R + H \quad (\text{A3b})$$

$$\sigma_r^O = \sigma_r^A, \quad \text{when } r = R \quad (\text{A3c})$$

$$\varepsilon_\varphi^O = \varepsilon_\varphi^A, \quad \text{when } r = R \quad (\text{A3d})$$

On determination of the constants, the normal stress at the interface can be written as,

$$\sigma_r(r = R) = - \frac{E^O(\alpha^A + \alpha^O)\Delta T \left[\left(\frac{R+H}{R} \right)^3 - 1 \right]}{1 - 2\nu^O + \frac{1 + \nu^O}{2} \left(\frac{R+H}{R} \right)^3 + (1 - 2\nu^A) \frac{E^O}{E^A} \left[\left(\frac{R+H}{R} \right)^3 - 1 \right]} \quad (\text{A4})$$

Because the thermal-expansion coefficient in the substrate, assumed to be a metal, is larger than that in the coating, assumed to be the oxide, the interface normal stress is tensile when the structure is cooled from a high to a low temperature.

In the other topology, corresponding to the substrate being on the outside, the corresponding boundary conditions are:

$$\text{stresses vanish when } r \rightarrow \infty \quad (\text{A5a})$$

$$\sigma_r^O = 0, \quad \text{when } r = R - H \quad (\text{A5b})$$

$$\sigma_r^O = \sigma_r^A, \quad \text{when } r = R \quad (\text{A5c})$$

$$\varepsilon_\varphi^O = \varepsilon_\varphi^A, \quad \text{when } r = R \quad (\text{A5d})$$

Combining with Eqs. (A1-A2), the normal stress at the interface can be written as,

$$\sigma_r(r = R) = \frac{E^O(\alpha^A - \alpha^O)\Delta T \left[1 - \left(\frac{R-H}{R} \right)^3 \right]}{1 - 2\nu^O + \frac{1 + \nu^O}{2} \left(\frac{R-H}{R} \right)^3 + \frac{E^O}{E^A} \left(\frac{1 + \nu^A}{2} \right) \left[1 - \left(\frac{R-H}{R} \right)^3 \right]} \quad (\text{A6})$$

As expected, in this case, the normal stress is compressive when the temperature change ΔT is negative.

Cylindrically Symmetric Case

The general solution for the in-plane stress, σ_r , and σ_ϕ , for symmetric closed ring in cylindrical coordinates (r, ϕ, z) , can be written as,

$$\sigma_r = \frac{c_3}{r^2} + c_4 \quad (\text{A7a})$$

$$\sigma_\phi = -\frac{c_3}{r^2} + c_4 \quad (\text{A7b})$$

where c_3 and c_4 are constants. As in the spherical case, the stress solution in the substrate takes the same form as it does in the coating and so there are four constants to be determined in order to evaluate the in-plane stresses. With the requirement that the plane remains plane during the cooling, the strain in the z -direction is constrained to be a constant in both the coating and the substrate. In particular, when the substrate is much larger than the coating, the strain in the z -direction is equal to the thermal strain of the substrate, i.e.,

$$\begin{aligned} \epsilon_z^O = \epsilon_z^A = \alpha^A \Delta T &= \frac{1}{E^A} [\sigma_z^A - \nu(\sigma_r^A + \sigma_\phi^A)] + \alpha^A \Delta T \\ &= \frac{1}{E^O} [\sigma_z^O - \nu(\sigma_r^O + \sigma_\phi^O)] + \alpha^O \Delta T \end{aligned} \quad (\text{A8})$$

This condition, combined with the boundary conditions listed in Eq. (A3), gives the tensile normal stress at the interface,

$$\sigma_r(r=R) = -\frac{E^O(\alpha^A - \alpha^O)\Delta T \left[\left(\frac{R+H}{R} \right)^2 - 1 \right]}{1 - 2\nu^O + \left(\frac{R+H}{R} \right)^2 + \frac{E^O}{E^A} \left(\frac{1-\nu^A}{1+\nu^O} \right) \left[\left(\frac{R+H}{R} \right)^2 - 1 \right]} \quad (\text{A9})$$

Similarly, the compressive normal stress is solved by combining Eq. (A8) with Eq. (A4):

$$\sigma_r(r=R) = \frac{E^O(\alpha^A - \alpha^O)\Delta T \left[1 - \left(\frac{R-H}{R} \right)^2 \right]}{1 - 2\nu^O + \left(\frac{R-H}{R} \right)^2 + \frac{E^O}{E^A} \left(\frac{1+\nu^A}{1+\nu^O} \right) \left[1 - \left(\frac{R-H}{R} \right)^2 \right]} \quad (\text{A10})$$

Notice that in both the cylindrical and spherical symmetric cases, the compressive stress solutions obtained from the above analysis are limited to $R/H > 1$. Thus, the tensile stress solution of generalized plane-strain case is reversed and plotted in dotted line in Fig. 12 to compare with the compressive stress in the trough, when $R/H < 1$.

When R/H is large, the magnitudes of interface stress evaluated from equations (A9) and (A10) reduces to Eq. (7) in the body of the text, and the magnitude of the interface stress evaluated from Eqs. (A4) and (A6) are just twice as large as that evaluated from Eq. (7). This is in accordance with that assumed in the discussion.

REFERENCES

1. V. K. Tolpygo and H. J. Grabke, *Oxid. Met.* **41**, 343 (1994).
2. B. A. Pint, A. J. Garratt-Reed, and L. W. Hobbs, *Mater. High Temp.* **13**, 3 (1995).
3. F. H. Stott, G. C. Wood, and J. Stringer, *Oxid. Met.* **44**, 113 (1995).
4. D. R. Sigler, *Oxid. Met.* **40**, 555 (1993).
5. Z. Suo, *J. Mech. Phys. Solids* **43**, 829 (1995).
6. Q. Ma and D. R. Clarke, *J. Am. Ceram. Soc.* **76**, 1433 (1993).
7. D. M. Lipkin and D. R. Clarke, *Oxid. Met.* **45**, 267 (1996).
8. J. He, PhD thesis, University of California, Santa Barbara (1997).
9. A. G. Evans, M. Y. He and J. W. Hutchinson, *Acta Mater.*, (in press).
10. R. L. Williamson, J. K. Knight, and R. M. Cannon, *Proc. Electrochem. Soc.* **96-26**, 16 (1997).
11. V. Tolpygo and H. J. Grabke, *Scripta Mater.* **38**, 123 (1998).
12. S. P. Timoshenko and J. N. Goodier, *Theory of Elasticity*, 3rd edn. (McGraw-Hill Book Company, New York, 1970).



WRINKLING OF α -ALUMINA FILMS GROWN BY THERMAL OXIDATION—I. QUANTITATIVE STUDIES ON SINGLE CRYSTALS OF Fe–Cr–Al ALLOY

V. K. TOLPYGO and D. R. CLARKE†

Materials Department, College of Engineering, University of California, Santa Barbara,
CA 93106-5050, U.S.A.

(Received 2 February 1998; accepted 30 March 1998)

Abstract—Quantitative measurements of the wrinkling morphology of the alpha-alumina scales formed by thermal oxidation at 1000°C and its evolution with oxidation time have been made using atomic force microscopy. The wrinkling wavelength and amplitude, and from these the surface area of the scale, for (110), (100) and (111) oriented single crystals of Fe–Cr–Al alloy as a function of oxidation time are presented. The residual stress in the scales is determined using piezospectroscopy. Together these results provide the basis for determining the lateral strains associated with the growth of the oxide. Crystallographic orientation of the alloy surface has a pronounced effect on both the wrinkling morphology and stress in the scale during the first 20–30 h of oxidation. The presence of the reactive element, yttrium, suppresses wrinkling and restricts lateral growth but it does not decrease the stress in the oxide. © 1998 Acta Metallurgica Inc. Published by Elsevier Science Ltd. All rights reserved.

1. INTRODUCTION

During oxidation of many Fe–Cr–Al and Ni–Cr–Al high-temperature alloys, the aluminum oxide formed on the surface adopts a wrinkled or convoluted morphology [1]. This morphology, shown in Fig. 1(a), develops and changes with time during oxidation at high temperature and is not a result of cooling to room temperature. Observations of cross-sections reveal that the thickness of the oxide is more or less uniform demonstrating that wrinkling is not caused by oxide intrusions or variations of the oxide growth rate from place to place.

Although the mechanism of wrinkling is not completely understood, it is believed that wrinkles form when the oxide expands in the lateral direction parallel to the metal surface during oxidation [2]. This lateral growth, in contrast to “normal” growth at the outer or inner surface, may be a result of oxide formation within the existing layer [2,3], or may simply occur due to volumetric changes when the metal transforms into the oxide. In either case, because of the constraint from the underlying metal, a compressive growth stress develops in the oxide parallel to the interface and energy is stored as elastic strain energy. Wrinkling is a deformation mode by which elastic strain energy can be reduced [4]. Therefore it may serve as a relaxation process, concurrent with stress generation during oxidation, leading to a net decrease in the average stress in the oxide. Typically, the strains associated

with wrinkling are so large that the change in oxide morphology necessitates that it deforms by plastic flow.

Although the phenomenon of wrinkling has been widely recognized for many years, its geometrical evolution and the accompanying stress in the oxide have not been systematically studied. The only recently published experimental study by Hou *et al.* [5] deals with some aspects of the geometrical parameters of the alumina scale on Fe–Cr–Al alloys. As for the residual and growth stresses in the wrinkling scales, to the authors’ knowledge, no reliable results have been presented so far. The motivation for the present work is both to provide a detailed description of the morphological instability of oxide wrinkling on a common Fe–Cr–Al alloy and to relate the wrinkling evolution to the growth stress in the oxide. Both subjects are of general importance to a much wider range of alloys since wrinkled oxides invariably exhibit poor adherence during cyclic oxidation. While particular attention during the past decade has been given to the effects of interfacial chemistry on the oxide spalling resistance [6–8], the importance of oxide configuration has not been so thoroughly investigated. An essential point in this geometrical concept is that wrinkling, in effect, transforms the biaxial stress in a planar oxide to create a component of stress normal to the interface thereby providing a force to separate the oxide from the metal [9–11]. In contrast, if the oxide and oxide–metal interface are flat, no stresses act in the normal direction.

†To whom all correspondence should be addressed.

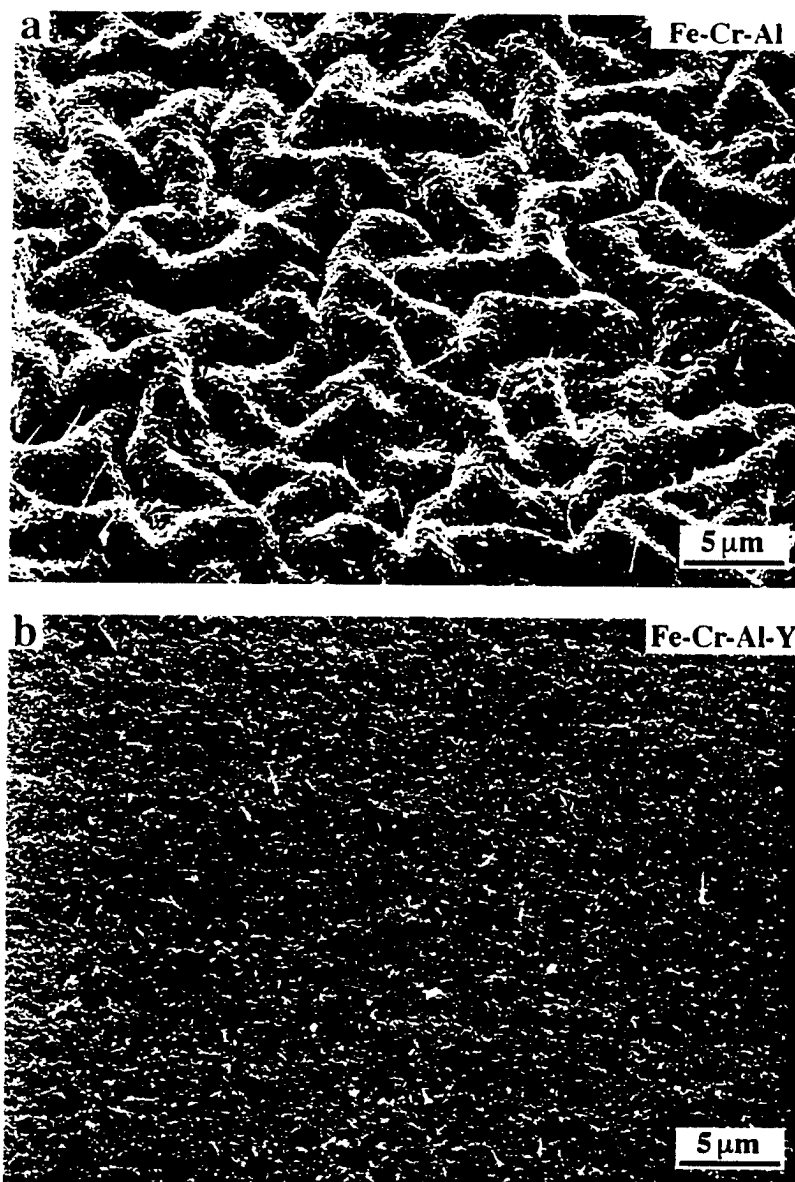


Fig. 1. Typical morphology of the wrinkled α -Al₂O₃ scale on the Fe-Cr-Al alloy (a) and flat α -Al₂O₃ scale on the Fe-Cr-Al-Y alloy (b) after oxidation at 1000°C for 100 h. Both alloys are single crystals with the surface polished parallel to the (111) b.c.c. plane.

It is well established that small additions of reactive elements such as Y, Ce, Zr to Fe-Cr-Al and Ni-Cr-Al alloys alter the morphology of the oxide leading to the formation of a flat and adherent alumina scale [1] [Fig. 1(b)]. Originally, it was supposed that the absence of wrinkles on the yttrium-containing alloys was due to the growth stresses in the oxide being smaller [2]. However, recent measurements have shown that the compressive growth stress in the oxide on the Fe-Cr-Al-Y alloy may be as high as 1 GPa at the oxidation temperature [12]. Yet, the scale remains flat during oxidation and, moreover, can withstand an additional compression of the order of 3–5 GPa on cooling caused by thermal expansion mismatch between the oxide and the metal. Another expla-

nation of the reactive element effect is that yttrium prevents sulfur segregation at the oxide-metal interface [6–8] and thereby increases the interfacial fracture resistance. There is indeed ample evidence from the literature that, if sulfur segregation is eliminated, then the oxides are much more adherent. At the same time, it seems remarkable that oxide wrinkling on the alloys with reactive elements is also suppressed, and consequently there are no forces acting to separate the oxide. Which of these two factors is of major importance and whether both are interrelated remains to be established.

The single-crystal Fe-Cr-Al alloy was chosen in order to study the dependence of wrinkling evolution on metal crystallographic orientation. Whilst the role of yttrium is not specifically addressed in

this work, the flat scale on the Fe–Cr–Al–Y alloy, and in particular the residual and growth stresses, provide an essential comparison to the wrinkling scale observed on the yttrium-free alloy. In the accompanying paper [13], which considers observations of oxide separation from the underlying alloy, its association with the evolution in wrinkling morphology and the separation sequences leading up to spalling failure are described.

2. EXPERIMENTAL

Two single-crystal alloys were studied: Fe–19.5%Cr–4.5%Al and Fe–21.7%Cr–5.42%Al–0.003%Y (wt%). Specimens about $8 \times 8 \times 0.5 \text{ mm}^3$ in size were cut parallel to either (110), (100) or (111) crystallographic planes of a b.c.c. lattice, mechanically polished to a $0.1 \mu\text{m}$ finish, and cleaned in acetone. Oxidation experiments were carried out in static air at 1000°C for times ranging from 0.1 to 100 h. The heating and cooling rate was about $500^\circ\text{C}/\text{min}$. Preliminary experiments have shown that both materials are pure alumina formers, i.e. the only oxide phase growing during oxidation at 1000°C is $\alpha\text{-Al}_2\text{O}_3$. Previous studies have also confirmed that 30 ppm Y in the alloy is enough to completely prevent alumina wrinkling and provide a flat scale [14]. Oxide morphology was examined using SEM. The thickness of the scale was estimated from thermogravimetric results of the mass change during oxidation assuming that the scale was fully dense $\alpha\text{-Al}_2\text{O}_3$.

The wrinkling morphology on the Fe–Cr–Al alloy was quantified using atomic force microscopy (AFM). Several images of the oxide surface, $40 \times 40 \mu\text{m}^2$ in size, were scanned on each specimen. Since the oxide wrinkles exhibit some periodicity, analysis of the AFM scans provides quantitative characteristics, such as average wavelength and amplitude of the oxide undulations. The characteristic wavelength was determined from the power spectral density plot for the whole area of each AFM image. The amplitude was characterized by the root-mean-square roughness parameter R_q calculated as the standard deviation of the height of each point on the surface relative to the average value. In these measurements the AFM images were digitally processed in such a way that the roughness caused by the shape of individual oxide grains was filtered out.

It should be noted that geometrical parameters, measured in this work, refer only to the outer oxide surface. As shown below, the oxide–metal interface on the Fe–Cr–Al alloy does not perfectly match the outer surface. This means that the “actual” configuration should include parameters of both the outer and inner surfaces, i.e. correspond to some average mid-section of the oxide. However, the strong adhesion of the oxide on many specimens, especially after short oxidation times, precluded ex-

posure of sufficiently large areas of the metal surface for comparison. Therefore a detailed AFM study of the interfacial configuration and its evolution has not been performed, and so only the parameters of the outer surface are used for the analysis. Nevertheless, when spalling of the scale exposed the alloy surface, these areas were analyzed and the results presented below.

The residual stress in the $\alpha\text{-Al}_2\text{O}_3$ was measured at room temperature using the photo-stimulated luminescence piezospectroscopy technique [15,16]. The stress is obtained from the frequency shift, $\Delta\nu$, of the characteristic R-lines of the Cr^{3+} luminescence relative to the stress-free alumina according to Refs [16,17]

$$\Delta\nu = \frac{1}{3} \Pi_{ii} \sigma_{ij} \quad (1)$$

where σ_{ij} are the hydrostatic components of the stress tensor and Π_{ii} are the components of the piezospectroscopic tensor ($\Pi_{ii} = 7.60 \text{ cm}^{-1}/\text{GPa}$ for polycrystalline alpha-alumina [17]). The stress-free frequency was measured on spalled or specially separated pieces of oxide after different exposures. For a flat scale, the stress is assumed to be biaxial, such that $\sigma_{xx} = \sigma_{yy} = \sigma$ and $\sigma_{zz} = 0$ (x and y are in-plane axes, and z is normal to the surface). Therefore, the stress can be directly determined from the frequency shift:

$$\Delta\nu = \frac{2}{3} \Pi_{ii} \sigma \quad (2)$$

or $\sigma \approx 0.197 \Delta\nu$, where σ is expressed in GPa and $\Delta\nu$ is measured in cm^{-1} . When the scale wrinkles, however, equation (2) is generally not valid because the component σ_{zz} normal to the specimen surface is no longer zero. Moreover, in each given place, its value depends on the local configuration of the oxide and oxide–metal interface. In turn, the in-plane components σ_{xx} and σ_{yy} should vary from place to place over the surface depending on the geometry of the oxide. As a result, the stress in a wrinkled scale is not readily obtained from the piezospectroscopic measurements and, generally, only the frequency shifts can be directly compared. In those cases below where the wrinkling configuration is quantified, the results of finite element analysis [11] will be used to transform the frequency shift into stress.

On the Fe–Cr–Al–Y alloy, the stress distribution over the specimen surface was very uniform, whereas on the Fe–Cr–Al alloy, the frequency shift measured with a small probe size demonstrated a large variability because of the oxide wrinkling. For this reason measurements were performed using an optimal probe size of about $4\text{--}5 \mu\text{m}$, which was found to be large enough to minimize variations of the frequency shift from place to place. Typically, 15–25 individual measurements were made from

different places on each specimen in order to determine an average shift.

A comparison of the luminescence frequency from the spalled oxide with that of a pure (and stress-free) sapphire provides a means to evaluate the chromium concentration in the scale. Increasing the chromium concentration in alpha-alumina gives a systematic frequency shift of the luminescence R-lines. The concentration-related shift (that is opposite to the compressive stress shift) is known to be [15]

$$\Delta\nu^* = 0.99 \cdot c_{Cr} \quad (3)$$

where chromium concentration, c_{Cr} is expressed in wt%.

3. RESULTS

A typical example of the wrinkling morphology of the scale is presented in Fig. 2. These SEM micrographs show the oxide surface and alloy surface exposed by spalling of the scale after cooling to room temperature. A closer examination shows [Fig. 2(b)] that the alloy surface is completely covered with imprints of alumina grains indicating that it remains in contact with the oxide during the scale

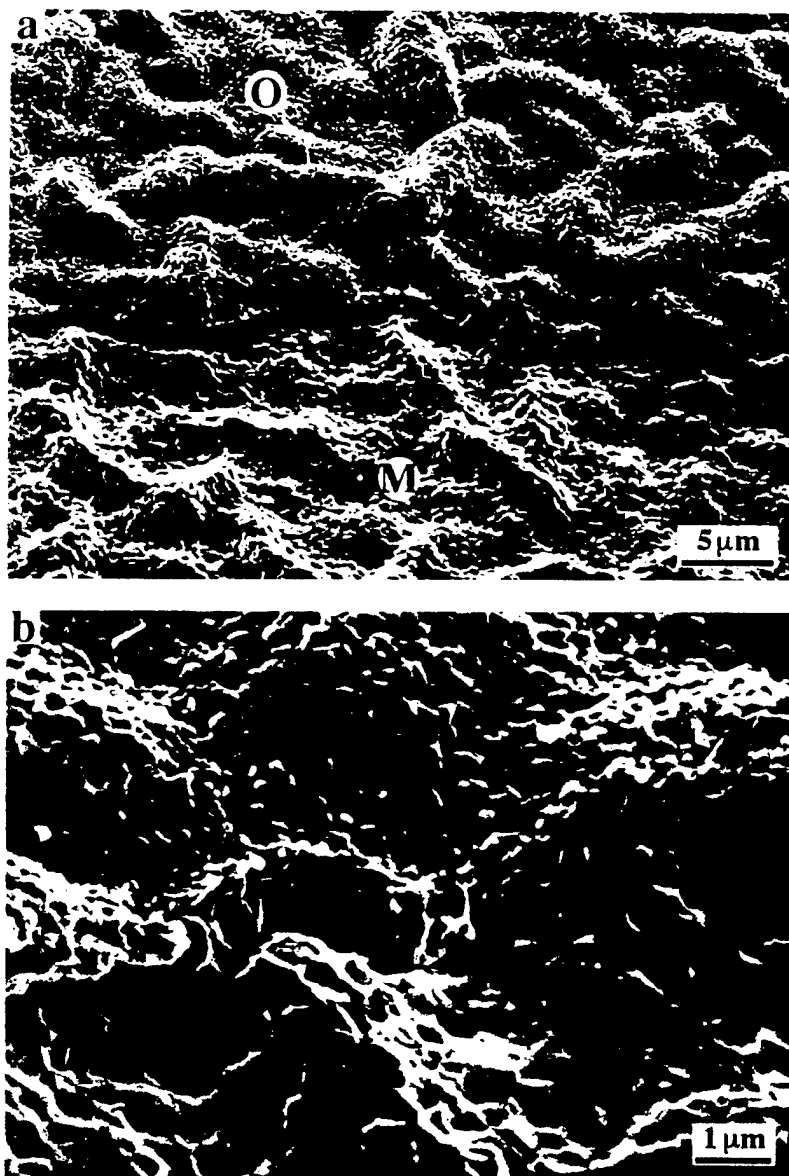


Fig. 2. SEM micrographs of the scale and metal surface on the (110) Fe-Cr-Al alloy after oxidation at 1000°C for 70 h: (a) general view showing that the metal surface, exposed after oxide spalling, exhibits wrinkling similar to the outer oxide surface (O—oxide, M—metal); (b) enlarged view of the scale cross-section and imprints of alumina grains on the metal surface.

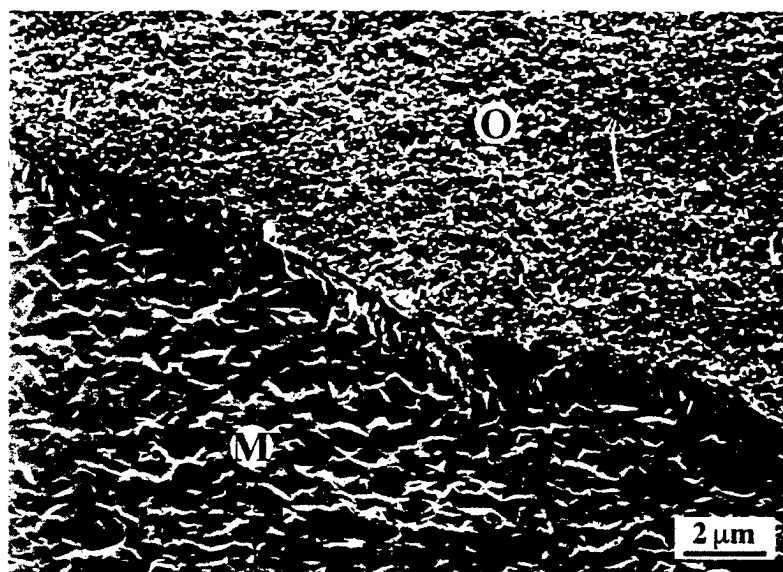


Fig. 3. Structure of the scale and scale-metal interface on the (110) Fe-Cr-Al-Y alloy after oxidation at 1000°C for 100 h.

growth and deforms together with the wrinkling scale. As a result, the configuration of the oxide-metal interface is generally similar to that of the outer scale surface. Various studies have shown that oxide wrinkles are associated, although not exclusively, with interfacial cavities or voids which are believed to be a result of scale decohesion and buckling during oxidation [1]. In contrast, our observations, as well as other results [5], suggest that, on a flat alloy surface in the absence of polishing scratches or contaminants, voids are very rare and the scale grows in contact with the alloy. For comparison, Fig. 3 demonstrates the morphology of the oxide and oxide-metal interface on the yttrium-containing alloy. Both the outer surface and oxide-metal interface remain nearly flat through the whole period studied. The following sections present results of a detailed examination of the wrinkled and flat scales formed on these two alloys.

3.1. Fe-Cr-Al alloy

All measurements on the Fe-Cr-Al alloy were performed after isothermal oxidation. Results of AFM analysis, as well as SEM observations, reveal that the scales formed during the initial oxidation stages exhibit substantially different configurations depending on the crystallographic orientation of the alloy surface. Two AFM images of the oxide surface and two SEM micrographs of the same specimens (Fig. 4) demonstrate a distinct difference in the extent of wrinkling between (110) and (111) orientations of the initial alloy surface after oxidation for 3 h. Oxide undulations are more pronounced on the (111) Fe-Cr-Al and show typical patterns of ridges extended in all directions [Fig. 4(b)], while on the (110) Fe-Cr-Al, they have

rather axisymmetric shape [Fig. 4(a)]. After prolonged oxidation, wrinkles increase their size, but the difference between metal orientations gradually disappears.

Figure 5 shows the time evolution of the wrinkling parameters. The wavelength, $2L$, represents the average distance between peaks or valleys of the oxide surface. For all metal orientations, the wavelength of oxide wrinkles increases with time in a similar manner [Fig. 5(a)]. Fitting the data by a power law gives comparable curves with time exponents between 1/3 and 1/4. The standard deviation of the data becomes quite large after prolonged oxidation because only a few wavelengths are located within the measured $40 \times 40 \mu\text{m}^2$ areas (a limitation imposed by the AFM being used). Interestingly, extrapolating the data to time $t = 0$ gives $2L_0 = 1.0\text{--}1.5 \mu\text{m}$. This suggests that wrinkling starts with some initial wavelength which appears to be independent of the substrate orientation. Its value is also much larger than the oxide grain size at the beginning of oxidation (estimated to be less than 50 nm). Solid points in Fig. 5(a) show the wavelength of the metal surface measured in places where the scale spalled off after cooling to room temperature. Although the number of data is small, it appears that both the outer and inner oxide surfaces have similar wavelengths. This is also confirmed by direct SEM observations (Fig. 2).

The time dependence of the roughness parameter R_q [Fig. 5(b)] also reveals similar behavior for all orientations of the metal substrate: a fast initial growth of oxide undulations is followed by relatively small changes after longer times. However, a clear difference in wrinkling amplitude is detected during the early stages of oxidation. While all start-

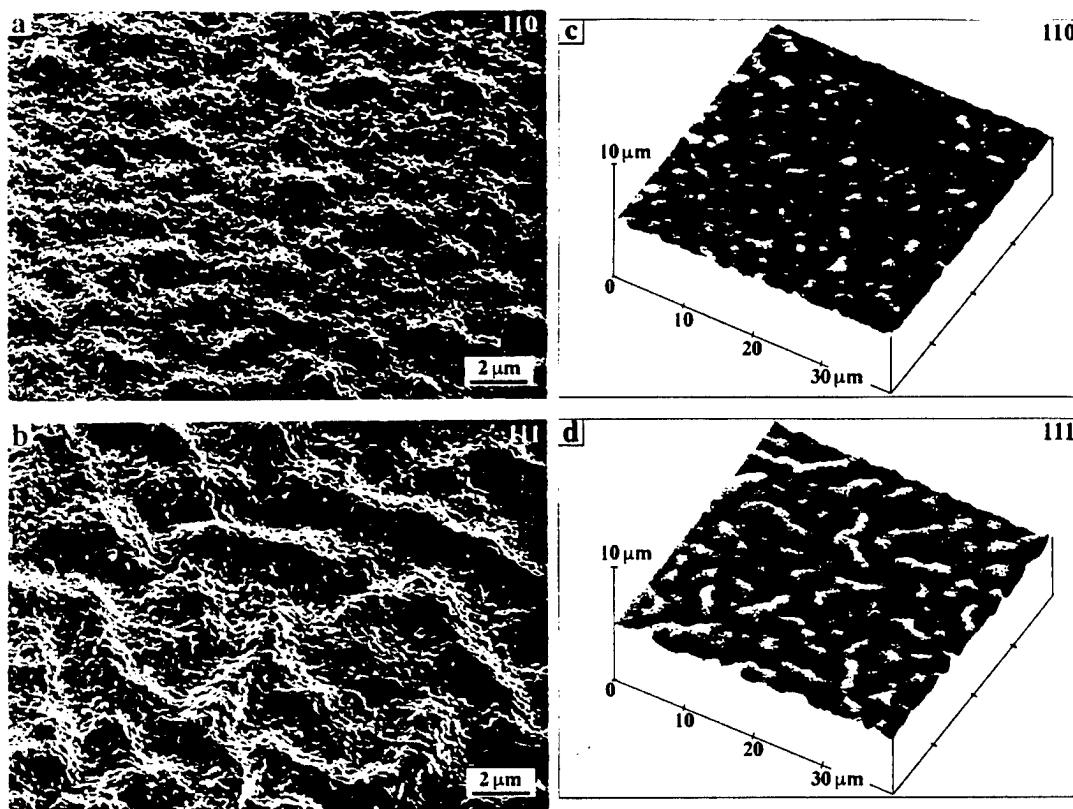


Fig. 4. SEM micrographs (a); (b) and AFM scans (c), (d) of the oxide surface on the Fe-Cr-Al alloy after oxidation at 1000°C for 3 h. The alloy with (110) initial surface orientation produces axisymmetrical wrinkles (a), (c), while the same alloy with (111) orientation gives elongated ridges (b), (d).

ing material surfaces had approximately the same roughness ($R_q = 10$ nm), after a short oxidation time the amplitude is clearly larger on the (111) surface, smaller on the (100), and smallest on the (110) surface. After about 30 h all amplitudes are approximately equal, and after longer oxidation times the amplitude is even somewhat smaller on the (111) orientation. Measurements made after 250 h, although not presented here, demonstrate only a slight additional increase of R_q up to 0.5–0.6 μm and support the observation that the wrinkling amplitude, following an initial fast growth, then increases slowly with time.

A few data points in Fig. 5(b) characterize the roughness of the oxide-metal interface (solid points). Unlike the wavelength, which was quite similar for both the metal and oxide surfaces [Fig. 5(a)], the roughness of the metal surface is considerably smaller than that of the outer oxide surface. This result is illustrated in Fig. 6 by two AFM images of the same (110) specimen oxidized for 30 h: the oxide surface looks more wrinkled due to a larger amplitude. As the scale was in contact with the metal during oxidation and no interfacial cavities were formed, this necessarily means that the oxide layer is generally thicker near the peaks and thinner at the valleys of the interface.

An increase of the oxide surface area taken from the AFM roughness analysis is presented in Fig. 5(c). These results show a fast initial enlargement of the surface area as a result of wrinkling and no further increase after about 25–30 h.

The alumina scales formed on all the specimens after isothermal oxidation were analyzed using optical piezospectroscopy. The frequency shift, $\Delta\nu$, relative to the stress-free state, is shown in Fig. 7 for all three orientations of the Fe-Cr-Al alloy. The largest frequency shift, corresponding to the highest residual room-temperature stress in the scale, is observed after short oxidation (less than 1 h). With increasing time, the shift decreases for all orientations suggesting that the growth stress in relatively thick scales is smaller than in thin scales at the beginning of oxidation. Among the three orientations, the highest shift is detected on the (110) and the smallest on the (111) specimens. After prolonged oxidation (100 h), the frequency shift does not vary much between the different metal orientations although the data show a relatively large scatter on a given specimen.

The stress axis included in Fig. 7 represents nominal values calculated assuming biaxial compression of the oxide [equation (2)]. In general, however, the relationship between residual stress and frequency

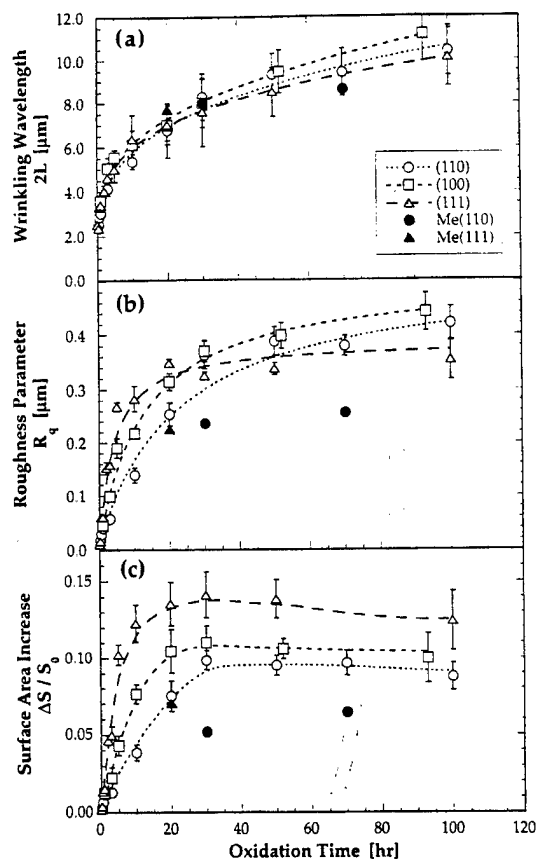


Fig. 5. Geometrical parameters of the scale wrinkling as a function of oxidation time at 1000°C for the three orientations of the Fe-Cr-Al alloy: (a) average wavelength $2L$; (b) surface roughness parameter R_q ; (c) surface area ratio $\Delta S/S_0 = (S - S_0)/S_0$ where S is the actual three-dimensional surface area and S_0 is the two-dimensional projected area. Open symbols—oxide surface; solid symbols—metal surface.

shift is rather complex [11], and the biaxial approximation is not valid. Nevertheless, there is a direct correspondence between frequency shift and elastic strain energy, so a reduction in frequency shift can be directly interpreted as a reduction in the average stress in the scale and vice versa [11]. The results in Fig. 7 indicate a substantial difference in room-temperature residual stress between three orientations after short oxidation exposures. Since the thermal mismatch stress should not depend strongly on the metal orientation, this difference is largely due to the different values of the growth stresses. An attempt to quantify the growth stress in the wrinkled oxide using the piezospectroscopic frequency shift and AFM results is given in the Discussion (Section 4).

Taken together with the geometrical parameters, the data in Fig. 7 reveal a striking correlation between the average stress and the extent of oxide wrinkling: a higher growth stress on the (110) orientation corresponds to a less wrinkled scale.

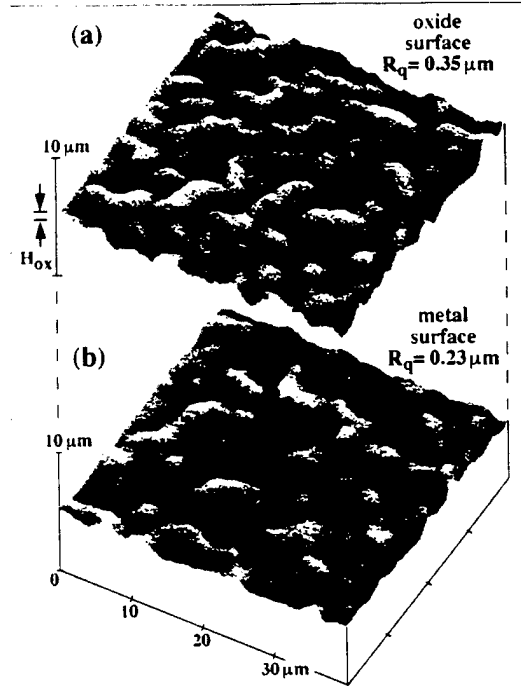


Fig. 6. Two AFM images of the oxide surface (a) and metal surface (b) on the same (110) Fe-Cr-Al alloy after oxidation at 1000°C for 30 h. The roughness parameter R_q equals 0.35 μm (a) and 0.23 μm (b). Estimated oxide thickness H_{ox} is indicated.

Conversely, on the (111) orientation, the scale is more prone to wrinkling while the growth stress is lower. After longer oxidation the influence of substrate orientation becomes insignificant.

Importantly, the orientation dependence of wrinkling parameters and residual stress is not caused by the difference between growth rates of alumina scale. On the contrary, all three orientations of the Fe-Cr-Al alloy show almost identical parabolic oxidation kinetics (Fig. 8). Chromium concentration is also very much the same in scales formed on all orientations of the Fe-Cr-Al alloy (Fig. 9), and therefore different behavior of the scales cannot be explained by an effect of chromium on the alumina creep rate. The concentration is surprisingly high in very thin scales after short oxidation times. This may be due to the formation of significant amounts of chromia or spinel phases at the nucleation stage. However, even after the shortest time examined (0.1 h), the scale is entirely composed of $\alpha\text{-Al}_2\text{O}_3$, i.e. any chromium-containing oxides initially formed are already dissolved in the alumina. Subsequently, the concentration gradually decreases probably as a result of less chromium entering the growing scale and also due to chromium evaporation from the scale during oxidation. Although we have not measured the iron concentration, cursory SIMS and RBS results indicate a general tendency for the concentration of Fe ions to be similar to that shown in Fig. 9 for Cr ions. The

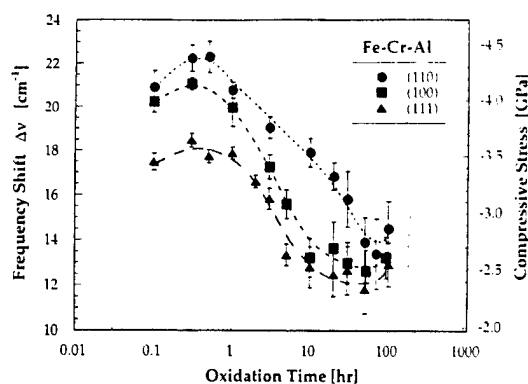


Fig. 7. Frequency shift of the characteristic R_2 -line of α - Al_2O_3 scales on different alloy orientations as a function of oxidation time at 1000°C. The second y-axis shows the calculated residual stress in the scale assuming it to be under biaxial compression.

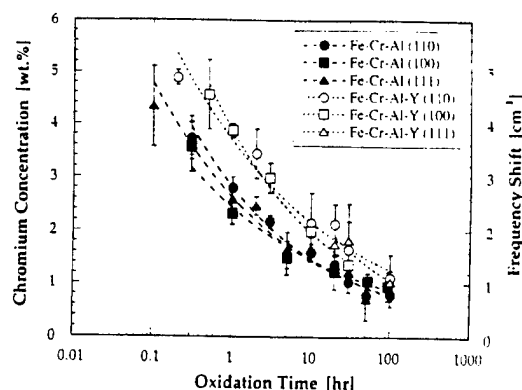


Fig. 9. Chromium concentration in the α - Al_2O_3 scales formed on the Fe-Cr-Al (solid symbols) and Fe-Cr-Al-Y (open symbols) alloys. The concentration was determined from the luminescence frequency shift measured on the spalled oxide relative to a stress-free sapphire.

data for the Fe-Cr-Al-Y alloy, included in Fig. 9 for comparison, will be discussed in Section 3.2.

3.2. Fe-Cr-Al-Y alloy

Unlike the Fe-Cr-Al alloy, measurements on single-crystalline specimens of the Fe-Cr-Al-Y alloy were performed mainly in the course of cyclic oxidation. Each specimen was repeatedly oxidized for different times, examined at room temperature and oxidized again with a cumulative exposure of 100 h. A few specimens were isothermally oxidized in order to check whether the time evolution of the residual stress in the oxide was affected by intermediate cooling and heating during cyclic oxidation. No detailed investigation of the oxidation kinetics has been performed on the Fe-Cr-Al-Y alloy; however, the microscopic observations confirm that the oxide thickness is comparable with that on the Fe-Cr-Al alloy (Figs 2 and 3).

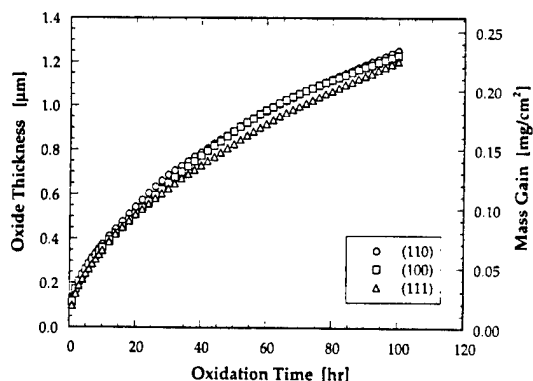


Fig. 8. Kinetics of isothermal oxidation of the Fe-Cr-Al alloy at 1000°C. Experimental data were obtained as a mass gain per unit surface area and then transformed into oxide thickness.

Since the alumina scale on the yttrium-containing alloy is almost perfectly flat, no AFM results are presented for this alloy. The time dependence of the residual stress in the scale together with the frequency shift of the R_2 -line are shown in Fig. 10. The flat configuration of the oxide and oxide-metal interface implies that the scale is under a biaxial compression, so a simple relation [equation (2)] between the frequency shift and residual stress can be used. Specimens of all three orientations exhibit identical residual stress after oxidation for 0.1 h. The same is observed after 100 h. In between, the stress is somewhat higher on the (110) orientation than on the other specimens. The data points showing residual stress after isothermal oxidation fit well into the curves for cyclic experiments suggesting that intermediate cooling does not affect time evolution of residual stress, i.e. does not lead to stress relaxation.

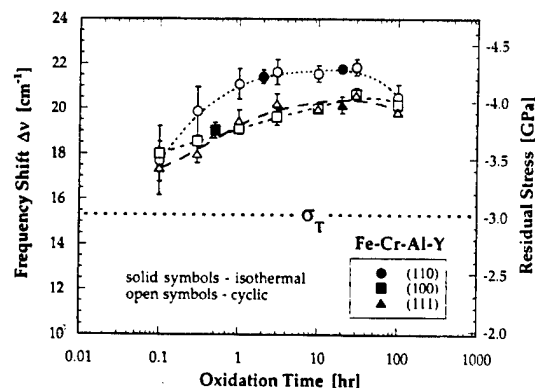


Fig. 10. Frequency shift and corresponding residual compressive stress in the scales formed on the Fe-Cr-Al-Y alloy during oxidation at 1000°C. Estimated value of the thermal mismatch stress, σ_T , is indicated.

In general, the room-temperature residual stress is much higher than expected from the thermal mismatch alone. This gives a clear indication that the oxide is under compression during oxidation. Similar to the Fe-Cr-Al alloy, the variation of the residual stress with time means that the growth stress also changes. At this point, we can qualitatively estimate that the growth stress in the scale on the Fe-Cr-Al-Y alloy gradually increases and reaches values of the order of 0.5–1.0 GPa during oxidation. A slight decrease between 30 and 100 h may be due to some plastic relaxation, presumably by metal creep, during oxidation. This process, as recently demonstrated on a polycrystalline Fe-Cr-Al-Y alloy oxidized at 1100–1300°C [12], leads to measurable elongation of the specimens. For 0.4 mm thick rectangular specimens used in this work, compressive stress of about 1 GPa in the 1 μ m thick oxide on both sides of the plate must be balanced by a biaxial tension of 5 MPa in the metal. This stress is sufficient for some metal creep to occur at 1000°C, thus leading to a reduction of the stress in the scale during oxidation. This relaxation, however, has not been monitored in the present work, because the creep strain was too small to measure. Indeed, if caused exclusively by metal elongation, the reduction of oxide stress by 0.1–0.3 GPa between 30 and 100 h (Fig. 10) would correspond to the metal plastic strain of about 2×10^{-4} – 6×10^{-4} , which is below our detection limits (about 10^{-3} for a 7–8 mm specimen). Thus, although the possibility of stress relaxation by metal creep during oxidation is clear, no measurements of this are presented. As for the plastic stress relaxation after cooling, the same force balance arguments show that the tensile stress in the metal at room temperature does not exceed 20–25 MPa, i.e. cannot produce any plastic deformation of the specimens. Further analysis and comparison with the Fe-Cr-Al alloy are presented in Section 4.

The chromium concentration in alumina on the Fe-Cr-Al-Y alloy, determined from the concentration-related frequency shifts [equation (3)], is shown in Fig. 9. A decrease of the chromium content with time is very similar to that on the Fe-Cr-Al alloy although the concentration is slightly higher on the yttrium-containing alloy. Nevertheless, it may be concluded that the different behavior of the two alloys is not related to differences in the chromium content in the scale.

4. ANALYSIS AND DISCUSSION

The results described in the previous section indicate the presence of substantial growth stresses in oxide formed on both the Fe-Cr-Al and Fe-Cr-Al-Y alloys. At the same time, the behavior of the scales is very different. On the yttrium-containing alloy, the growth stress gradually increases with time, but the oxide remains flat. In contrast, on the

Fe-Cr-Al alloy, the growth stress generally decreases with time and the scale plastically deforms producing wrinkles. In addition, both the growth stress and wrinkling evolution depend on the crystallographic orientation of the metal.

As the formation of the oxide wrinkles occurs at high temperature, it is essential to compare the growth stresses in different scales and determine the growth stress variation with time. To do this, the thermal mismatch contribution must be subtracted from the residual room-temperature stress. For a flat oxide layer formed on the Fe-Cr-Al-Y alloy, the calculation of the thermal stress and growth stress is straightforward. If the scale is much thinner than the metal and no plastic relaxation occurs during cooling, which is apparently the case in the present experiments, the thermally induced stress, σ_T , is given by the following approximate expression:

$$\sigma_T = \frac{(x_{ox} - x_m)\Delta T \cdot E_{ox}}{1 - \nu_{ox}} \quad (4)$$

where the metal and oxide thermal expansion coefficients are, respectively, $x_m = 14.0 \times 10^{-6}/^\circ\text{C}$ and $x_{ox} = 8.2 \times 10^{-6}/^\circ\text{C}$ [18], ΔT is the temperature change ($\Delta T = 975^\circ\text{C}$), the oxide elastic modulus is taken to be $E_{ox} = 400$ GPa, and Poisson ratio $\nu_{ox} = 0.25$. For the Fe-Cr-Al-Y alloy, the thermal mismatch stress σ_T is indicated in Fig. 10. In turn, the growth stress in the scale, σ_G , can be determined from

$$\sigma = \sigma_T + \frac{E_{ox}}{E_{ox}^T} \cdot \sigma_G \quad (5)$$

where σ is the residual room temperature stress in the scale and $E_{ox}^T = 350$ GPa is the oxide Young's modulus at 1000°C [18]. Note that the compression is purely biaxial for the scales formed on the Fe-Cr-Al-Y alloy.

For a wrinkled scale, however, even the thermal mismatch stress, not to mention the growth stress, varies with position across the scale and depends on geometrical parameters of the oxide. As a result, all the stress components σ_{ij} are expected to change between peaks and valleys of the oxide layer. The mechanical aspects of such a complex situation were examined recently using finite element analysis [11], and the results of that study are applied in the following paragraphs. In particular, the dependence of the frequency shift on the oxide wavelength $2L$, amplitude A , and thickness H will be used. In the numerical analysis, the frequency shift was calculated for different geometrical parameters of the oxide subject to a known elastic thermal mismatch strain. In this work, a reverse problem is posed: the parameters L , A , H and the frequency shifts are experimentally determined whereas the stress (or elastic strain) is the unknown.

If the scale configuration exhibits a symmetry relative to some mid-plane, it is reasonable to assume that the average value of the normal component, σ_{zz} , over one wavelength, is essentially zero. The in-plane components, σ_{xx} and σ_{yy} , can be taken equal by symmetry. The shear stresses do not contribute significantly to the frequency shift [17]. All these assumptions simplify the comparison of the scales of different configurations. Once the wrinkling parameters are known, each particular geometry can be transformed into a flat oxide layer subject to the same (macroscopic) elastic strains as the wrinkled scale. The frequency shift and stress that would be obtained from such an equivalent scale can be found using the results from Ref. [11]. By doing this for all experimental data, all oxide configurations can be adjusted to a quasi-biaxial compression and hence can be compared with each other.

For the purpose of comparison, we suppose that all scales formed on the Fe-Cr-Al alloy assume a sinusoidal shape where the wrinkling displacement with time is given by:

$$z(x,y,t) = A(t) \cdot \sin\left[\frac{\pi x}{L(t)}\right] \cdot \sin\left[\frac{\pi y}{L(t)}\right] \quad (6)$$

with the wavelength $2L(t)$ and amplitude $A(t)$ both changing with time. For this configuration, the wrinkling amplitude is determined by the oxide roughness parameter as $A(t) = 2R_q(t)$. From the experimental values of $2L$ [Fig. 5(a)], R_q [Fig. 5(b)], and oxide thickness H (Fig. 8), we can find the dimensionless geometrical parameters L/H and A/H used in numerical calculations [11] and determine the frequency shift ratio, $k = \Delta v_w / \Delta v_f$, corresponding to each particular combination of parameters. Here, Δv_w is the average frequency shift that is measured on a wrinkled scale under a certain set of elastic strains, and Δv_f is the shift that would be measured on the equivalent flat scale. The time dependence of the parameters L/H and A/H as well as the frequency shift ratio k are presented in Fig. 11. Clearly, $k \rightarrow 1$ at the beginning of oxidation when scale is almost flat, and $k < 1$ when wrinkling occurs. This gives an important conclusion: the shift measured on a wrinkled oxide is always smaller than on a flat oxide for the same mismatch strain.

The frequency shift ratio, k , can be applied to the experimental values in Fig. 7 in order to find the frequency shift corresponding to the scale which is now assumed to be flat. This shift is determined as

$$\Delta v_{eq} = \frac{1}{k} \cdot \Delta v_{exp} \quad (7)$$

where Δv_{exp} denotes experimental results (Fig. 7) and k is taken from Fig. 11(c) for each given time and metal orientation. Since the calculated equivalent

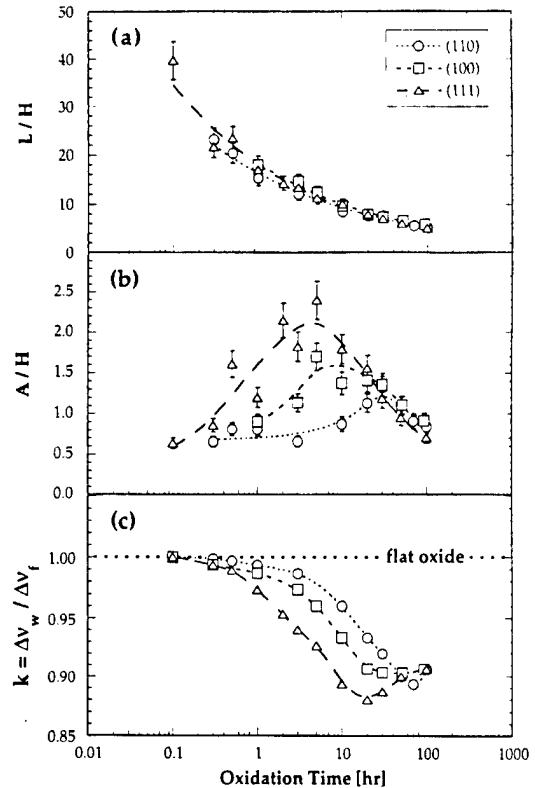


Fig. 11. Parameters used for the growth stress calculations in the wrinkling scales on the Fe-Cr-Al alloy: (a) experimental values of the wavelength-oxide thickness ratio, L/H ; (b) wrinkling amplitude-oxide thickness ratio, A/H ; (c) frequency shift ratio, $k = \Delta v_w / \Delta v_f$, taken from the finite element calculations in Ref. [11].

ent shift, Δv_{eq} , refers to a quasi-biaxial stress state, it can be transformed into compressive stress according to equation (2), and finally the oxide growth stress is obtained using equation (5). With the above correction [equation (7)] a comparison between wrinkled scales formed on different metal orientation is possible and, moreover, these data

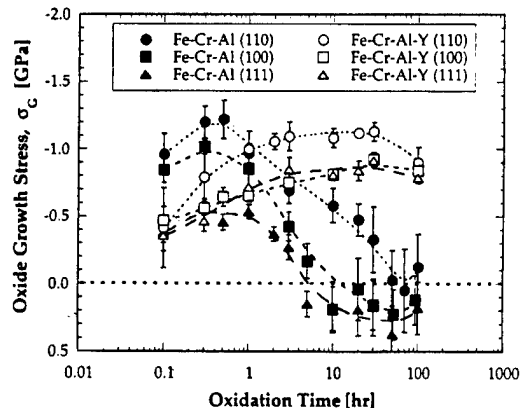


Fig. 12. Calculated values of the growth stress in the α - Al_2O_3 scales during oxidation at 1000°C of the Fe-Cr-Al (solid symbols) and Fe-Cr-Al-Y (open symbols) alloys.

can be compared with results for the Fe–Cr–Al–Y alloy.

Figure 12 shows the derived values of the oxide growth stress for all three orientations of both alloys. Two opposite tendencies are revealed. On the Fe–Cr–Al alloy, a rapid increase of the stress is followed by a gradual decline, essentially to zero after 20–30 h of oxidation. In contrast, on the yttrium-containing alloy the growth stress exhibits a continuous increase up to about 1 GPa and then a slight decrease after prolonged oxidation, which is believed to be a result of metal plastic relaxation, as indicated previously. Except for the first 2–3 h, the compressive stress in the oxide on the Fe–Cr–Al–Y alloy is substantially larger than that on the Fe–Cr–Al alloy. Several other features are worth mentioning. In all experiments, a growth stress of the order of 0.3–1.0 GPa is observed in very thin scales after only 6 min oxidation. The compression is notably higher on the (100) and, especially, (110) specimens of the Fe–Cr–Al alloy; it is precisely these orientations that produce less wrinkled scale initially. On the other hand, the (111) Fe–Cr–Al alloy and all orientations of the Fe–Cr–Al–Y alloy exhibit approximately equal growth stresses at the beginning of oxidation. Nevertheless the scale wrinkles within minutes on the former whereas it remains flat on the latter.

The growth stress for the Fe–Cr–Al alloy in Fig. 12 seems to decrease and become tensile (positive values) after longer times. This is, most probably, due to the fact that the scale configuration is not exactly symmetrical, so that the assumptions used for the numerical analysis are not entirely valid at long times. In particular, the frequency shift ratio [equation (7)] is only approximate. The second possibility is that partial stress relaxation in the metal occurs during cooling. To this point, the assumption has been made that the metal deforms elastically when temperature changes. For a flat oxide, this appears to be reasonable because of the small and uniform thermal stress in the metal, as mentioned above. The presence of wrinkles, however, should result in a non-uniform stress distribution in the subscale region of the metal with relatively high stresses in specific areas [11]. It is possible that plastic deformation of the metal occurs in these areas during cooling, thus leading to a decrease of the average residual stress in the oxide.

A comparison of the results for the Fe–Cr–Al and Fe–Cr–Al–Y alloys in Fig. 12 and the microscopic observations show that the existence of high growth stresses is not sufficient alone to cause wrinkling. Moreover, even on the same Fe–Cr–Al alloy, a higher growth stress on the (110) orientation does not lead to more extensive wrinkling. This suggests that the scale configuration is related to stress relaxation in the oxide but not specifically to the magnitude of the growth stress itself. If so,

the rate of alumina plastic relaxation becomes a critical factor in determining stress in the scale during its growth. Fast plastic deformation provides a decrease of the growth stress essentially to zero on the (111) and (100) Fe–Cr–Al after several hours. For some reason, it is retarded on the (110) orientation, thus the growth stress remains substantial for much longer times. Certainly, a higher stress in the oxide should lead to a higher creep rate, but other parameters such as alumina grain size or grain aspect ratio may well be dominating.

One of the consequences of the wrinkling and the fact that the underlying metal conforms to the oxide is that the surface orientation of the metal changes with time and becomes more and more randomized as wrinkling proceeds. As a result, the initial distinction between the crystallographic orientations of the specimens becomes smeared out when a thin scale is formed. It is therefore likely that the observed differences in residual stress and wrinkling morphology are determined at the nucleation stage of the scale formation. For instance, if a larger density of alumina nuclei form on the (111) orientated surface of the Fe–Cr–Al alloy, a smaller oxide grain size will result, thereby facilitating creep during oxidation. Conversely, a lower nucleation density would lead to a larger grain size and hence a more creep resistant oxide. Some preferential orientation of alumina grains relative to the metal's initial orientation is also possible [19], which would also affect plastic behavior of the scale and result in different creep rates.

It might be supposed, following the above arguments, that the absence of wrinkling on the Fe–Cr–Al–Y alloy denotes a very slow relaxation, and therefore the growth stress remains high during oxidation. This assumption looks even more reasonable as the creep rate of alumina has been shown to be significantly reduced by yttrium doping [20, 21]. However, such a consideration is not completely satisfactory for the following reason: the oxide on the Fe–Cr–Al–Y alloy remains flat even after very long oxidation times and the growth stress remains high. On the other hand, after prolonged oxidation, a relatively thick scale on the Fe–Cr–Al alloy continues to deform under small, if any, growth stress, which is evident from the continuous evolution of the wrinkling wavelength and amplitude (Fig. 5). In order to explain the difference between the two alloys, it should be noted that the value of the growth stress at any given time represents the result of two concurrent and competing processes in the scale: stress generation and stress relief. A comparison of the growth stresses on the two alloys (Fig. 12) has already demonstrated that the existence of a very high stress in the scale on the yttrium-containing alloy is not sufficient to cause wrinkling. Another factor appears to be most significant in determining whether the oxide remains flat or assumes a wrinkled configuration, namely,

the lateral growth strain of the oxide. Following the arguments used to describe the stress generation during oxidation [12], we suppose that the stresses develop when the scale grows in the lateral direction but is constrained by the underlying metal. (The growth in the direction normal to the surface is not constrained and produces an increase in oxide thickness.) While the mechanism of such lateral growth is not known, the Rhines-Wolf model [3], suggesting the formation of oxide within the existing layer, seems to be the most plausible explanation.

Quantification of the scale morphology on the Fe-Cr-Al alloy makes it possible to determine the lateral growth from the measured surface area of the scale. As shown in Fig. 5(c), the surface area of the wrinkled oxide is substantially larger than the initially flat surface. The increase of the surface area can be described by a strain, ϵ_w , obviously plastic, which can be obtained from the surface area ratio:

$$\epsilon_w = \sqrt{1 + \frac{\Delta S}{S_0}} - 1 \quad (8)$$

where the ratio of surface area increase to the initial surface area, $\Delta S/S_0$, is taken from the AFM roughness analysis [Fig. 5(c)]. Figure 13 shows the time variation of the strain ϵ_w , defined in this way, for the three orientations of the Fe-Cr-Al alloy. This experimentally measured strain represents a sum of the growth strain, ϵ_{growth} , and elastic strain, ϵ_{el} , in the scale during oxidation

$$\epsilon_w = \epsilon_{\text{growth}} + \epsilon_{\text{el}} \quad (9)$$

In turn, the elastic strain is given by the growth stress value

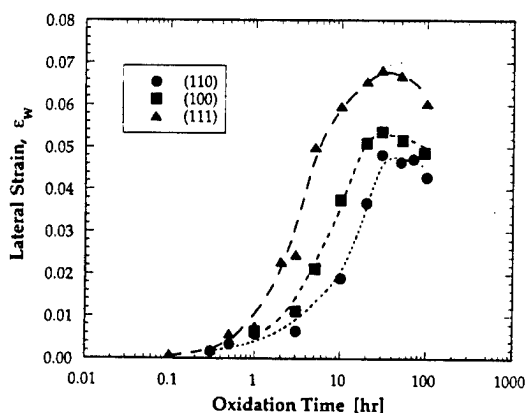


Fig. 13. Lateral strain of the wrinkling α -Al₂O₃ scale on different orientations of the Fe-Cr-Al alloy determined from the oxide surface area enlargement according to equation (8). This strain represents plastic deformation associated with oxide wrinkling. The surface area enlargement, $\Delta S/S_0$, is taken from the AFM roughness analysis [Fig. 5(c)].

$$\epsilon_{\text{el}} = \sigma_G \frac{1 - \nu_{\text{ox}}}{E_{\text{ox}}^T} \quad (10)$$

where the stress σ_G is determined by equation (5) and presented in Fig. 12. This strain is taken to be negative because the oxide is under compression. Combining equations (8)–(10), the growth strain is:

$$\epsilon_{\text{growth}} = \left(\sqrt{1 + \frac{\Delta S}{S_0}} - 1 \right) - \frac{\sigma_G(1 - \nu_{\text{ox}})}{E_{\text{ox}}^T} \quad (11)$$

Note that all strains are considered at temperature, therefore the thermal strains are not included. We also suppose that the oxide morphology does not change during cooling so the surface area, measured at room temperature, is the same as at the oxidation temperature.

The growth strain defined by equation (11) for the oxide formed on the Fe-Cr-Al alloy is presented in Fig. 14. For comparison, the growth strain for the Fe-Cr-Al-Y alloy is included. The elastic contribution [the second term on the right-hand side of equation (11)] is rather small for the Fe-Cr-Al alloy, whereas it is the only contribution included for the flat oxide on the Fe-Cr-Al-Y alloy. The difference between the oxide growth strains for the two alloys is remarkable. From the very beginning of oxidation the growth strain is substantially larger on the Fe-Cr-Al alloy and rapidly increases with time reaching a value of 5–6%, more than an order of magnitude higher than on the Fe-Cr-Al-Y alloy. After about 20–30 h, the growth strain does not increase on the Fe-Cr-Al alloy. Apparently, the oxide wrinkling is not a continuous process: it takes place during initial stages, gradually slows down and eventually stops after prolonged oxidation.

Strictly speaking, there should be additional terms on the right-hand side of equation (11). First and foremost, a plastic relaxation in the oxide that

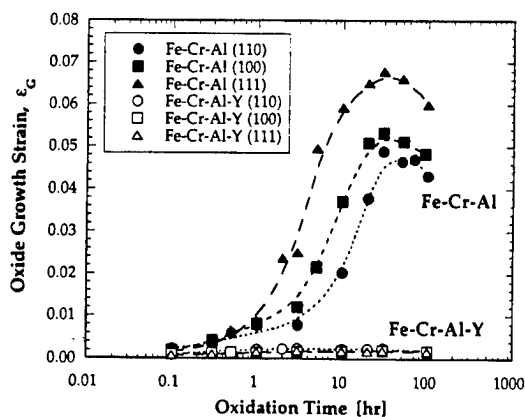


Fig. 14. Lateral growth strain of the oxide on the Fe-Cr-Al (solid symbols) and Fe-Cr-Al-Y (open symbols) alloys calculated according to equation (11).

occurs without wrinkling should be mentioned. The existence of this relaxation mode has been recently demonstrated for the Fe–Cr–Al–Y alloy oxidized at 1100–1300°C [12, 22]. The oxide creep, presumably in the direction normal to the surface, provides a way to accommodate the lateral growth strain of the order of a few percent at higher temperatures and longer times. Perhaps the columnar grain structure of the scales with yttrium makes this type of plastic deformation preferable to wrinkling on the yttrium-free alloy where the oxide grains are equiaxed. In the present work, we could not quantify the oxide creep contribution for the Fe–Cr–Al–Y alloy. However, it might be quite significant as the growth stress is very high in the scale at 1000°C. For the Fe–Cr–Al alloy, an additional oxide creep normal to the interface is also possible, most probably during initial stages when the growth stress is high. This correction would shift the curves of the growth strain, ϵ_{growth} , in Fig. 14 upwards.

Another term describing metal elongation [12] during oxidation should also be included in equation (11). This strain, however, was too small to be detected experimentally in this work. As mentioned previously, a possible metal elongation that could remain undetected is about 10^{-3} . Thus, the actual growth strain values for the Fe–Cr–Al–Y alloy in Fig. 14 may be up to 10^{-3} higher after longer times (when the metal elongation might be expected). For the Fe–Cr–Al alloy this correction is insignificant because, when the oxide becomes relatively thick, the growth stress is already small. With all the uncertainties indicated, the difference between the growth strains for the two alloys may in fact not be quite so large as that presented in Fig. 14, but they will nevertheless be substantially different.

No reliable explanation can be offered at this time as to why the lateral growth of the oxide on the Fe–Cr–Al alloy apparently terminates after certain oxidation exposure. One possibility is that the growth strain actually continues to increase, while the plastic relaxation occurs not only by oxide wrinkling but also by creep in the direction normal to the surface. As a result, the growth strain at this stage can be accommodated without increasing the surface area. On the other hand, a small growth stress in the oxide after prolonged oxidation indicates that this relaxation is very unlikely.

5. CONCLUSIONS

Measurements of the surface topography of α - Al_2O_3 scales formed on single-crystalline Fe–Cr–Al alloys during oxidation at 1000°C show that the wrinkling of the scale depends on the initial crystallographic orientation of the alloy surface. The residual room-temperature stress in the scales also depends on the alloy orientation and varies with oxidation time. These experimental results were

used to evaluate the growth stress in the scale and its evolution during oxidation.

Wrinkling is more extensive on the (111) orientation, which leads to fast relaxation of the growth stresses in the scale. Wrinkling is retarded on the close-packed (110) plane and, correspondingly, the growth stress is higher. After oxidation for about 30 h, the difference between metal orientations becomes negligible. The time evolution of the geometrical parameters describes the process of wrinkling in terms of the surface area enlargement. Experimental results show that wrinkling of the scale on the Fe–Cr–Al alloy is apparently a transient process that takes place during 20–30 h at 1000°C. Further oxidation does not produce additional enlargement of the surface area, while the plastic deformation of the scale continues. This follows from a continuous increase of the amplitude and wavelength of oxide undulations.

Except for the first few hours of oxidation, the growth stress in the scale is higher on the Fe–Cr–Al–Y alloy than on the yttrium-free alloy. However, no wrinkling occurs, primarily it is concluded, because of a smaller growth strain in the scales in the presence of yttrium.

Acknowledgements—This work was supported by the Office of Naval Research under grant N00014-97-1-0190 and also made use of the MRL Central Facilities supported by the National Science Foundation under Award No. DMR-9123048. The authors are thankful to H. J. Grabke (MPI, Düsseldorf) for providing single-crystal specimens for this study.

REFERENCES

1. Stott, F. H., Wood, G. C. and Stringer, J., *Oxid. Metals*, 1995, **44**, 113.
2. Golightly, F. A., Stott, F. H. and Wood, G. C., *Oxid. Metals*, 1976, **10**, 163.
3. Rhines, F. N. and Wolf, J. S., *Metall. Trans.*, 1970, **1**, 1701.
4. Suo, Z., *J. Mech. Phys. Solids*, 1995, **43**, 829.
5. Hou, P. Y., Cannon, R. M., Zhang, H. and Williamson, R. L., in *Proc. Symp. on Fundamental Aspects of High Temperature Corrosion*, ed. D. A. Shores, R. A. Rapp and P. Y. Hou. Electrochemical Society, Pennington, NJ, 1997, pp. 28–40.
6. Smeggil, J. G., *Mater. Sci. Engng*, 1987, **87**, 261.
7. Grabke, H. J., Kurbatov, G. and Schmutzler, H. J., *Oxid. Metals*, 1995, **43**, 97.
8. Meier, G. H., Pettit, F. S. and Smialek, J. L., *Werkstoffe Korros.*, 1995, **46**, 232.
9. Evans, A. G., Crumley, G. B. and Demaray, R. E., *Oxid. Metals*, 1983, **20**, 193.
10. Chao, J. and Gonzalez-Carrasco, J. L., *Mater. Sci. Engng*, 1997, **A230**, 39.
11. Gong, X.-Y. and Clarke, D. R., *Oxid. Metals*, 1998, **50**, 355.
12. Tolpygo, V. K., Dryden, J. R. and Clarke, D. R., *Acta mater.*, 1998, **46**, 927.

13. Tolpygo, V. K. and Clarke, D. R., *Acta mater.*, 1998, **46**, 0000 (submitted).
14. Tolpygo, V. K. and Grabke, H. J., *Oxid. Metals*, 1994, **41**, 343.
15. Ma, Q. and Clarke, D. R., *Acta metall. mater.*, 1993, **41**, 1811.
16. Lipkin, D. M. and Clarke, D. R., *Oxid. Metals*, 1996, **45**, 267.
17. He, J. and Clarke, D. R., *J. Am. Ceram. Soc.*, 1995, **78**, 1347.
18. Munro, R. G., *J. Am. Ceram. Soc.*, 1997, **80**, 1919.
19. Smialek, J. L. and Gibala, R., *Metall. Trans.*, 1983, **14A**, 2143.
20. French, J. D., Zhao, J., Harmer, M. P., Chan, H. M. and Miller, G. A., *J. Am. Ceram. Soc.*, 1994, **77**, 2857.
21. Fang, J., Thompson, A. M., Harmer, M. P. and Chan, H. M., *J. Am. Ceram. Soc.*, 1997, **80**, 2005.
22. Tolpygo, V. K. and Clarke, D. R., *Oxid. Metals*, 1998, **49**, 187.



WRINKLING OF α -ALUMINA FILMS GROWN BY OXIDATION—II. OXIDE SEPARATION AND FAILURE

V. K. TOLPYGO and D. R. CLARKE†

Materials Department, College of Engineering, University of California, Santa Barbara, CA 93106-5050, U.S.A.

(Received 20 February 1998; accepted 30 March 1998)

Abstract—Two types of localized separation of the α -Al₂O₃ scale, grown on a Fe–Cr–Al alloy at 1000°C, occur after isothermal oxidation and cooling to room temperature. One type is a form of buckling where the size of the detached region is much larger than the thickness of the oxide and is usually accompanied by substantial stress relaxation and cracking of the scale. It is observed within a narrow range of oxide thickness of about 0.2–0.5 μ m. The second type is intimately related to the wrinkling morphology of the scale and takes place primarily along the ridges of the longer wavelength wrinkles. No significant stress relaxation in the oxide appears to accompany this form of separation unless cracking of the scale occurs as well. The consequences of thermal cycling on these modes of separation and how they may lead to oxide spalling are discussed. © 1998 Acta Metallurgica Inc. Published by Elsevier Science Ltd. All rights reserved.

1. INTRODUCTION

High-temperature oxidation of Fe–22% Cr–5% Al alloy results in the formation of a continuous surface layer of α -Al₂O₃ with a typical wrinkled or convoluted morphology. In the first part of this work, the evolution of the wrinkling morphology during oxidation was quantified in terms of the amplitude and wavelength of the undulations and these geometric parameters were related to the residual stress in the oxide [1]. In this second part, a similar Fe–Cr–Al alloy but in polycrystalline form is examined with the emphasis placed on observations of the separation of the oxide from the underlying alloy and its relation to the wrinkling morphology. Two distinct forms of localized separation are observed. These are believed to be precursors to the spalling failure of the oxide under cyclic oxidation conditions.

2. EXPERIMENTAL

The chemical composition of the alloy studied was similar to that used in the first part, namely (wt%): Fe (bal.)–22.0% Cr–5.28% Al. The content of impurities was determined to be: 82 p.p.m. C; 49 p.p.m. S; 23 p.p.m. P; 120 p.p.m. Si. The alloy was vacuum-induction melted, annealed at 1100°C and cut into rectangular specimens. The specimens were mechanically polished to a 1 μ m surface finish and oxidized in air at 1000°C. The oxide scale was studied using optical and scanning electron microscopy (SEM) and the residual stress in the oxide measured using photostimulated chromium lumines-

cence piezospectroscopy [2]. All the relevant experimental details are given in the first part [1].

3. RESULTS

3.1. Observations of scale separation

The wrinkled scale generally exhibits good spalling resistance after isothermal oxidation at 1000°C. However, the oxide does not remain in contact with the metal after cooling to room temperature everywhere over the surface. Observations using a conventional optical microscope in the back-reflection mode reveal localized oxide separation or debonding but no visible spalling. Any debonded (but not spalled) areas of the scale larger than a few micrometers are clearly observed through an optical microscope as brighter regions [Figs 1(a) and 2]. The origin of this optical contrast is believed to be as follows. The oxide is transparent in the visible spectrum and so most of the reflection of incident light comes from the metal surface. Since the difference in index of refraction of the metal–gas interface is higher than that of the metal–oxide interface [3], the metal surface under debonded oxide appears brighter than the same surface in contact with the oxide. An additional observation made was that the debonded regions of the scale form during cooling within a few minutes after removing a specimen from the furnace. This indicates that the debonded regions “pop-in” on cooling rather than steadily grow as the temperature decreases.

Similar optical contrast is observed when large interfacial cavities form during oxidation. In this case, a higher reflectivity of these regions is also

†To whom all correspondence should be addressed.

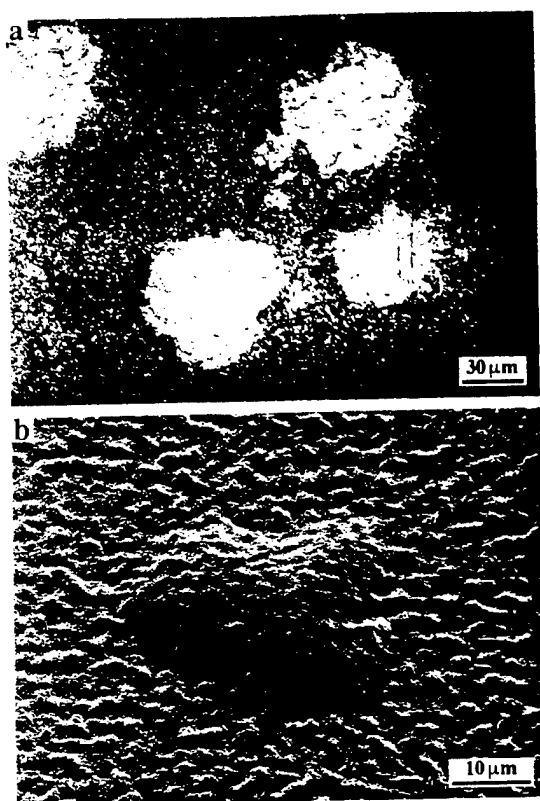


Fig. 1. Local buckling of the alumina scale on the Fe-Cr-Al alloy after oxidation for 10 h at 1000°C: (a) optical micrograph showing the detached regions of the scale apparent from their higher reflectivity; (b) scanning electron micrograph showing the pronounced oxide up-lift associated with the buckling ("blistering").

due to the smooth metal surface at the bottom of the cavity. Generally, it is not possible to distinguish the localized separation induced by cooling and the cavities formed during oxide growth, unless the scale is separated and the oxide-metal interface is exposed for direct observation. In the present case, as indicated earlier [1], almost no cavities formed during isothermal oxidation, so nearly all the debonded areas arise on cooling. (Cyclic oxidation, however, may result in cavity formation at high temperature as will be discussed later.) Spallation of the scale, exposing a bare metal surface, produces even more distinct optical contrast and can easily be detected and distinguished from the oxide-metal separation described below.

Two types of oxide separation and debonding were observed. One is in the form of large blisters such as shown in Fig. 1. These are dome-shaped regions of the scale, 20–40 μm in diameter, elevated up to a few micrometers above the metal surface. Another distinguishing feature is that the area of a single blister covers a number of oxide wrinkles. Since the metal surface under the blisters is seen to replicate the wrinkles and grain structure of the scale, it is concluded that the debonding must have occurred on cooling, not during the scale growth.

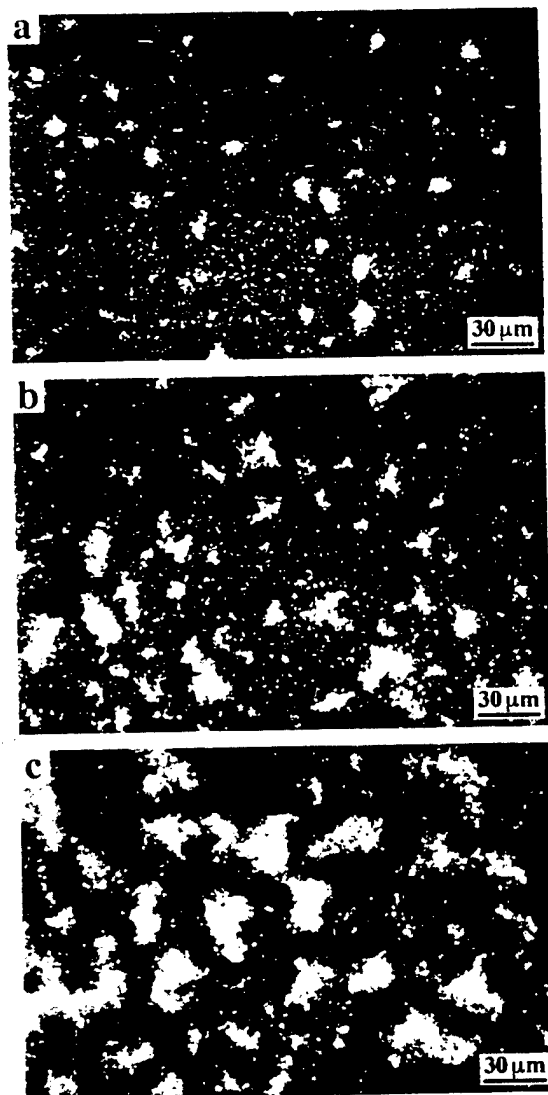


Fig. 2. The second type of oxide detachment discernible by its higher optical reflectivity. The detached regions increase in size with increasing oxidation time: (a) 30 h; (b) 100 h; (c) 400 h (optical micrographs).

Usually, the perimeter of the blisters is fringed by cracks which most probably inhibit lateral propagation of the blisters. However, in cyclic oxidation experiments, the cracks often lead to spalling of the buckled regions of the scale. This type of separation was observed after oxidation for 3–20 h when the oxide is still relatively thin, typically only about 0.2–0.5 μm thick. Interestingly, for thinner scales, no separation was observed and the oxide remained perfectly adherent after isothermal oxidation.

The second type of debonding is shown in the sequence of optical micrographs in Fig. 2. These smaller regions are also visible through an optical microscope but, importantly, cannot be revealed in SEM images. They appear after oxidation for 20–25 h and both their size and number increase after longer oxidation times. Comparing the size of

debonded regions with the wrinkling wavelength measured in the first part [1], it is concluded that each corresponds to the crest of the wrinkles in the scale. This becomes clear after prolonged oxidation when individual wrinkles can be resolved by optical microscopy. For instance, after 400 h oxidation the scale at almost every crest or ridge is debonded after cooling to room temperature [Fig. 2(c)].

A closer examination of relatively thick scales after 200–400 h oxidation reveals small cracks (Fig. 3). These cracks can be found near the most pronounced ridges (but never at the valleys) of the scale. Both the debonded regions and the cracks do not propagate over larger areas, at least after isothermal oxidation and air cooling, therefore no spalling occurs. In cyclic tests, however, a gradual accumulation of the debonded regions results in oxide spalling.

It was found that both types of oxide debonding are greatly affected by cooling rate. The separations presented in Figs 1–3 were observed after fast air cooling (about 500°C/min). With decreasing cooling rate, the number of debonded areas is smaller, for example after furnace cooling at 5–10°C/min. Conversely, quenching from the oxidation temperature significantly enhances the scale debonding and invariably leads to local spalling.

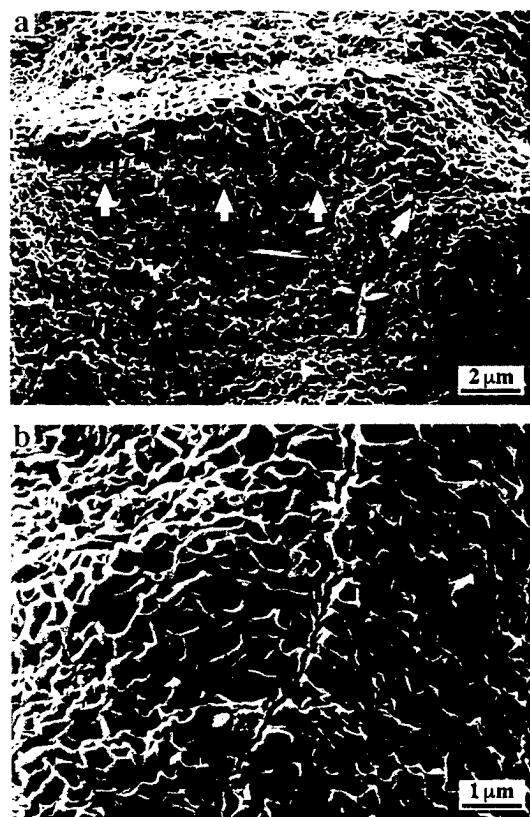


Fig. 3. SEM micrographs showing the presence of micro-cracks in thick scales after oxidation for 400 h at 1000°C. The crack is indicated by arrows in (a) and shown at higher magnification at the crest of oxide wrinkle in (b).

The observations of oxide debonding presented so far clearly show that it occurs after cooling to room temperature whereas, during isothermal exposure, the scale remains in contact with the metal. Cyclic oxidation, however, leads to localized debonding at high temperature. This process causes the formation of interfacial cavities which appear as smooth craters on the metal surface. A typical structure of the metal surface exposed by spalling of the scale after five 50 h oxidation cycles (250 h total exposure at 1000°C) is shown in Fig. 4(a). No such cavities were observed after isothermal oxidation. For instance, the SEM micrograph showing the absence of cavities on the metal surface after isothermal oxidation for 20 h at 1200°C is presented in Fig. 4(b). The oxide adherence after isothermal oxidation at 1000°C was strong enough, so that only small areas of the oxide could be removed to reveal the underlying metal surface. Therefore, for illustrative purposes, the interfacial structure is shown after oxidation at 1200°C, when the scale spalled almost completely.

3.2. Residual stress in the oxide

Measurements of the residual stress in the oxide scale at room temperature after isothermal oxidation at 1000°C were made using photostimulated

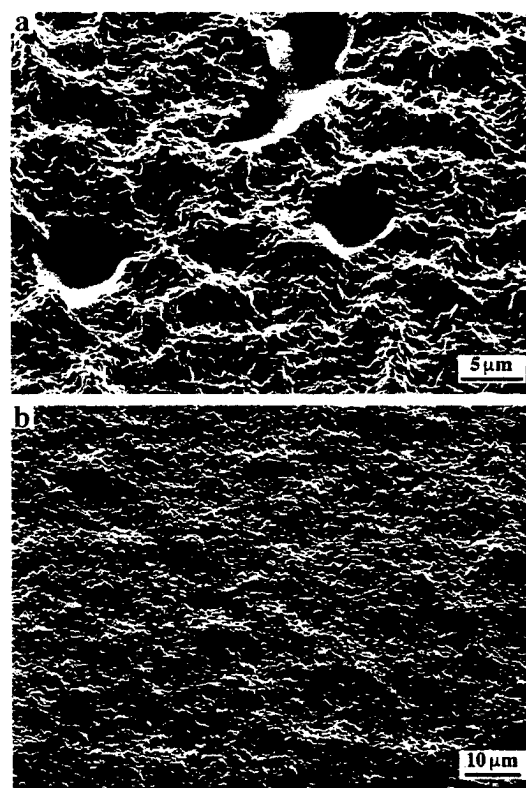


Fig. 4. The microstructure of the metal surface exposed by spalling of the scale: (a) after five 50 h oxidation cycles at 1000°C showing interfacial cavities (smooth craters) and imprinted contact interface; (b) after 20 h isothermal oxidation at 1200°C showing the absence of cavities.

luminescence spectroscopy [2]. Two types of measurement were made: one with a probe size comparable to the oxide wrinkling wavelength so as to obtain the spatial average of the residual stress, and the other with a much smaller probe so that the local residual stress could be determined. No systematic difference between the average residual stress was detected after isothermal and cyclic oxidation (for times $t \leq 100$ h) of the same cumulative exposure. This suggests that cooling from the oxidation temperature does not lead to irreversible plastic relaxation in the scale. With increasing time of cyclic oxidation, however, local spalling and cracking of the scale occurred, therefore the results presented in the following paragraphs refer only to isothermal oxidation.

Apart from significant variations at short oxidation times due to differences in crystallographic orientation of the underlying metal grains [1], the value of the spatial average of the residual stress became almost constant after about 60 h oxidation at 1000°C [Fig. 5(a)]. By this time, the wrinkling wavelength was sufficiently large, so that the residual stress in the vicinity of the ridges and the valleys between them could be measured with a small ($< 3 \mu\text{m}$) optical probe. The results are shown in Fig. 5(a) together with the spatial average values. Here, the piezospectroscopic frequency shift is presented as a function of oxidation time, and the second y-axis indicates the stress calculated from the frequency shift assuming that the oxide is under biaxial compression. Note that these stress values are not directly applicable for the wrinkled oxide, as discussed previously [1,4], and can only be used for a flat oxide layer. For comparison, the residual stress in the flat scale formed on the yttrium-containing alloy is included [5]. Two luminescence spectra in Fig. 5(b) illustrate a marked difference between the ridge and valley regions of the scale after oxidation for 400 h. Clearly, the frequency shift is much smaller on the oxide ridges and larger at the valleys. The implications of these results with respect to the local stress state of the scale will be discussed below.

As shown in Fig. 2(c) (400 h oxidation), a large proportion of the scale, namely the majority of ridge regions, is debonded from the metal surface after cooling to room temperature. It is, therefore, natural to suppose that the stress in the oxide near the ridges can, at least partially, be relieved as a result of scale separation during cooling. After shorter oxidation time [Fig. 2(b), 100 h], some oxide ridges are debonded, however there are many others where the scale apparently remains in contact with the metal. These two regions were analyzed using a small probe size in order to compare the frequency shifts between the debonded and intact ridges. Surprisingly, no systematic difference between these two has been detected (Fig. 6). In other words,

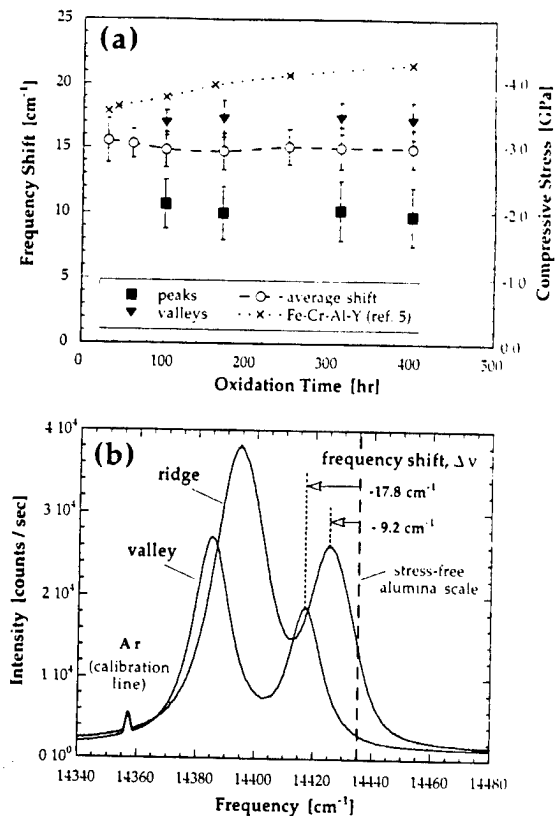


Fig. 5. Piezospectroscopic stress measurements of the wrinkled alumina scales after isothermal oxidation at 1000°C: (a) piezospectroscopic frequency shift from ridges and valleys of the wrinkles, measured with a small probe size (solid symbols), and spatially averaged values, measured with a large probe size (open circles) as a function of oxidation time (the frequency shift obtained on the yttrium-containing alloy [5] is shown for comparison); (b) example of luminescence spectra recorded from the ridges and valleys after oxidation for 400 h (dotted line indicates the frequency of R_2 -line for the stress-free alumina scale).

scale debonding along the ridges does not produce significant stress relaxation in the oxide.

When the cracked regions of the scale were examined, the resulting luminescence peaks were generally found to be highly non-symmetrical indicating a large variation in stress within the probed volume [6]. In addition, the piezospectroscopic measurements from such places usually gave significantly smaller (sometimes nearly zero) frequency shifts, as shown in Fig. 6. In fact, the large difference in the shifts between cracked and intact regions of the scale makes it possible to ascertain which regions of the scale contain cracks and which remain intact. The frequency shift obtained from large blisters is almost always very close to zero presumably because of the cracks at their perimeter.

4. DISCUSSION

The microstructural observations described indicate that two quite distinct modes of oxide-metal separation can occur during cooling of wrinkled

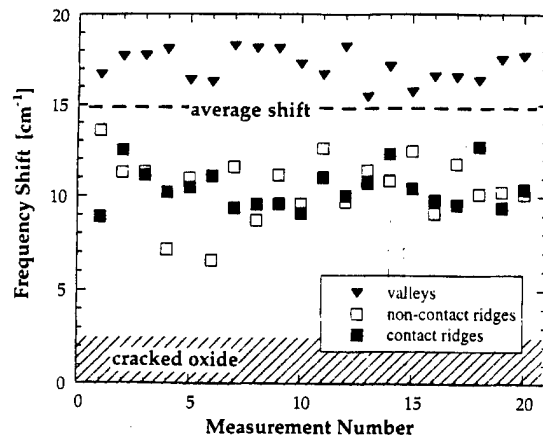


Fig. 6. Results of a series of measurements of the wrinkling scale after 100 h oxidation. The difference in optical reflectivity allows the debonded and the regions in contact with the scale to be distinguished in the course of piezospectroscopic measurements. Both the debonded and contact ridges show similar frequency shifts. The dashed area indicates a typical range of measured shifts from the cracked oxide.

alumina scales. One is a form of buckling in which a large area, of dimensions much larger than the oxide thickness, of the scale separates from the underlying metal (Fig. 1). This form of failure is accompanied by distinct cracks through the oxide at the periphery of the buckle, a displacement away from the metal surface and a relaxation of the residual stress in the oxide in the buckled region. The observations show that it occurs occasionally and at random locations on the metal surface after short isothermal oxidation times, when the scale is relatively thin. The reason for this buckling is not known but it is assumed to be due to the presence of localized patches of (unidentified) impurities that significantly decrease the local interfacial fracture resistance. The size of these blistered regions is consistent with that calculated from the usual mechanics criteria [7-9] for buckling of a compressively stressed thin film, namely that the buckle diameter, a_c , is given by

$$a_c = gh \sqrt{\frac{E}{\sigma_c}} \quad (1)$$

and the elastic strain energy relieved exceeds the interface fracture resistance. In this equation, g is a geometric parameter ($g \approx 2.2$ for an axisymmetric buckle), h the scale thickness, E the oxide elastic modulus, and σ_c the biaxial compressive stress. Substituting in appropriate values ($h \sim 0.5 \mu\text{m}$, $\sigma_c \sim 3 \text{ GPa}$ and $E \sim 400 \text{ GPa}$), the predicted buckle size is about $12 \mu\text{m}$, a value similar to that seen in Fig. 1.

The second type of separation is directly related to the wrinkling morphology, occurring primarily along the crests of the wrinkles with equal probability all over the metal surface (Fig. 2). It is the

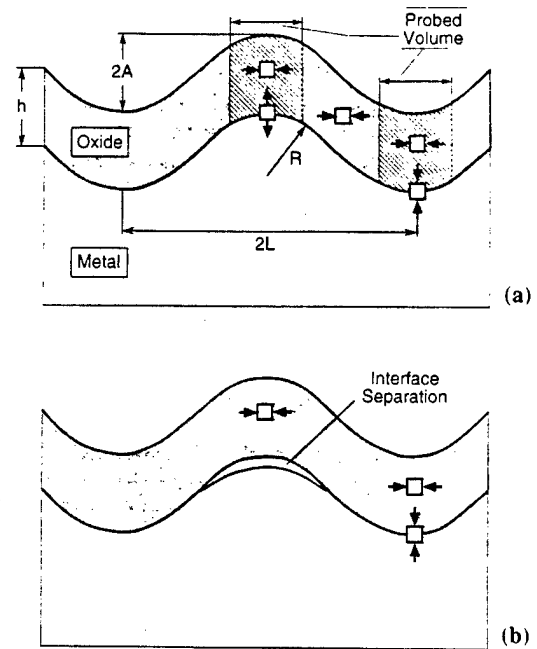


Fig. 7. Schematic diagram illustrating the state of residual stress in a wrinkled oxide scale: (a) oxide remains in contact with the metal surface. For comparison, the approximate size of the probed volume used to measure the stresses in the ridge and valley is also shown; (b) interface separation (debonding) at the wrinkling ridge as a result of tensile stresses normal to the interface; the oxide remains in contact at surrounding valleys where the stress across the interface is compressive.

most common form of oxide separation after isothermal oxidation at 1000°C for 25-400 h in the experiments but, importantly, it does not cause spalling of the scale. There appears to be almost no accompanying stress relaxation in the oxide unless cracking of the scale also occurs.

Debonding of the scale at the crests and ridges is attributed to the existence of local tensile stresses across the oxide-metal interface created from the thermal mismatch stress in the scale as a result of the wrinkling geometry. Both analytical solutions [4, 9] and finite element calculations [4, 10] show that cooling of the wrinkled scale produces regions of tensile stress across the interface at the ridges and corresponding compressive stress in the valley regions. (For all but the most convoluted scales, the finite element results for the tensile stress across the interface can be represented with considerable accuracy by using a soap-film analogy in which the normal stress is given by the Laplace equation, namely the biaxial stress divided by the local curvature [4].) The results (Figs 5 and 6) confirm this conclusion since the piezospectroscopic frequency shift is much higher at the valleys than at the ridges. A schematic illustration of the oxide wrinkling morphology is shown in Fig. 7(a). The stress component normal to the interface varies

from a maximum tensile value to zero in the ridge region and from a maximum compressive value to zero in the valley region [4, 9, 10]. For the small volumes of the oxide analyzed by the optical probe, these normal stresses contribute with opposite sign to the piezospectroscopic shift, therefore causing the frequency shift from the ridge to be smaller than the spatial average and that from the valley to be larger. The maximum magnitude of the normal stress at the interface is in the range $(0.1-0.4)\sigma_{\text{flat}}$ [4], where σ_{flat} is the residual biaxial compression of the flat oxide layer. A typical value for σ_{flat} caused by thermal expansion mismatch is about 3.0–3.2 GPa. Thus, the magnitude of the maximum tensile stress is expected to be 0.3–1.3 GPa depending on the geometry of the oxide wrinkles. It is argued in the following paragraphs that the existence of spatially varying tensile and compressive stresses across the oxide-metal interface has two consequences that are consistent with observations associated with the second type of detachment: the interface separation along the ridges with no stress relaxation and the observed size of the detached regions.

The piezospectroscopic measurements of the scale around the wrinkling ridges demonstrate that no systematic difference exists between the areas where oxide is detached (without cracking) and the areas where it apparently remains in contact with the metal (Fig. 6). This means that separation during cooling does not lead to significant stress relaxation in the oxide and raises the question of why the observed separation occurs. To answer the question, the stresses need to be considered not only in the oxide layer, but also in the underlying metal. In contrast to the stress distribution at the planar interface, where a biaxial uniform tension in the metal can usually be ignored (the stress in the metal is very small if the oxide is much thinner than the metal), the stresses in the metal beneath the wrinkled interface are inhomogeneous and may be sufficiently large in some locations, as discussed above, so as to cause metal deformation. If the oxide does not deform, the most probable result of metal deformation is debonding at the interface. This process will create isolated crescent-shaped separations at the concave regions of the interface during cooling [Fig. 7(b)]. So, unlike buckling (Fig. 1) where the oxide layer bends away from the metal surface, these smaller debonded regions are believed to be due to the deformation (plastic, elastic, or both) of the underlying metal.

The existence of a tensile stress acting normal to the oxide-metal interface is commonly considered to be an essential pre-requisite for oxide separation and spalling. However, the separation observed in the ridge areas does not lead to spalling of the scale, at least within the oxidation times studied (400 h at 1000°C). The reason is, probably, that each crest or ridge of the scale is surrounded by regions where the stress across the interface is com-

pressive. Thus, the size of the detached regions is expected to be related to the size of the regions over which tensile stresses are created, i.e. about half of the wrinkling wavelength. In fact, consideration of the energy associated with the separation suggests that, as with other fracture phenomena, there will be a critical size below which separation cannot occur whereas above which it will occur. The existence of a critical size is consistent with two of the observations mentioned above. Firstly, that separations at the ridges only occur after some intermediate oxidation time, 20–25 h at 1000°C, and secondly, that the separations "pop-in" on cooling. As shown in the quantitative morphological investigations described in part I [1], both the wavelength and amplitude of the wrinkles increase with oxidation time, so the critical size of separation corresponds to approximately half of the wrinkling wavelength after 20–25 h, i.e. about 3.5 μm . The observation of separation "pop-in"—the sudden growth to a stable size—is characteristic of crack-like growth in a spatially varying stress field and then arrest when the strain energy release rate falls below the interfacial fracture resistance.

Provided that the size of separated regions is less than the critical buckling size, the scale cannot buckle. Following these arguments, the extensive spalling of the scale after oxidation at 1200°C may simply be related to a substantially larger wrinkling wavelength, as shown in Fig. 4(b). Certainly, with increasing oxidation temperature, the thermal mismatch strain increases, and so the elastic strain energy, available for decohesion, is greater in the thicker scales formed at the higher temperatures. Both factors lead to propagation of the detached regions beyond a single ridge of the interface and cause spalling of large areas of the scale. The progressive increase in size of the separated regions along the ridges with time of isothermal oxidation at 1000°C is associated with the coarsening of the wrinkling morphology, specifically the growth of the larger wavelength undulations at the expense of the shorter wavelength undulations [11]. The observation that not all the interfaces along the ridges are separated [for example, after 100 h in Fig. 2(b)] further suggests that it is primarily the larger sized ridges that separate. Furthermore, spalling of the scale after oxidation at higher temperatures [Fig. 4(b)] is probably best described in terms of percolation of separated regions. It is expected that once the connected regions of separation reach the critical buckle size, buckling and spalling spontaneously occur.

Cracking of the oxide takes place at, or near, the ridges in the wrinkling scale after prolonged isothermal oxidation, for instance 200–400 h at 1000°C (Fig. 3). It is believed to be associated with the development of tangential tensile stresses at the outer surface of debonded oxide once a critical thickness of the scale is reached. Cracking leads to

stress relaxation in the adjacent area of the oxide (as confirmed by piezospectroscopic measurements), including the normal tensile component. No cracking was observed in the adjoining valleys where the oxide remains under compression. Cracking is also observed at the periphery of the buckled regions in thin scales (Fig. 1), presumably in response to the large deformations associated with the buckling event.

The existence of debonded regions of the scale after cooling to room temperature raises the question as to what happens with such regions during cyclic oxidation. Obviously, if oxide detachment is accompanied by cracking, then oxygen can penetrate into the gap between the scale and the metal and form a secondary oxide layer during subsequent oxidation cycles. This process was, in fact, observed in the case of the large blisters shown in Fig. 1 in the course of 5 or 10 h oxidation cycles. However, the smaller debonded regions (Fig. 2) are usually not cracked. It can be expected, therefore, that the separation between the scale and the metal

will close during subsequent heating and the oxide-metal contact will be restored at temperature until the next cooling. The major requirement for such a repeated debonding-bonding process, besides the absence of cracks, is a purely elastic behavior of both the metal and oxide during temperature change. If decohesion occurs without plastic deformation in both phases, the oxide inner surface and metal surface should perfectly match each other after next heating to oxidation temperature. This possibility is schematically shown in Fig. 8 (route I).

Although it is difficult to prove experimentally, it is supposed that repeated debonding-bonding may indeed occur in some cases, i.e. the changes of the oxide and metal surface configuration within the debonded region can be completely reversible. There are, however, at least two factors which complicate this simple conclusion. First, as mentioned previously, metal plastic deformation may in fact occur during cooling, especially, at the perimeter of the debonded region, where the shear stresses are

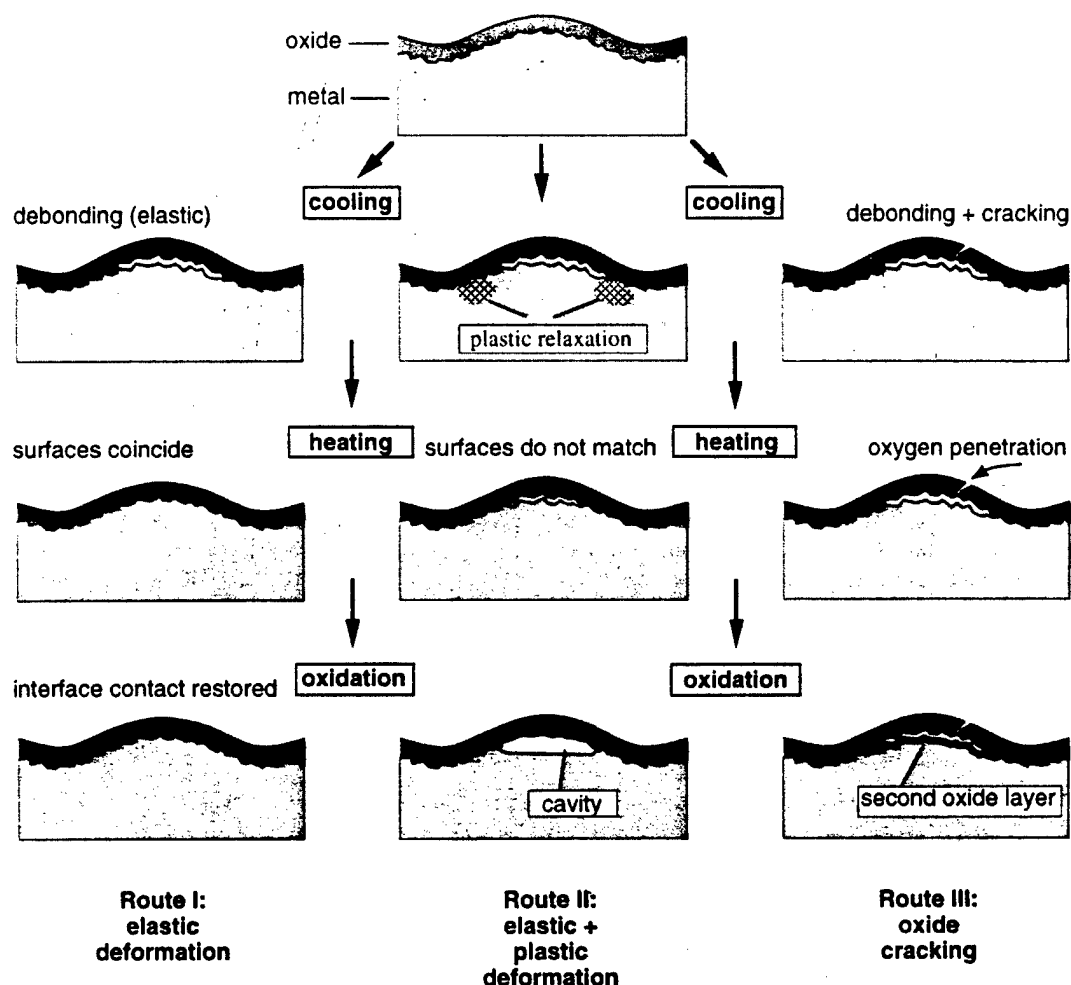


Fig. 8. Schematic diagram illustrating three different routes of oxide debonding and failure during cyclic oxidation.

highest and where significant stress gradients develop between separated and contact areas. This is illustrated in Fig. 8 (route II). Any plastic deformation of the metal surface would lead to a geometrical mismatch with the oxide inner surface during subsequent heating. Second is a complex morphology of the oxide-metal interface itself. The interface is formed by facets of alumina grains of various orientations and their replicas on the metal surface. Simple geometric considerations imply that it is unlikely to restore intimate contact after separation over the whole interface. For both reasons, many debonded regions remain after next heating. During subsequent oxidation exposure, these regions transform into normal interfacial cavities with smooth surface at the metal side in order to minimize surface energy [Fig. 4(a)]. That is probably the reason why cavities can be observed after cyclic oxidation but not after isothermal oxidation of the same total exposure. Certainly, if separation after cooling is followed by oxide cracking, a similar geometrical mismatch at the interface would prevent contact from being restored (route III in Fig. 8).

In these examples of oxide detachment, spalling was not specifically considered since it did not occur after isothermal oxidation at 1000°C. However, spontaneous spalling with a loss of a significant portion of the scale was observed in the experiments under cyclic conditions. During cyclic oxidation, accumulation of local damage in the scale (through-cracks, debonded regions around ridges) and formation of interfacial cavities (as described above) result in the development of large debonded areas which eventually separate from the metal after a number of cycles.

5. CONCLUSIONS

Two distinct forms of detachment of the alumina scale from the underlying Fe-Cr-Al alloy occur after isothermal oxidation at 1000°C and cooling to room temperature. One is a conventional form of buckling which is observed in the case of relatively

thin scales (0.2–0.5 μm) and may be attributed to the presence of localized patches of impurities at the interface that form a critical flaw size for the onset of buckling. The other, and more general, is associated with the ridges in the wrinkling morphology and resulting local tensile stresses across the oxide-metal interface. The size and the number of separated regions increase with oxidation time as the wavelength of oxide wrinkles increases. No significant stress relaxation in the oxide is associated with this form of oxide-metal separation and so it is believed to be attributed to the underlying metal contracting away from the oxide on cooling. Localized separation of the scale after isothermal oxidation does not lead to spalling. During cyclic oxidation, the separated regions can propagate over larger areas of the interface and lead to failure of the scale by complete detachment from the metal surface.

Acknowledgements—It is a pleasure to acknowledge support for this research from the Office of Naval Research through grant N00014-97-1-0190.

REFERENCES

1. Tolpygo, V. K. and Clarke, D. R., *Acta mater.* (this issue).
2. Ma, Q. and Clarke, D. R., *J. Am. Ceram. Soc.*, 1993, **76**, 1433.
3. Heavens, O. S., *Optical Properties of Thin Solid Films*. Dover, New York, 1965.
4. Gong, X.-Y. and Clarke, D. R., *Oxid. Met.*, 1998, **50**, 355.
5. Tolpygo, V. K. and Clarke, D. R., *Oxid. Met.*, 1998, **49**, 187.
6. Lipkin, D. M. and Clarke, D. R., *J. appl. Phys.*, 1995, **77**, 1855.
7. Thouless, M. D., Hutchinson, J. W. and Liniger, E. G., *Acta metall. mater.*, 1992, **40**, 2639.
8. Suo, Z. and Hutchinson, J. W., *Adv. appl. Mech.*, 1992, **29**, 63.
9. Evans, A. G., Crumley, G. B. and Demaray, R. E., *Oxid. Met.*, 1983, **20**, 193.
10. Evans, A. G., Ho, M. Y. and Hutchinson, J. W., *Mater. Sci. Engng*, 1998, **A245**, 168.
11. Tolpygo, V. K. and Clarke, D. R., in preparation.

INITIATION OF OXIDE SCALE DECOHESION AND SPALLING: MICROSCOPY OBSERVATIONS AND PIEZOSPECTROSCOPIC STRAIN MEASUREMENTS

Vladimir K. Tolpygo and David R. Clarke

Materials Department, College of Engineering
University of California, Santa Barbara, CA 93106-5050

Abstract

The processes leading up to decohesion and spalling of the α - Al_2O_3 scale formed on a Fe-Cr-Al alloy at 1000°C have been investigated by combining optical microscopy observations with local stress measurements made using photostimulated luminescence spectroscopy. Scale decohesion, on cooling, is apparent from changes in the optical reflectivity from the alloy surface. The regions of scale decohesion are found to be associated with the crests of the wrinkled morphology of the oxide layer. The localized decohesion is accompanied by partial stress relaxation in the oxide and is attributed to separation of the metal from the oxide. As the wavelength of the oxide wrinkles increases with oxidation time, the size of the regions, separated as a result of cooling, also increases. This increase in size and the subsequent linking together of the separated regions are proposed to be the mechanisms by which the localized decohesion evolves until reaching the critical size for spontaneous buckling and spalling. The accompanying changes in both optical reflectivity and luminescence intensity may provide the basis for a non-destructive method of monitoring damage evolution.

1. INTRODUCTION

Decohesion and spalling of protective oxide scales are the two processes that limit the operating time and temperature that an alloy can be used in an oxidizing atmosphere. Whilst it is known that spalling tends to occur on cooling, rather than at the oxidation temperature, very little is known about the microscopic processes that lead to spalling.

The primary reason of scale decohesion and spalling is the build up of residual compressive stress in the oxide during cooling caused by the difference in thermal expansion between the alloy and the oxide. (Any growth stresses in the scale simply augment the thermal mismatch stress.) Some insight into the possible processes leading up to spalling comes from the fracture mechanics of thin films under compression. If the oxide-metal interface is flat, no forces act perpendicular to the interface and so the scale decohesion can only occur by elastic buckling away from the alloy surface followed by cracking and spalling. However, when the oxide-metal interface is rough, the biaxial compressive stress in the scale is geometrically transformed, so that local tension across the interface is created at the peaks and corresponding local compression at the valleys (1).

Rigorous fracture mechanics analyses provide a means of quantifying these two cases. For instance, for compressively stressed films on a flat surface, buckling can only occur when a critically sized flaw first exists at the interface between the substrate (the alloy) and the film, and its radius, r_c , is given by the relation (2)

$$r_c \approx 1.1 \cdot h_{ox} (E_{ox} / \sigma_B)^{1/2} \quad [1]$$

where h_{ox} is the scale thickness, E_{ox} is the Young's modulus of the oxide, and σ_B is the biaxial compressive stress in the oxide. Taking typical values for the residual compressive stress after cooling, $\sigma_B \sim 3.0 - 3.5$ GPa, the size of the flaw is about 20-25 times the scale thickness. Pre-existing flaws of such a size are rarely seen yet the scale on many alloys spalls very easily. This then raises the question of how, and by which process, sufficiently large flaws can be generated during oxidation. Similarly, mechanics analyses of the effect of surface roughness indicates that the maximum tensile stress, σ_N , across the interface created geometrically by a convex domed surface of radius of curvature, R , is given by:

$$\sigma_N = 2\sigma_B \frac{h_{ox}}{R} \quad [2]$$

It should be noted, however, that the existence of a tensile stress across the interface is not a sufficient condition for failure but merely a necessary one. It is, therefore, essential for a fracture criterion to be established for the separation along a curved interface subject to these tensile stresses. This has yet to be done but nevertheless it is physically meaningful to discuss the magnitudes of the tensile stresses created by surface curvatures. It is also clear that, for given oxidation conditions (time and temperature), the magnitude of the tensile stresses across the interface depends on its roughness.

Whilst surface roughness can be intentionally introduced prior to oxidation by a number of means, such as grit-blasting, it can also evolve naturally from an originally flat alloy surface on some alloys by the phenomenon of wrinkling. In this process, as detailed and quantified elsewhere (3), the wavelength and amplitude of alumina scale undulations on the Fe-Cr-Al alloy increase with oxidation time. As a result, when the alloy is cooled to room temperature, the tensile stress created across the oxide-metal interface should also change with oxidation time.

It is well known that wrinkled alumina scales exhibit quite poor spalling resistance, in particular, in the course of cyclic oxidation. The most commonly accepted explanation of this behavior is the harmful effect of sulfur segregation to the oxide-metal interface (4). Nevertheless, some recent experimental observations show that, even if sulfur segregation is eliminated by yttrium doping, roughening of the alloy surface prior to oxidation may have an adverse effect on the oxide spalling resistance compared to a flat surface (5). Still, there is no clear evidence that oxide wrinkling causes interface decohesion, a pre-requisite for buckling to occur.

In this work, our objective was to address the connection between wrinkling and spalling by investigating the initial stages of oxide decohesion using both optical microscopy and local measurements of stress in the alumina scale. The latter were made using photostimulated luminescence piezospectroscopy (6). The Fe-Cr-Al alloy without a reactive element addition was selected for investigation since its thermally-grown alumina scale both wrinkles and spalls after a period of several hundred hours at 1000°C.

2. EXPERIMENTAL

A conventional Fe - 22.0%Cr - 5.28%Al (wt.%) vacuum-induction melted alloy was studied. The content of impurities was determined to be: 82 ppm C; 49 ppm S; 23 ppm P; 120 ppm Si. The alloy was first annealed at 1100°C and then cut into rectangular specimens. The specimens were mechanically polished to a 1- μ m surface finish and oxidized in air at 1000°C. The heating and cooling rate was about 500°C/min. In the oxidation conditions used, the alloy forms alpha-alumina scale from the very beginning of oxidation, so that no indications of transition (metastable) aluminas or other oxides were found. The α -Al₂O₃ scale was analyzed using optical and scanning electron microscopy (SEM), and the residual stress in the oxide was measured using photostimulated chromium luminescence piezospectroscopy.

The experimental configuration used in making the piezospectroscopy measurements enables both the residual stress within a very small volume of the scale, with the lateral size about 2-3 μ m, as well as the spatial average value (by defocusing the objective lens or by moving the specimen under the microscope during spectrum acquisition) to be determined. Therefore, both the local residual stresses and the average stress for the whole scale were measured. Two parameters of the luminescence spectra were analyzed in detail: the piezospectroscopic frequency shift of the ruby R₂ line from the compressed oxide relative to the oxide detached from the same specimen, and the intensity of the luminescence (counts per second) normalized for different measurements using a reference ruby crystal. The former gives a direct measure of the hydrostatic component of the stress tensor (6,7). The intensity of the characteristic spectrum, being proportional to the chromium content in the scale and the probe volume, also provides additional information as will be shown below.

3. RESULTS AND DISCUSSION

3.1. Oxide Scale Morphology

The α -Al₂O₃ scale formed during high-temperature oxidation of the Fe-Cr-Al alloy exhibits a typical convoluted or wrinkled morphology (Fig. 1). Oxide wrinkles develop in the course of oxidation as a result of plastic deformation of the scale. The presence of alumina grain imprints on the entire metal surface, except for the areas around alloy grain boundaries, indicates that the scale remains in contact with the metal during oxidation. Recent quantitative measurements of the wrinkling morphology show that it evolves with oxidation time, so that both the average wavelength and amplitude of undulations increase as the scale becomes thicker (3). In order to maintain contact at the metal-oxide interface, the scale wrinkling is accompanied by metal deformation in the vicinity of the interface, and the configuration of the metal surface is generally similar to the outer oxide surface (Fig. 1a).

Very rarely, interfacial cavities were observed. They were usually seen as smooth shallow craters on the metal surface after removing the oxide, indicating locations where the scale had separated during its growth. The occurrence of these interfacial cavities was invariably associated with various defects on the metal surface such as polishing scratches, non-metallic inclusions, contaminants, as well as the alloy grain boundaries (8). As

thorough polishing and cleaning the alloy surface before oxidation almost eliminates interfacial cavities, this form of scale decohesion and its influence on spalling resistance can be ignored. Thus, in the following, we consider the behavior of the oxide which is attached to the metal during oxidation.

3.2. Observations of Scale Separation

The wrinkled scale generally exhibits good spalling resistance after isothermal oxidation at 1000°C and cooling to room temperature. Apart from at the edges of the specimens, no visible spalling occurs even at very high cooling rates (up to 1000°/min). However, observations using a conventional optical microscope reveal that the oxide does not remain in contact with the metal everywhere over the specimen surface. Fig. 2 shows a series of optical micrographs of the Fe-Cr-Al alloy after isothermal oxidation for 30, 100, and 400 hr. The dark-gray area corresponds to the alumina scale attached to the metal, whereas the brighter regions indicate places where the scale is separated (but not spalled) from the metal surface.

Provided that the oxide thickness on a given specimen is uniform, as confirmed by direct SEM observations, the higher reflectivity of certain regions clearly indicates regions of scale decohesion. The optical contrast between adherent and separated oxide is due to the fact that the difference in index of refraction of the metal-gas interface is higher than that of the metal-oxide interface (Fig. 3). Since most of the reflection of incident light comes from the metal (the thin oxide layer is essentially transparent), the metal surface appears brighter under debonded oxide than when in contact with the oxide. Spallation of the scale, exposing a bare metal surface, produces even more distinct optical contrast and can easily be detected and distinguished from the oxide-metal separation which takes place without spalling.

A few other observations confirm that the separated regions of the scale form during cooling from the oxidation temperature. Firstly, their appearance can be observed through an optical microscope within minutes after removing a specimen from the furnace as the specimen is still cooling. The number of separated regions is smaller after slow cooling, whereas increasing the cooling rate results in scale separation in more places. Finally, removing the scale, for instance, by bending the oxidized specimen, reveals an imprinted alloy surface, which indicates oxide-metal contact during oxidation. (The presence of large interfacial cavities under the scale would give rise to similar optical contrast as the cooling-induced separation).

The localized separated regions of about 5-10 μm in size appear after oxidation for 20-25 hours when the scale thickness is about 0.5 μm . After longer oxidation times, their size and number increase (Fig. 2). Since the average wrinkling wavelength, measured previously on a similar Fe-Cr-Al alloy (3), correlates well with the size of separated regions, it is reasonable to assume that each region corresponds to the crest or ridge of the wrinkles. Indeed, after prolonged oxidation when individual wrinkles can be resolved by optical microscopy, it becomes clear that almost every crest of the scale is separated after cooling (Fig. 2c). A substantial enhancement of the scale separation with oxidation time suggests that the process is largely determined by geometrical parameters of the scale, namely, the oxide thickness, wavelength and amplitude of scale undulations (Fig. 4). It is notable that no localized separation of this type is observed for very thin alumina scales

after short oxidation times ($h_{ox} < 0.5 \mu\text{m}$), although wrinkling occurs from the very beginning of oxidation (3). A notably smaller number of the separated regions after slower cooling indicates that plastic deformation in the metal (and, perhaps, in the oxide) can provide an alternative mode of stress relaxation.

Both theoretical considerations (1,9) as well as finite element calculations (5,9-11) show that the wavy configuration of the oxide-metal interface creates out-of-plane stress component as a result of thermal expansion mismatch during cooling. The stress across the interface is tensile at the concave regions and compressive at the convex regions. The existence of tensile stresses acting normal to the oxide-metal interface is usually considered to be essential pre-requisite for oxide separation and spalling. However our experimental results show that, at least over the range of oxidation times studied, the separation in the ridge areas during cooling does not lead to spalling, so that these areas remain isolated. The reason is, probably, that each convex region of the scale is surrounded by regions where the stress across the interface is compressive. Thus, the normal tensile stresses initiate the scale separation in the ridge areas and the normal compressive stresses in the valley areas prevent lateral propagation of interfacial cracks.

The size of the separated regions is expected to be related to the size of the regions over which tensile stresses are created, i.e. about a half of the wrinkling wavelength. For this reason, the regions of cooling-induced separation become larger after longer oxidation times (Fig. 2) as the wavelength increases. Additionally, because of the irregular shape of oxide ridges, some of the adjacent separated regions may link together, as shown in Fig. 2c, creating much larger areas of decohesion. After oxidation at higher temperatures or for much longer times, these areas may well become sufficiently large to cause extensive spalling of the scale, which indeed was usually observed after oxidation at 1200°C .

The second type of oxide decohesion, quite different from the described above, was observed after relatively short oxidation times (less than 25 hr at 1000°C) when the oxide thickness was about $0.2\text{-}0.5 \mu\text{m}$. In this case, separation occurs in the form of large blisters shown in Fig. 5. These are dome-shaped regions of the scale, $20\text{-}40 \mu\text{m}$ in diameter, elevated up to a few micrometers above the metal surface and fringed by cracks over the perimeter. The blisters can easily be detected by both optical (Fig. 5a) and scanning electron microscopy (Fig. 5b). Another distinguishing feature is that the area of a single blister covers a number of oxide wrinkles. Since the metal surface under the blisters replicates the wrinkles and grain structure of the scale (Fig. 5d), oxide separation also takes place on cooling. This second type of decohesion can be described as "normal" buckling mechanism of thin compressed films.

The origin of this type of scale separation remains unclear. It is not common for all specimens studied (it may happen on some specimens but not on the others), so it is probably caused by localized patches of unidentified impurities or contaminants on the alloy surface, which form a critical flaw size for the onset of buckling.

3.3. Residual Stress in the Scale

The frequency shift of the Cr^{3+} luminescence measured on the scales after different oxidation times is presented in Fig. 6. The residual stress in the scale, σ , was calculated from the frequency shift, $\Delta\nu$, assuming that the oxide is under biaxial compression (7):

$$\overline{\Delta\nu} = \frac{2}{3} \Pi_{ii} \langle \sigma \rangle \quad [3]$$

where $\Pi_{ii} = 7.61 \text{ cm}^{-1}\text{GPa}^{-1}$. Since the scale on the Fe-Cr-Al alloy is wrinkled, this expression for the biaxial stress can only be used as an estimate. The reason is that the stress component normal to the interface is not zero for a wrinkled scale and, in each given place, its value depends on the local configuration of the oxide. By measuring the spatial average of the frequency shift, the contribution of the normal stress component can be minimized, since the algebraic sum of all stresses acting normal to the specimen surface should be zero. More detailed approach relating the residual stress in oxide scale to the piezospectroscopic frequency shift has recently been presented (10).

Apart from significant variations at short oxidation times (3), the value of the spatial average of the residual stress appears to be almost constant after isothermal oxidation at 1000°C (Fig. 6). These average values were measured using a large probe size (about $15 \mu\text{m}$) at 20-25 different locations over the surface of each specimen after isothermal oxidation. For comparison, the residual stress in the flat scale formed on the Fe-Cr-Al-Y alloy from ref.(12) is included. The fact that the average residual stress in the wrinkled scale neither increases nor decreases with oxidation time suggests that the progressive increase in area of separation of thicker scales on cooling is not related to a higher average value of the residual stress.

The solid data points in Fig. 6 correspond to the frequency shifts measured separately in the vicinity of the oxide ridges and valleys using the $2\text{-}3 \mu\text{m}$ probe size. Clearly, the shift (and the corresponding residual stress) is much higher than the average in the valley regions and lower around the ridges. The wavy morphology of the scale and oxide-metal interface dictates that the stress component normal to the interface varies from a maximum tensile value to zero in the ridge region and from a maximum compressive value to zero in the valley region (1,10). For the small volumes of the oxide analyzed by the optical probe, these normal stresses contribute with opposite sign to the piezospectroscopic shift.

Two luminescence spectra in Fig. 7 illustrate the difference between ridges and valleys: the average shift of the R_2 ruby line from the valleys is about $6\text{-}7 \text{ cm}^{-1}$ higher. To a first approximation, assuming that the in-plane stress component does not vary much over the scale surface, this gives about $1.2\text{-}1.4 \text{ GPa}$ difference between the normal tensile stress at the ridges and the normal compressive stress at the valleys. This value is in a good agreement with the results of finite element calculations (10) showing the maximum normal stress at the interface in the range $(0.1\text{-}0.3)\sigma_b$, where σ_b is the biaxial compression of the flat oxide layer. A typical value for σ_b caused by thermal expansion is about $3.0\text{-}3.2 \text{ GPa}$. Thus, the maximum normal stress is expected to be in the range $0.3\text{-}1.0 \text{ GPa}$, and the difference between maximum tensile and maximum compressive stresses should be two times larger, $0.6\text{-}2.0 \text{ GPa}$ depending on the geometry of the oxide wrinkles. No systematic variation of this value with oxidation time is observed experimentally, although the geometrical parameters of the scale continue to change. From the equation [2] it follows that, for the time-independent in-plane stress σ_b , the constant value of σ_N is expected when both the oxide thickness, h_{ox} , and the radius of interface curvature, R , similarly increase with oxidation time. If, however, the oxide growth rate is higher, then the stress across the interface after cooling will increase as the scale becomes thicker.

An additional set of measurements was performed in order to detect whether there was a difference between the oxide ridges which had separated from the metal after cooling and those remaining in contact. After oxidation for 100-200 hours, both in-contact and separated ridges can be distinguished in the microscope and their luminescence spectra can be consecutively measured on the same specimen using a small probe size. The results are shown in Fig. 8, where the frequency shifts and luminescence intensities are compared. A large scatter of the data is most probably related to different geometry of each individual ridge. Nevertheless, it can be concluded that the separated ridges have, on the average, somewhat smaller frequency shift than the ridges still in contact with the metal. This small, yet significant, difference (about 1.8 cm^{-1} corresponding to a stress of about 350 MPa) indicates that partial stress relaxation in the oxide occurred as a result of separation. Contrary to what might be expected, however, separation apparently does not lead to a complete stress relaxation in the oxide, as these regions remain under residual compression of about 2 GPa (Fig. 8a). This result further supports the suggestion that local scale separation at the crests of wrinkles is not a form of buckling since the latter should result in a nearly complete stress relaxation.

As only partial stress relaxation occurs in the scale as a result of separation, the most probable reason for the separation is the deformation of the underlying metal. In contrast to the stress distribution at the planar interface, where a biaxial tension in the metal can usually be ignored (the stress in the metal is very small if the oxide is much thinner than the metal), the stresses in the metal beneath the wrinkled interface are inhomogeneous and large enough in certain places to cause metal deformation (9-11). At the crests of the wrinkles, the tensile stress across the interface is created on cooling and metal deformation leads to debonding at the interface. So, unlike buckling, where the oxide layer bends away from the metal surface, local debonding of the wrinkled scale is believed to be primarily due to the deformation of the underlying metal in the convex regions of the interface.

Another important feature of the measurements presented in Fig. 8 is the striking difference in luminescence intensity between the separated and in-contact oxide ridges. The average signal intensity from the separated oxide is almost twice larger than that from the same oxide in contact with the metal (Fig. 8b). For a typical chromium concentration range in the alumina scales (around 0.5 - 1 wt.%), the luminescence intensity should generally be proportional to the number of chromium ions within the probe volume, i.e. to the scale thickness. We do not have any indications that chromium concentration might vary significantly from place to place, nor that the scale might be much thicker in some places than in the others. Since all measurements were performed at the same time and under identical experimental conditions (laser power, objective lens etc.), an increased luminescence intensity from the-separated oxide is likely to be of the same origin as the optical contrast described previously (Fig. 3). Although a detailed study of this phenomenon is still in progress, an essential point is that the variation of luminescence intensity from place to place on the scale of uniform thickness may be used to detect the areas of oxide decohesion.

From the results in Fig. 8b it is also clear that the luminescence intensity from the in-contact ridges is more uniform than from the separated ridges. A substantial scatter of intensity data in the latter case may reflect another aspect of the luminescence technique: intensity dependence on the thickness of the separation between the alumina scale and the metal surface. Again, further work is required to quantify this observation.

To this point, all piezospectroscopic results were presented for the scales apparently free of cracks. A closer examination by SEM of relatively thick scales formed by oxidation for 200-400 hr reveals small cracks located near the most pronounced ridges (Fig. 9). In most cases, they cannot be seen in the optical microscope and, therefore, apart from SEM observations, the fractured regions of the scale can only be identified from the shape and position of the luminescence peaks. Obviously, cracking of the scale during cooling results in stress relaxation, thus the frequency shift from such places is noticeably smaller than from the adjacent intact regions. A typical range of the frequency shifts for the fractured regions of the scale is shown in Fig. 6.

Within the oxidation times studied, oxide cracking is only occasional and mainly occurs along alloy grain boundaries. The luminescence spectra presented in Fig. 10 give an example of how the scale fracture can be identified (as mentioned previously, no visible spalling or detectable mass loss were observed on these specimens after isothermal oxidation at 1000°C). The spectrum at the top of Fig. 10 corresponds to an extensively fractured portion of the scale with nearly zero frequency shift relative to the unstressed scale. The second spectrum was recorded from the region at the edge of a long crack extended along the alloy grain boundary. The frequency shift ($\Delta\nu \approx 8 \text{ cm}^{-1}$) is approximately half the average shift for the intact scale. This suggests that the crack leads to almost complete stress relaxation in one direction (perpendicular to the crack line) but does not change the stress in the direction parallel to the crack line. Finally, the spectrum at the bottom of Fig. 10 was recorded from a severely cracked, but not spalled, region of the scale. Such an asymmetric spectrum can be fitted by two symmetrical doublets, each corresponding to different portions of the scale: one under higher and another under lower compression, as shown by dotted lines. The presence of lower-stressed oxide indicates partial stress relaxation as a result of cracking. Similar asymmetric peaks were obtained in the vicinity of the most pronounced ridges after prolonged oxidation, where small cracks can be observed by SEM (Fig. 9).

The frequency shift from the buckled scale in the area of blisters (Fig. 5) almost always is close to zero. Apparently, buckling of the oxide during cooling, accompanied by through-thickness cracking at the perimeter of the blisters, produces a complete stress relaxation in the oxide. It is worth mentioning that, as in the case of local separated regions, the luminescence intensity from the buckled scale is twice as large as the intensity from the adjacent intact scale.

4. CONCLUDING REMARKS

Two distinct forms of detachment of the alumina scale from the underlying Fe-Cr-Al alloy occur after isothermal oxidation at 1000°C and cooling to room temperature. One is a conventional form of buckling which is observed in case of relatively thin scales (0.2-0.5 μm) and may be attributed to the presence of localized patches of impurities at the interface that significantly decrease the local interfacial fracture resistance.

The other, more general, form of decohesion is associated with the ridges in the wrinkling morphology and resulting tensile stresses across the oxide-metal interface. The size and the number of separated regions increase with oxidation time as the wavelength of oxide wrinkles increases. Only partial stress relaxation in the oxide occurs as a result of this form of oxide-metal separation, so it is believed that separation is caused by the underlying

metal contracting away from the oxide on cooling. Localized separation of the scale after isothermal oxidation at 1000°C does not lead to spalling as the separated regions remain surrounded by intact regions. However the results presented give some insight into how the oxide failure would occur in cyclic oxidation conditions or after oxidation at higher temperatures. Thicker scales formed at higher temperatures are more prone to spalling for several reasons. First, the thermal mismatch stress after cooling is higher as well as the elastic strain energy, which is proportional to the scale thickness, is greater. Additionally, due to an increase of the wrinkling wavelength and amplitude, the separated regions become large enough to link together creating extended areas of decohesion and, eventually, through-thickness cracking and spallation of the scale. During cyclic oxidation, accumulation of local damage in the scale (cracks and separated regions) also leads to spontaneous spalling after a number of cycles.

Finally, on the basis of the combined microscopy and piezospectroscopy measurements described here, it is believed that the initiation of oxide failure may be detectable non-destructively. The increased luminescence intensity from the certain regions of oxide scale, as well as the distinct optical contrast, identifies local areas of scale decohesion even when no visible spalling occurs. Furthermore, the large difference in the frequency shift and shape of the luminescence peaks between cracked and intact regions of the scale may make it possible to locate where the scale begins to fail.

ACKNOWLEDGMENTS

This research was financially supported by the Office of Naval Research through grant NO0014-97-1-0190.

REFERENCES

1. A. G. Evans, G. B. Crumley, and R. E. Demaray, *Oxid. Met.* 20, 193 (1983).
2. A. G. Evans and J. W. Hutchinson, *Int. J. Solids and Structures* 20, 455 (1984).
3. V. K. Tolpygo and D. R. Clarke, *Acta Materialia* (1998), in press.
4. G. H. Meier, F. S. Pettit, and J. L. Smialek, *Werkstoffe und Korros.* 46, 232 (1995).
5. J. Chao, J. L. Gonzalez-Carrasco, *Mater. Sci. Eng. A230*, 39 (1997).
6. Q. Ma and D. R. Clarke, *Acta Metall. Mater.* 41, 1811 (1993).
7. J. He and D. R. Clarke, *J. Amer. Ceram. Soc.* 78, 1347 (1995).
8. V. K. Tolpygo, submitted to *Oxid. Met.* (1997).
9. A. G. Evans, M. Y. He and J. W. Hutchinson, *Acta Mater.* 45, 3543 (1997).
10. X.-Y. Gong and D. R. Clarke, *Oxid. Met.* (1998) in press.
11. R. L. Williamson, J. K. Wright, and R. M. Cannon, in Proc. Symp. on Fundamental Aspects of High Temperature Corrosion, D. A. Shores, R. A. Rapp and P. Y. Hou, eds. Vol. 96-26, pp.16-27, The Electrochem. Soc., Pennington, NJ (1997).
12. V. K. Tolpygo and D. R. Clarke, *Oxid. Met.* 49, 187 (1998).

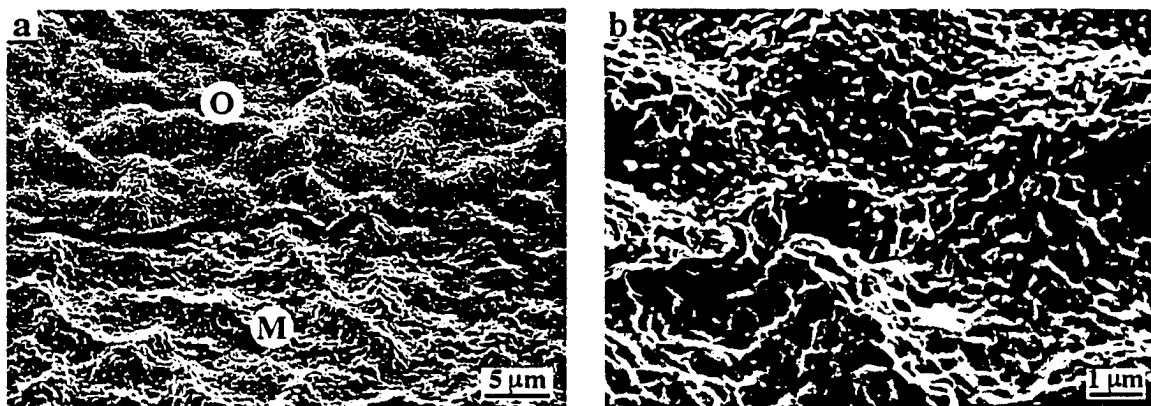


FIG. 1. Typical morphology of the wrinkled α - Al_2O_3 scale on the Fe-Cr-Al alloy after oxidation at 1000°C for 70 hours: (a) - general view (O - oxide, M - metal); (b) - enlarged view of the scale cross-section and imprints of alumina grains on the metal surface.

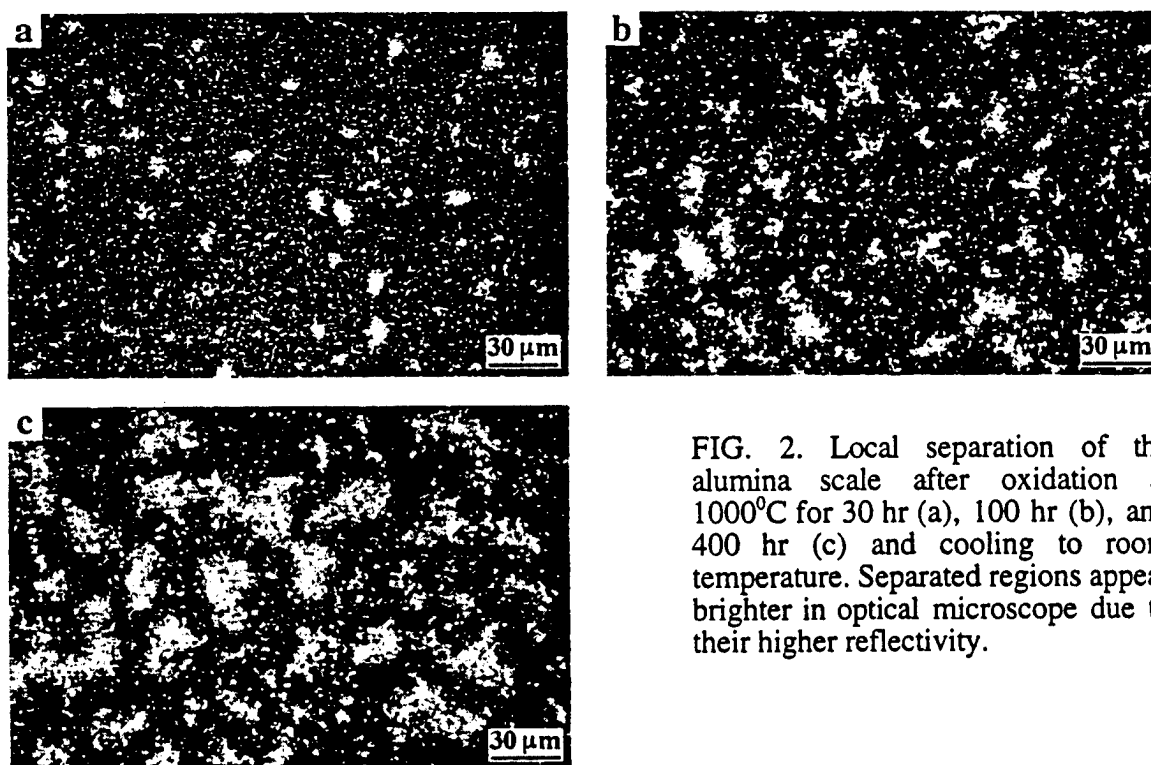


FIG. 2. Local separation of the alumina scale after oxidation at 1000°C for 30 hr (a), 100 hr (b), and 400 hr (c) and cooling to room temperature. Separated regions appear brighter in optical microscope due to their higher reflectivity.

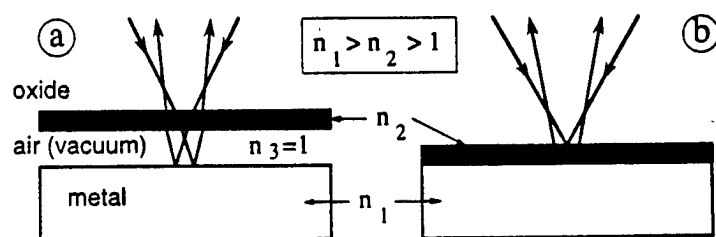


FIG. 3. Schematic illustration of the origin of the optical contrast between separated (a) and in-contact (b) scale. Reflectivity of the metal surface is proportional to the difference in the index of refraction: $(n_1 - 1)$ in the former, $(n_1 - n_2)$ in the latter.

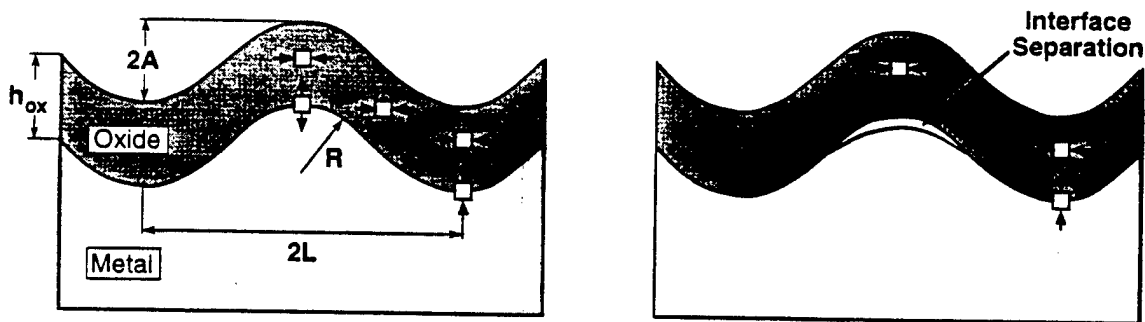


FIG. 4. Schematic diagram illustrating the state of residual stress in a wrinkled scale and interface separation (debonding) at the wrinkling ridge as a result of tensile stresses across the interface. The oxide remains in contact at surrounding valleys where the stress normal to the interface is compressive.

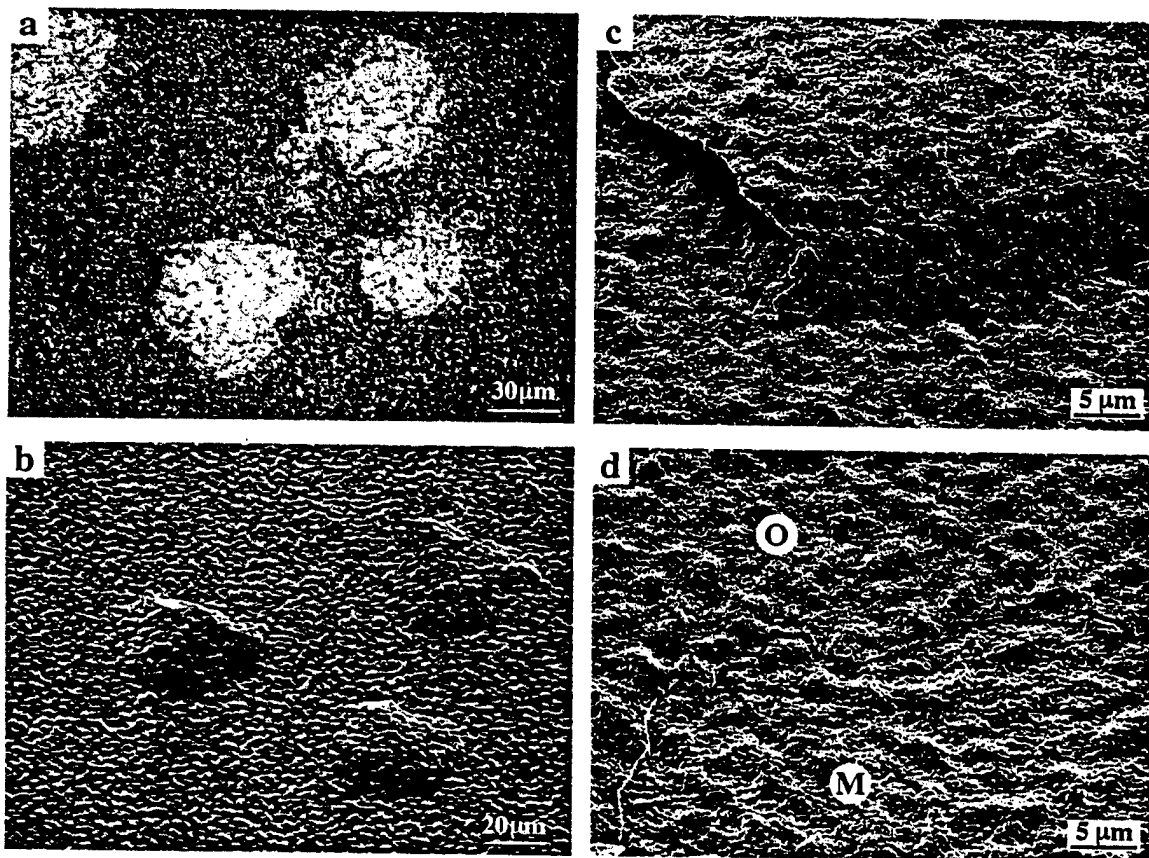


FIG. 5. Local buckling of the alumina scale on the Fe-Cr-Al alloy after oxidation for 10 hr at 1000°C: (a) optical micrograph showing the separated regions of the scale apparent from their higher reflectivity; (b) SEM micrograph showing the pronounced oxide up-lift associated with buckling ("blistering"); (c) cracking of the scale over the perimeter of the buckled regions; (d) metal surface exposed after spalling of the blister (O - oxide, M - metal).

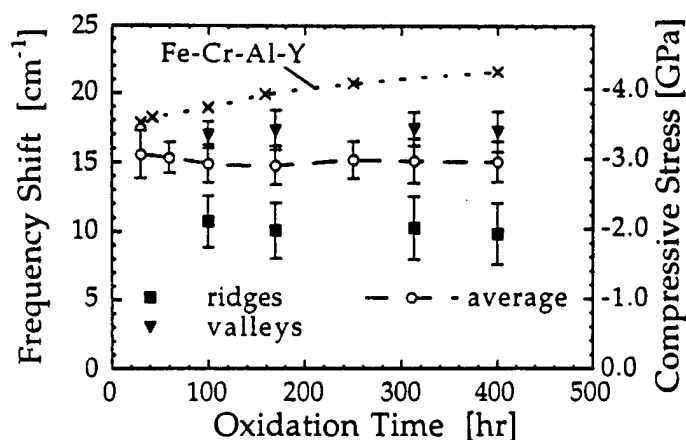


FIG. 6. Piezospectroscopic stress measurements in the alumina scales after isothermal oxidation at 1000°C: spatially averaged values (open circles) and separate data for ridges and valleys (solid symbols). The residual stress in the scale on the Fe-Cr-Al-Y alloy from ref. (12) is shown for comparison.

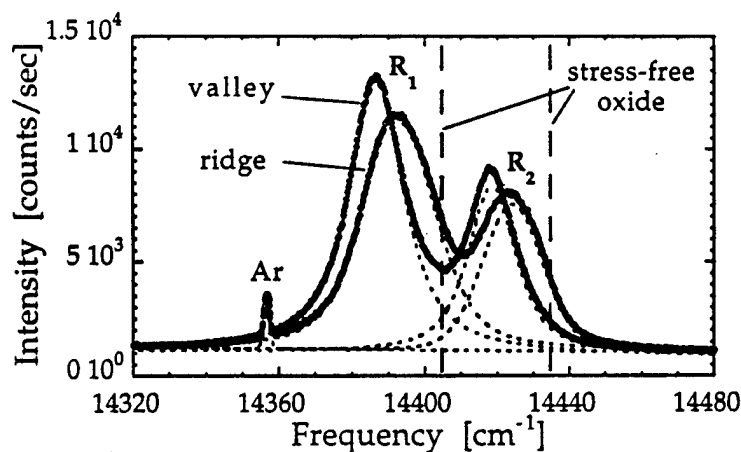


FIG. 7. Example of luminescence spectra recorded from the ridges and valleys after oxidation for 100 hr. The position of the R₁-R₂ ruby doublet for the stress-free scale is indicated. The frequency shift is notably higher for the valley region.

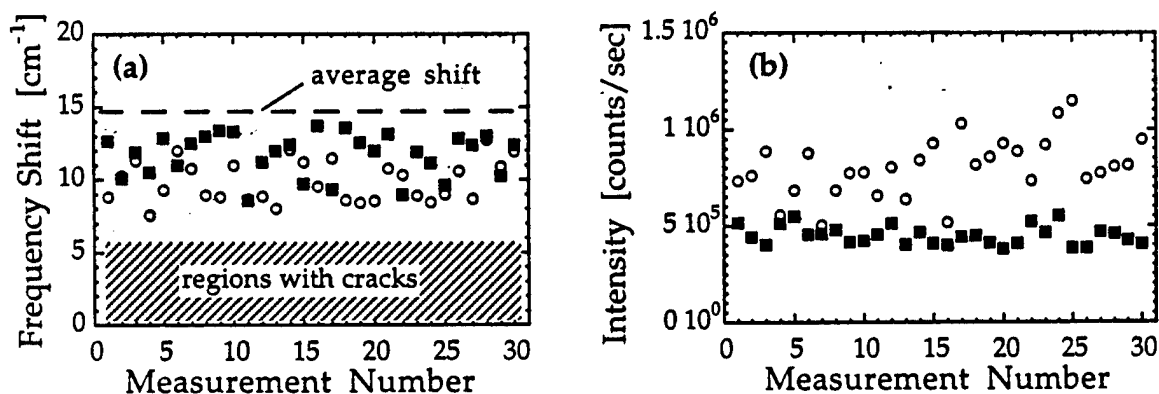


FIG. 8. Results of a series of measurements of the wrinkled scale after 100-hr oxidation: (a) - frequency shift from different oxide ridges; (b) - luminescence intensity from the same places. Open circles - separated ridges; solid squares - in-contact ridges. These two can be distinguished due to the difference in optical reflectivity.

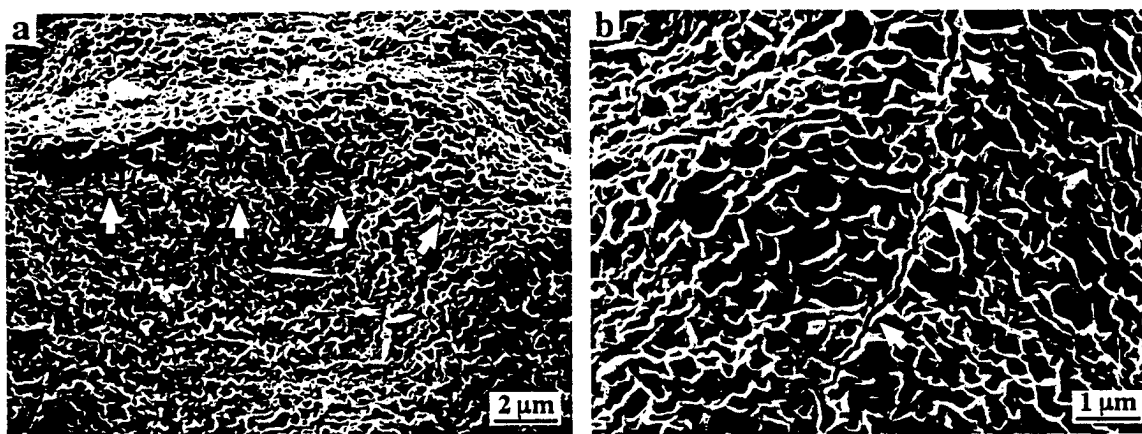


FIG. 9. SEM micrographs showing the presence of micro-cracks (indicated by arrows) in thick scales after oxidation for 400 hr at 1000°C . The cracks appear after cooling to room temperature at crests of the most pronounced wrinkles.

FIG. 10. An example of luminescence spectra recorded from the cracked scale after isothermal oxidation for 400 hr at 1000°C (no visible spalling occurred).

